Development of Acrylamide/Acrylic acid Superabsorbent Polymer (SAP) Particles for Water Applications

Ehsan Tabesh

A DISSERTATION SUBMITTED TO

THE FACULTY OF GRADUATE STUDIES

IN PARTIAL FULFILLMENT OF THE REQUIREMENTS

FOR THE DEGREE OF DOCTOR OF PHILOSOPHY

GRADUATE PROGRAM IN MECHANICAL ENGINEERING

YORK UNIVERSITY

TORONTO, ONTARIO

February 2025

Abstract

Water contamination, particularly from bacterial sources, poses significant risks to public health and environmental safety. Low bacterial concentrations in water samples often go undetected by conventional methods, increasing these risks and highlighting the need for efficient sample enrichment techniques. This research investigates the use of superabsorbent polymer microparticles (SAP-MPs) and their nanocomposites with MXene nanosheets for enriching bacterial samples. The study first focuses on developing innovative microfluidic platforms for real-time characterization of SAP-MPs. Subsequently, advanced MXene/SAP-MP nanocomposites are introduced for enhanced bacterial enrichment and water analysis.

The study is structured into four objectives. The first objective involves the design and fabrication of a novel microfluidic device for high-resolution, real-time characterization of SAP-MPs. This device enables detailed single particle analysis of swelling behaviors, including volume swelling ratio (VSR) and swelling rate (SR). The second objective investigates the effect of particle size, crosslinker concentration, acrylic acid concentration, and neutralization degree on the swelling behavior of SAP-MP. Results revealed a ~40% and ~300% reduction in equilibrium VSR (VSR_{eq}) and SR with increased crosslinker concentration, respectively, while increasing acrylic acid concentrations enhanced VSR_{eq} and SR by ~200%. A ~300% increase in VSR_{eq} was observed with smaller particle sizes, marking the first single-particle-scale study of this phenomenon. The third objective demonstrates the synthesis of MXene/SAP-MP nanocomposites using the Breathing-In-Breathing-Out (BI-BO) method, achieving successful integration of MXene nanosheets without compromising swelling behavior. Finally, the fourth objective evaluates bacterial enrichment performance, revealing a 10-fold enrichment efficiency and 90% recovery efficiency under

optimized conditions.

This research advances the fundamental characterization of SAPs and their applications, including water treatment, biosensing, and environmental monitoring.

Acknowledgements

First, I would like to express my earnest gratitude to my supervisors, Prof. Pouya Rezai, and Prof. Siu Ning (Sunny) Leung, for giving me the opportunity to study at York University and for their guidance and patience throughout my PhD studies.

I would like to thank Prof. Paul O'Brien and Prof. Dasantila Golemi-Kotra for their support and advice during my comprehensive exam and committee meetings. I am also grateful to Prof. Ebrahim Ghafar-Zadeh and Prof. Vahid Adibnia for their consideration and patience during the thesis examination.

I express my sincere thanks to my colleagues at York University for their support and guidance during my PhD studies. I am also grateful to my dear friends for their friendship and encouragement, and for always being there for me through thick and thin.

Finally, I would like to acknowledge my family, my parents, and my sister for their unconditional help in every step of my life. A very special thank you to my wife, Sara, for her endless love, support, and patience throughout this journey. Her encouragement has been a constant source of strength, and I am deeply grateful for her presence in my life.

Table of Contents

List of Tables

List of Figures

List of Symbols and Abbreviations

Symbol / Abbreviation	Description
AA	Acrylic Acid
Aam	Acrylamide
APS	Ammonium Persulfate
BI-BO	Breathing-In-Breathing-Out Process
CD	Concentration Degree
CFU	Colony-Forming Units
CNTs	Carbon Nanotubes
DI Water	Deionized Water
E. coli	Escherichia coli
EF	Enrichment Factor
FTIR	Fourier Transform Infrared Spectroscopy
HCl	Hydrochloric Acid
IPA	Isopropyl Alcohol
LiF	Lithium Fluoride
MBAm	N,N′-Methylene Bisacrylamide
MAX Phase	Precursor Material for MXene
MXene	Two-Dimensional Transition Metal Carbide/Nitride
NaOH	Sodium Hydroxide
RE	Recovery Efficiency
SAP	Superabsorbent Polymer
SEM	Scanning Electron Microscopy
SR	Swelling Rate
T_d	Time Difference
Ti_3AlC_2	Titanium Aluminum Carbide (MAX Phase)
TGA	Thermogravimetric Analysis
T_t	Transition Time
UV-Vis	Ultraviolet-Visible Spectroscopy
VSR_{eq}	Equilibrium Volumetric Swelling Ratio
VSR	Volumetric Swelling Ratio
XRD	X-ray Diffraction
μm	Micrometer

Chapter 1

Motivation and Introduction

1.1 Background

Superabsorbent polymers (SAPs) are a class of loosely crosslinked hydrogels characterized by their exceptional ability to absorb and retain a large amount of water relative to their own mass [1]. This absorption capacity results from a process known as swelling, during which water diffuses into the polymer network, causing it to expand. SAPs' unique swelling behavior in aqueous environments makes them valuable across a variety of fields [2].

In construction, for instance, SAPs are integrated into concrete mixtures to act as internal curing agents, ensuring consistent hydration and reducing the risk of cracking [3]. These SAPs are often

tailored to exhibit lower water retention to match cement's moisture content. In agriculture, they enhance soil water retention, aiding plant growth in arid regions by releasing stored water over time [4, 5]. Agricultural SAPs are typically modified for slower water release and higher biocompatibility to integrate with soil ecosystems. In biomedical applications, SAPs are utilized in drug delivery systems and tissue engineering scaffolds, leveraging their biocompatibility and high water content to support healing and regeneration [4]. Biomedical SAPs frequently incorporate advanced monomers or crosslinkers to achieve enhanced biodegradability and biocompatibility in physiological conditions.

In enrichment applications, modified SAPs can selectively concentrate targets such as bacteria, protein, and biomolecules from dilute solutions. This capability is critical for analyzing biological samples, where concentrating the target molecule is often essential for accurate detection, diagnostics, or therapeutic development [6-10].

The properties and applications of SAPs are largely influenced by material and processing parameters such as monomer type, crosslinker type, initiator type, and polymerization method. These parameters govern the intrinsic structure and functionality of the polymer network. Additionally, particle size plays a crucial role in SAP performance, as the surface-to-volume ratio significantly affects the swelling process. Optimizing particle size is therefore essential for enhancing the swelling behavior and overall effectiveness of SAPs in various applications [2, 11].

At the microscale, SAPs may behave differently, necessitating comprehensive characterization. Existing literature that investigates the swelling behavior of SAP-MPs using conventional characterization methods, such as gravimetric methods (e.g., the tea-bag method), often presents inconsistencies, highlighting the need for an accurate and reproducible method to analyze these

particles under various conditions [12, 13]. Microfluidics has a great potential to offer a robust solution for the individual characterization of SAPs, providing insights into the behavior of individual SAP microparticles (SAP-MPs) [14].

In parallel, the use of SAPs and SAP-MPs in sample preparation for detection is increasing due to the outstanding properties of these materials. Water solutions frequently contain diverse pollutants, including biological contaminants, which pose significant challenges for assessing water quality. In the case of bacteria, waterborne diseases cause over 2.2 million deaths annually and substantial economic losses, estimated at nearly $12 billion per year [15]. A critical component of detection involves sample preparation including efficient separation, enrichment, and isolation of specific targets from these complex matrices. Absorption-based techniques offer promising potential for concentrating bacteria, thereby facilitating subsequent detection processes. SAPs could significantly enhance this step by improving the efficiency of detection methods, enabling more effective monitoring and analysis of bacterial pathogens in water samples [7].

The development of composite materials incorporating nanostructures, such as MXene nanoparticles, has shown promise in enhancing the functional properties of SAPs. MXene, a family of two-dimensional transition metal carbides, nitrides, or carbonitrides, exhibits exceptional mechanical, electrical, and chemical properties, making it an ideal candidate for creating advanced nanocomposites. Incorporating MXene into SAP-MPs can improve their performance in applications such as water treatment and biological contamination enrichment by enhancing sensitivity and efficiency. This improvement is attributed to MXene's unique properties, including its negative surface charge and diverse surface functional groups, which facilitate better interactions with biological molecules, and increased electrostatic interactions in aqueous

environments [16, 17]. These advancements align with the critical need for effective bacterial detection and enrichment systems, as discussed in the next section.

Despite their promising attributes, the integration of MXene nanoparticles into SAPs poses certain challenges. The high cost of synthesizing MXene materials [18], combined with their potential chemical instability under oxidizing or acidic conditions [19], could limit large-scale application. Additionally, achieving uniform dispersion of MXene within the SAP matrix requires precise optimization of synthesis parameters to prevent agglomeration, which could negatively impact performance [20]. Addressing these challenges is crucial to fully harness the potential of MXene-enhanced SAPs.

1.2 Research Problem Statement

Water scarcity, pollution, and bacterial contamination pose significant challenges for assessing water quality, where timely and accurate detection of bacterial contaminants is essential for mitigating associated health risks [21-24]. Advances in SAP technology have introduced promising approaches to bacterial enrichment, which is an important step prior to efficient bacterial detection. However, critical gaps remain in characterizing and optimizing these materials for real-world applications. Bacterial detection methods include culture-based techniques, molecular techniques (e.g., PCR), immunological methods (e.g., ELISA), and biosensors [9]. While generally reliable, these methods often have high detection limits and require sophisticated equipment and trained personnel. Effective detection often requires an initial enrichment step to concentrate bacteria from large water volumes to improve sensitivity and accuracy. These methods can be broadly categorized into conventional and portable techniques.

Despite advancements in SAP-related technologies, several challenges remain in the

characterization of SAP-MPs. During swelling, SAP-MPs expand significantly, transitioning from micro to macro-scale dimensions. This substantial volume change complicates single-particle and time-lapse swelling characterization, as conventional methods such as gravimetric analysis and optical imaging often fail to accurately capture the dynamic, multi-stage process. These methods may lack the temporal resolution to detect the transient swelling process or the spatial precision to account for localized environmental effects. Additionally, understanding how parameters such as particle size, crosslinker concentration, monomer concentration, and neutralization degree affect the swelling behavior of SAPs at the microscale remain insufficiently explored.

Furthermore, the application of SAP-MP and their nanocomposites in environmental analysis, particularly for bacterial enrichment in water samples, remains underexplored. Existing studies have primarily focused on macro-SAP applications rather than microparticles. This gap in research highlights the need for innovative SAP-MP-based approaches tailored for environmental applications. By bridging the knowledge gap in characterization and exploring the functionalization of SAP-MPs with advanced materials such as MXene, the field can address these challenges more effectively. There is a significant opportunity to enhance the sensitivity of bacterial detection methods by concentrating bacteria in water samples using MXene/SAP-MPs. Such nanocomposites can be used in a cost-effective pre-concentration step for traditional detection methods, which often suffer from high costs, low limits of detection (LOD), and reliance on complex instrumentation.

This research aims to address these gaps by advancing SAP-MP characterization techniques and exploring MXene-functionalized SAP-MPs for efficient bacterial enrichment in water samples.

1.3 Research Objectives

This thesis aims to address the above research gaps by pursuing the following objectives:

1. Design and fabricate a microfluidic platform for the real-time trapping and analysis of SAP-MPs' swelling behavior. The platform will enable single-particle characterization of SAP-MPs, allowing for quantitative analysis of their volume swelling ratio (VSR), swelling rate (SR), and swelling model.
2. Investigate the effects of particle size, crosslinker concentration (Cr), monomer concentration (AA), and neutralization degree (ND) on the swelling behavior of SAP-MPs. This objective will utilize the developed microfluidic platform to analyze the impact of these parameters individually and in combination, focusing on the structure-to-property relationships of SAP-MPs.
3. Synthesize MXene nanoparticles and develop MXene/SAP-MP nanocomposites. This objective will explore the incorporation of MXene into SAP-MPs using the BI-BO (Breathing-in Breathing-out) method, aiming to enhance their properties for environmental applications. The integration of MXene is expected to improve the nanocomposites' enrichment efficiency, leading to at least a two-fold increase in bacterial concentration efficiency compared to standard SAPs.
4. Evaluate the application of MXene/SAP-MPs for bacterial enrichment in water samples. This objective will assess the effectiveness of the nanocomposites in concentrating bacteria, without culturing or using external equipment.

1.4 Research Questions

To guide this research, the following key questions are posed:

1. How to effectively trap and analyze the swelling behavior of SAP-MPs, ranging from approximately 50 μm to 2 mm, in real time by designing and fabricating a microfluidic platform?
2. What are the individual and combined effects of particle size, crosslinker concentration, monomer concentration, and neutralization degree on the swelling behavior of SAP-MPs?
3. How can MXene nanoparticles be synthesized and effectively incorporated into SAP-MPs to create functional nanocomposites?
4. How do MXene/SAP-MPs nanocomposites perform in bacterial enrichment applications?
5. What factors, such as ionic strength, bacterial species, or particle loading, influence the efficiency of MXene/SAP-MPs in water analysis?

1.5 Scope and Limitations

1.5.1 Scope

This research focuses on the design and fabrication of a microfluidic platform to characterize the swelling behavior of SAPs under various conditions. It also includes the synthesis and characterization of MXene/SAP-MP nanocomposites and explores their application in bacterial enrichment for water analysis. The study encompasses both experimental and theoretical aspects, covering the design and validation of microfluidic devices, as well as practical applications of SAPs in bacteria enrichment.

1.5.2 Limitations

The research is limited to specific types of SAPs, particularly acrylic acid (AA) – acrylamide (Aam)-based SAP-MPs, and MXene nanoparticles. The findings may not directly apply to other types of SAPs or nanocomposites, as variations in polymer composition or nanomaterial properties

can significantly influence performance. The experimental conditions are controlled within laboratory settings, which may not fully replicate all real-world scenarios. For example, water samples with varying salinity, pH, or organic contaminants may yield different bacterial enrichment results, requiring further validation under field conditions. Additionally, the bacterial enrichment tests conducted are preliminary, necessitating further optimization to ensure their efficacy across diverse environmental conditions. Future studies could expand on this research by testing a wider range of SAP formulations and analyzing performance in different environmental matrices, such as seawater or wastewater.

1.6 Thesis Structure

This thesis is organized as follows:

Chapter 1: **Introduction**

Provides the background, research problems, objectives, research questions, scope, and limitations of the study.

Chapter 2: **Literature Review**

Reviews existing literature on SAPs, microfluidic platforms for particle analysis, and the use of nanocomposites in environmental applications. This chapter establishes the context for research, highlighting knowledge gaps and opportunities for innovation.

Chapter 3: **Materials and Methods**

Describes the materials, synthesis methods, and experimental procedures used in the research, including the design and fabrication of the microfluidic platform and the synthesis of MXene/SAP-MPs. Details of characterization techniques and statistical analyses

employed are also provided.

Chapter 4: Microfluidic platform for characterization of SAP-MPs

Presents the design, fabrication, and characterization of the microfluidic platform for SAP-MPs, including the analysis of their swelling behavior.

Chapter 5: Parametric Investigation of SAP-MPs

Discusses the effects of particle size, crosslinker concentration, monomer concentration, and neutralization degree on the swelling behavior of SAP-MPs, utilizing the developed microfluidic platform. Key findings are related to the structure-to-property relationships of SAP-MPs, providing insights into parameter optimization.

Chapter 6: **Synthesize MXene Nanoparticles and Evaluate its Application for Bacterial Enrichment in Water Samples**

Explores the synthesis of MXene nanoparticles, the development of MXene/SAP-MPs, and their application in bacterial enrichment for water analysis. Performance metrics of bacterial enrichment are analyzed and discussed, with comparisons to conventional methods.

Chapter 7: **Conclusion and Future Work**

Summarizes the key findings, discusses their implications, and proposes directions for future research. Future work focuses on scaling the methodologies and expanding the applications of MXene/SAP-MPs in diverse environmental conditions.

Chapter 8: **Contributions**

Outlines the significant contributions of this research to the field of SAPs-MPs,

microfluidics, and environmental applications. The impact of these contributions on advancing SAP technology and analytical methodologies is highlighted.

1.7 Publication Contribution

This thesis is primarily based on papers co-authored by the PhD candidate (Section 8-3). The following outlines my specific contributions:

The contents of Chapters 3–6 have been derived from published and submitted journal papers [14, 25, 26]. I was responsible for designing and performing all experiments, which included conceptualizing the study, device design and implementation, and conducting data analysis. I drafted the original manuscripts and prepared the initial responses to reviewers, which were subsequently revised by Prof. Pouya Rezai and Prof. Siu Ning Leung.

Prof. Pouya Rezai and Prof. Siu Ning Leung provided critical support for the conceptualization and refinement of device designs, offering valuable feedback to guide the research. They also reviewed the original drafts of both conference proceedings and journal submissions. Dr. Alireza Zabihihesari contributed to developing computational codes, conducting numerical analyses, and reviewing manuscripts across various papers.

Chapter 2

Background and Literature Review

2.1 Superabsorbent Polymers (SAPs)

Hydrogels are polymeric materials with three-dimensional hydrophilic network structures, capable of absorbing up to 10 g/g of water [27]. Superabsorbent polymers (SAPs) represent a new class of loosely crosslinked hydrogels, enhanced with hydrophilic functional groups such as carboxyl (-COOH), sulfonic ($-SO_3H$), amine ($-NH_2$), and hydroxyl (-OH) groups, offering superior water absorption performance [28-30]. Figure 2-1 illustrates the general structure of superabsorbent polymers, highlighting their crosslinked polymer chains and functional groups.

The conceptual foundation for SAPs originated in the mid-20th century. The first-generation

water-swellable polymer hydrogel was synthesized from divinyl-benzene and acrylic acid by Kern in 1938. Later, in 1960, Wichterle and Lim [31] developed hydrogels from hydroxyalkyl methacrylate a 40–50% swelling capacity and found use in contact lenses for ophthalmic applications [31]. This achievement laid the groundwork for the emergence of second-generation hydrogels with improved swellability (70–80%), broadening their applications across diverse areas [32].

In the 1970s, The United States Agriculture Division, led by Zoila et al. [33], developed a starch-based SAP (starch-graft-poly(acrylonitrile)) for agricultural purposes. Despite their innovative nature, these SAPs faced challenges in terms of manufacturing costs and poor mechanical strength [33]. In the 1990s, Japan successfully commercialized the production of SAPs for hygienic applications, increasing SAP demand to 32,000 metric tons per year [34]. This commercialization spurred significant interest in SAPs, leading to further investigation of hydrogel networks, their characteristics, and their synthesis using natural and synthetic monomers [32].

In the 2000s, SAP technology research and development focused on improving performance, addressing environmental concerns, and exploring new applications [35, 36]. The development of biodegradable SAPs mitigated the environmental and health-related impacts of conventional SAPs. These innovations have broadened the potential applications of SAPs, including in drug delivery, tissue engineering, responsive coatings, etc. Recent advancements have also explored the functionality of SAPs, leading to the creation of smart SAPs that respond to external stimuli such as temperature, pH, and electric fields [27, 32, 37].

Ongoing research continues to push the boundaries of SAP technology, emphasizing sustainability and new functionalities to meet the requirements for various applications. Current research efforts focus on enhancing the sustainability and functionality of SAPs, ensuring their relevance and

adaptability to novel applications [32].

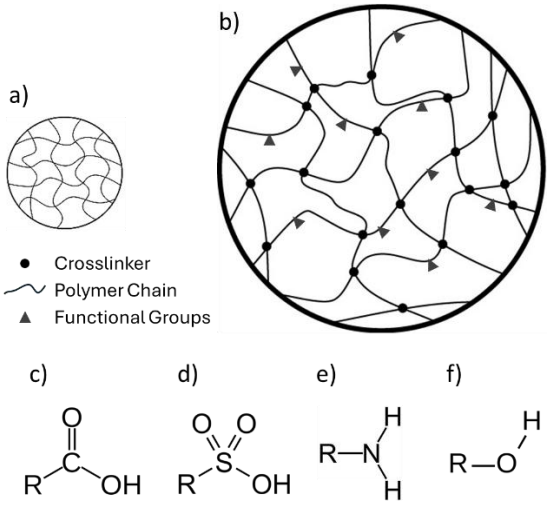

Figure 2-1. Schematic representation of the superabsorbent polymer structure in a) unswelled and b) swelled state and (c-f) examples of functional groups commonly incorporated in SAPs, including carboxyl (-COOH), sulfonic (-SO_3H), amine (-NH_2), and hydroxyl (-OH).

2.2 SAP Synthesis Methods

Various methods are employed to synthesize the SAPs. Synthesis methods include bulk polymerization, solution polymerization, suspension polymerization, and emulsion polymerization.

2.2.1 Bulk Polymerization

Bulk polymerization is the simplest technique in which monomers are polymerized by initiators, light, heat or radiation without the presence of solvents and dispersants (Figure 2-2a) [38]. This method achieves a high rate and degree of polymerization due to the high monomer concentration. However, the viscosity of reaction increases significantly and the heat result from polymerization is hard to spread. These limitations can be avoided by using lower temperature and reduced initiator concentration. The key advantage of bulk polymerization is that it produces high molecular weight polymers with high purity without complex devices [39].

2.2.2 Solution Polymerization

In solution polymerization, the monomers are mixed with the cross-linking agent and initiator. Polymerization is initiated by thermal, UV-irradiation, or a redox initiator. This method, depicted in Figure 2-2b, uses a solvent to act as a heat sink, mitigating issues seen in bulk polymerization. The presence of solvent is the major advantage of the solution polymerization over the bulk polymerization method to serve as a heat sink [39]. The prepared SAPs must be washed with distilled water to remove unreacted monomers, oligomers, cross-linking agents, initiators, and other impurities. Phase separation can occur, forming heterogeneous SAPs, when the water content during polymerization exceeds the equilibrium swelling capacity. This method has been used to prepare varieties of SAPs in the last decades [40].

2.2.3 Suspension Polymerization

Suspension polymerization is a method used to prepare spherical SAPs micro-particles with a size range of 1 μm to 1 mm. As shown in Figure 2-2c, this method involves dispersing a monomer solution (containing monomers, crosslinkers, and initiators) into an organic solution to form droplets [41]. Polymerization is initiated thermally, and the newly formed microparticles are then washed to remove unreacted components.

Inverse suspension polymerization is a modified method based on suspension polymerization, where monomers, crosslinkers, and initiators are soluble in an aqueous solution, forming droplets in an organic solution. This approach is particularly advantageous due to its fast processing time and high controllability on polymer particle size, making it an ideal choice for synthesizing SAP particles with specific size ranges and morphologies [42].

2.2.4 Emulsion Polymerization

Emulsion polymerization is another polymerization technique that enables the synthesis of SAP ranging from 10 to 500 nm [43]. This method involves a reaction system including monomers, surfactants, initiators, and water. The monomers, typically hydrophobic, are introduced into water and stabilized by surfactants, which self-assemble into micelles—small spherical structures with hydrophobic interiors. These micelles encapsulate the monomer molecules, serving as polymerization sites. A water-soluble initiator generates free radicals in the aqueous phase. These radicals diffuse into the micelles, where they initiate polymerization by reacting with the encapsulated monomers. As the reaction progresses, the micelles grow into polymer nanoparticles while remaining stably dispersed in the continuous aqueous phase. The resulting polymer can be used directly or further processed through coagulation, filtration, or spray drying to obtain dry SAP powders [44].

A key difference between emulsion polymerization and suspension polymerization lies in their dispersion mechanisms and polymerization environments. In suspension polymerization, all components—including monomers, initiators, and crosslinkers—are dispersed as droplets in an aqueous phase using mechanical agitation and stabilizers, with each droplet acting as an individual reaction site. Conversely, emulsion polymerization occurs exclusively in an aqueous medium, where monomers are stabilized by surfactants, and polymerization takes place inside the micelles formed by these surfactants. Suspension polymerization produces larger, porous polymer beads, making it ideal for absorbent applications, such as in diapers and agricultural water retention. In contrast, emulsion polymerization enables precise control over particle size and molecular weight, making it particularly suitable for coatings, adhesives, biomedical SAPs [45].

2.3 Classification of SAPs

This section categorizes SAPs based on their building blocks, cross-linking mechanisms, electrical charges, and responsiveness to environmental stimuli. These classifications highlight the diversity of SAPs, their synthesis approaches, and their tailored functionalities for various applications.

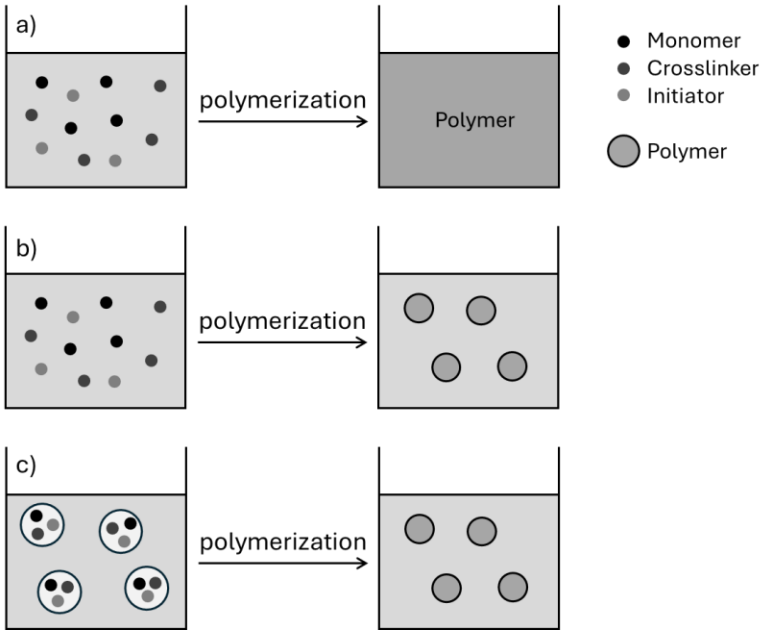

Figure 2-2. Schematic representations of SAP synthesis methods: a) Bulk polymerization, where monomers and initiators directly polymerize without solvents; b) Solution polymerization, where a solvent facilitates the reaction as a heat sink; and c) Suspension polymerization, showing the formation of droplets in an organic solution to produce spherical SAP particles.

2.3.1 Classification Based on General Building Blocks

The main building blocks of an SAP can be synthetic, natural, or a combination of both. Synthetic SAPs are typically synthesized from petrochemically-based monomers such as acrylates or acrylamides. These SAPs often exhibit high mechanical strength, making them suitable for applications requiring robust performance, such as construction and personal hygiene products. However, synthetic SAPs may suffer from limited reaction control and high polydispersity.

Natural SAPs, on the other hand, are derived from biopolymers such as polypeptides and

polysaccharides like chitosan. These SAPs are readily available, non-toxic, and sustainable, making them ideal for applications like agriculture and biomedicine. However, they often lack the mechanical properties needed for demanding applications.

Semi-synthetic SAPs combine natural and synthetic building blocks to balance sustainability, biocompatibility, and mechanical strength. They are widely used in specialized applications, such as tissue engineering and responsive materials. Recent advancements, such as bio-inspired polymerization, are enhancing the control over synthetic SAPs while improving the strength and stability of natural and semi-synthetic variants [2, 32].

2.3.2 Classification Based on Cross-Linking Mechanisms

SAPs can be categorized into physically cross-linked and chemically cross-linked types. Physical bonds, such as hydrogen bonds, ionic interactions, van der Waals forces, or molecular entanglements, are relatively weak (typically several kJ/mol). Physically cross-linked SAPs are often formed without the use of chemical cross-linkers, relying instead on molecular interactions to create the network structure.

Chemically cross-linked SAPs, in contrast, form strong covalent bonds (>100 kJ/mol). They are often synthesized through free radical polymerization, using either natural functionalized starting materials or synthetic cross-linkers. These SAPs exhibit high mechanical stability, making them suitable for robust applications such as structural hydrogels. Advances in hybrid cross-linking mechanisms combine physical and chemical bonds, leveraging the elasticity of physical interactions with the strength of covalent linkages [2, 32].

2.3.3 Classification Based on the Type of Electrical Charges

SAPs can be classified into four types based on the presence of electrical charges along their

polymer backbone or side chains.

- **Non-ionic SAPs**: These lack any charges and are often used in neutral or inert applications, such as agarose-based hydrogels.
- **Ionic SAPs**: These include anionic or cationic polymers like synthetic acrylates and alginate, which carry negative or positive charges, respectively. Ionic SAPs are widely utilized in biomedical and wastewater treatment applications due to their ability to interact with oppositely charged molecules.
- **Ampholytic SAPs**: These contain both acidic and basic groups, enabling them to respond to pH changes, making them suitable for stimuli-responsive systems.
- **Zwitterionic SAPs**: These SAPs possess both anionic and cationic groups, resulting in a net charge of zero. They are gaining prominence in medical devices and membranes for their superior anti-fouling properties.

The charge properties of SAPs determine their interactions with target molecules and influence their swelling behavior, making this classification critical for application-specific SAP design [2, 32].

2.3.4 Classification Based on the Environmental Stimuli ('Smart' SAPs)

Certain SAPs undergo distinct physical changes in response to minor environmental variations, earning them the designation of "smart" polymers. These polymers respond to stimuli such as pH, temperature, light, or electric fields.

- **Thermo-Sensitive SAPs**: These SAPs respond to temperature changes, exhibiting either lower critical solution temperature (LCST) or upper critical solution temperature (UCST) behavior. Below the LCST, the SAP swells due to hydrophilic interactions, while above the

LCST, it contracts. Positive temperature-sensitive SAPs, conversely, swell above the UCST. Examples include chitosan, cellulose, and interpenetrating networks of poly(acrylic acid) and poly(acrylamide). Tailoring LCST or UCST is possible through structural modifications or the inclusion of specific additives.

- **pH-Sensitive SAPs**: These SAPs respond to environmental pH, leveraging functional groups such as carboxylic acid or amine functionalities. Anionic SAPs swell when solution pH exceeds their pKa due to electrostatic repulsion, while cationic SAPs swell at low pH when their amine groups protonate.
- **Photo- and Electro-Sensitive SAPs**: Photo-sensitive SAPs respond to specific light wavelengths, with examples including UV-responsive hydrogels. Electro-sensitive SAPs, composed of polyelectrolytes, exhibit swelling or bending behavior under applied electric fields. These SAPs are used in advanced applications like microfluidics, drug delivery, and sensors [2, 32].

2.4 SAP Morphology

SAPs can be synthesized in various morphological forms, including fibers, powders, granules, and sheets. The choice of morphology is often dictated by the intended application. For example, fibers are preferred for composite materials, while powders and granules are commonly used in agriculture and hygienic products. Sheets may be applied in wound dressings or filtration membranes.

It is crucial that the original shape of an SAP remains unchanged upon water uptake. SAPs must exhibit sufficient mechanical strength to resist physical degradation, even under pressure, ensuring consistent performance. For instance, in agricultural applications, granular SAPs must maintain

integrity to support sustained water release into the soil. Powder and granule SAPs are typically manufactured via solution polymerization due to its scalability and ability to produce uniform particles [37].

2.5 SAP Applications

SAPs have tunable structures and properties, making them perfect materials for a wide range of applications. These applications expand across various fields, including agriculture, drug delivery, tissue engineering, construction, water purification, and biological sample enrichment [7, 9, 46-48]. To perform effectively in these fields, SAP particles must meet application-specific requirements, such as high water absorption capacity, controlled absorption and desorption rates, non-toxicity, reusability, and stimuli-responsiveness [30].

In agriculture, SAPs play a crucial role in improving soil moisture management by absorbing and retaining water, reducing irrigation frequency and overall water usage. They can also be integrated into soil amendments and fertilizers to enhance nutrient uptake by plants, leading to better crop yields and resource efficiency [49].

In biomedical and pharmaceutical applications, SAPs are utilized for drug delivery and tissue engineering due to their ability to respond rapidly to changes in environmental conditions such as pH, temperature, and enzyme presence. For instance, SAPs swell or deswell in response to specific stimuli, enabling controlled drug release and supporting tissue regeneration processes [28].

In the construction industry, SAPs are added to concrete to improve workability, reduce cracking, and enhance durability. Additionally, they act as moisture barriers in construction materials, preventing water ingress and minimizing structural damage [3].

In water purification processes, SAPs play a vital role in environmental remediation efforts. Their

high absorption capacity allows them to effectively remove various contaminants, such as positively charged pollutants, heavy metal ions, and dyes, from wastewater. This functionality contributes to cleaner water sources and reduced environmental pollution [50].

Recent advancements have seen SAPs being employed in biological sample enrichment and target capture applications. They selectively bind with target molecules or analytes, concentrating them for subsequent analysis or detection. SAPs can also repel unwanted targets, leaving them behind while isolating specific molecules. This dual functionality makes SAPs versatile for enrichment applications in areas such as proteomics, bacterial detection, and biomarker discovery. For effective performance in these roles, SAPs must possess not only high water absorption capacity but also fine-tuned characteristics, such as small surface pore size, selective absorption capability, and a high surface charge [7, 9].

2.6 Swelling Process of SAPs

The swelling process of SAPs begins with the penetration of solvent molecules into the polymer network. This causes the molecular chains between the cross-linked points to expand, reducing the configuration enthalpy value. Simultaneously, the polymer network exerts an elastic contractive force, attempting to restore the network to its original state. When these opposing forces reach equilibrium, swelling is stabilizes, and the polymer achieves a balance between osmotic pressure driving expansion and the elastic restoring force resisting it [51].

The swelling behavior of SAPs is often explained by the Flory theory of ionic networks. This theory assumes that the polymer network is uniformly cross-linked with evenly distributed cross-link points and that polymer segments interact with solvent molecules based on the Flory-Huggins interaction parameter (χ). It further assumes that the total volume of the swollen gel equals the

sum of polymer and solvent volumes and that swelling occurs at thermodynamic equilibrium. Importantly, the ionic strength of the solution impacts the osmotic pressure due to the charged groups on the polymer backbone, influencing the swelling process [51].

Two primary forces govern the swelling equilibrium. Osmotic pressure, arising from ion concentration differences inside and outside the polymer network, drives solvent absorption. This pressure is influenced by the ionic strength (S) of the external solution and the charge density (i) on the polymer. The elastic restoring force, on the other hand, is generated by the deformation of the polymer network during swelling. It is characterized by the cross-linking density (v) and the initial volume of the polymer (V_0). Together, these forces determine the equilibrium swelling ratio (Q) of the polymer [51].

The swelling ratio can be calculated using the modified Flory equation [51]:

$$Q^{\frac{5}{3}} = \left[\left(\frac{i}{2 \times V_u \times S^{\frac{1}{2}}}\right) + \frac{\left(\frac{1}{2} - X\right)}{V_1}\right] \times {}^{v}/_{V_0} \tag{2-1}$$

where Q is maximum water absorbency (g/g); i is ionic charge per polymer unit; V_u is volume of structural unit; S is ionic strength of solution; X is polymer-solvent interaction parameter; V_1 is molar volume of solvent; v is effective number of chains (cross-linking density); and V_0 is volume of un-swelled polymer.

The performance of SAPs in swelling applications can be optimized by adjusting key parameters. Reducing the cross-linking density decreases the elastic restoring force, enhancing water absorption but potentially compromising mechanical strength. This approach is often employed in agricultural hydrogels, where water retention is prioritized over structural integrity. Increasing the

fixed charge density amplifies osmotic pressure, improving absorption in high-salinity environments, such as in diapers or saline-rich soils. Additionally, modifying the polymer-solvent interaction parameter (χ) allows for tailoring SAP behavior for specific applications, such as biomedical uses requiring precise swelling in physiological conditions [51].

The polymer-solvent interaction parameter (χ) is a dimensionless measure of the compatibility between a polymer and a solvent. It balances the enthalpic and entropic contributions to their mixing. A lower χ value indicates stronger polymer-solvent interactions, resulting in enhanced swelling or dissolution, while a higher χ value reflects poor compatibility, favoring polymer-polymer interactions and reducing swelling [51].

While the Flory theory provides a robust framework for understanding SAP swelling, it has limitations. Real-world SAPs often exhibit heterogeneous cross-linking, leading to deviations from theoretical predictions. Similarly, in highly concentrated salt solutions, osmotic pressure behavior diverges from the idealized model. Complex solvent interactions, such as those involving multi-component systems, can also challenge the theory's assumptions. Despite these limitations, the Flory theory remains a valuable tool for predicting and optimizing SAP performance in diverse applications [51].

2.7 Swelling Characterization

Swelling behavior, consisting of absorption capacity (AC) and swelling rate, is one of the most important properties that gives SAPs a wide range of applications. AC refers to the maximum amount of fluid or solvent that an SAP can absorb under specific conditions. It characterizes the effectiveness of SAPs in absorbing and retaining liquids, such as water or aqueous solutions. SR indicates the speed at which an SAP absorbs a solvent and reaches its equilibrium swelling

capacity. Initially, the SR is at its maximum due to the high osmotic pressure, but it decreases over time as the polymer network swells and the forces reach equilibrium [52-54].

Various methods can be used to measure AC and SR. AC can be determined using volumetric or gravimetric methods. The volumetric method calculates the volumetric swelling ratio (VSR) by measuring changes in the SAP sample's volume before and after absorption. The gravimetric method measures mass changes of SAP samples. SR is derived from AC measurements, such as measuring SAP size at intervals during the swelling process using volumetric methods [2, 55].

The AC and SR of SAPs are governed by various factors, which can be categorized into two main groups: polymer-related factors and solution-related factors.

2.7.1 Polymer Related Factors

2.7.1.1 Chemical structure

Swelling behavior of SAPs are define by the presence of hydrophilic groups, such as hydroxyl (-OH), amide (-CONH- and -$CONH_2$), and sulfonic acid (-SO_3H), which influence *X*, the polymer-solvent interaction parameter in Eq2-1. Higher ratios of hydrophilic to hydrophobic groups increase *X*, improving AC and SR by enhancing polymer-solvent compatibility. Conversely, hydrophobic groups reduce *X*, causing the polymer to collapse in water and lowering AC and SR [56-59].

2.7.1.2 Crosslinking ratio

The cross-linking ratio refers to the proportion of cross-linking agents relative to the monomers in the polymer. This ratio determines the cross-linking density (ν) in the Flory Eq (2-1). Higher cross-linking ratios result in increased ν, leading to greater structural density and reduced polymer chain flexibility. This restricts the extent of swelling, lowering AC and SR, but enhances mechanical

strength. Conversely, lower cross-linking ratios decrease ν, creating a looser network that improves AC and SR but compromises mechanical integrity. The nature of the cross-linker also plays a crucial role, as hydrophilic cross-linkers improve water affinity, influencing both ν and the polymer-solvent interaction parameter (X) in the Flory equation [60-63].

Recent rheological studies indicate that beyond an optimal cross-linking concentration, further increasing the cross-linker ratio does not significantly increase the mechanical properties of the polymer. According to Adibnia and Hill [64], there exists an optimal cross-linking threshold beyond which additional cross-linking agents do not contribute effectively to the network structure. Instead, an excess of cross-linker leads to the formation of dangling chains and ineffective cross-links, which do not contribute to elasticity. As a result, the polymer becomes increasingly brittle due to partial chain stretching [64].

2.7.1.3 Neutralization degree

ND refers to the ratio of sodium ions (Na^+) to ionizable functional groups on the polymer chain (e.g., carboxylic acid groups (-COOH)), determined by the amount of sodium hydroxide (NaOH) used to neutralize acrylic acid (AA) during pre-polymerization [65, 66].

ND influences the ionic charge density (i) and osmotic pressure in the Flory Eq (2-1). At low ND, reduced electrostatic repulsion and lower osmotic pressure limit swelling. Increasing ND enhances i, leading to network expansion and improved AC and SR. However, beyond a certain threshold, counterion condensation (screening effect) reduces electrostatic repulsion and osmotic pressure, causing AC and SR to decline [67].

ND also increases the ionic strength (S) of the solution, further reducing osmotic pressure and

swelling capacity due to Donnan equilibrium effects. Thus, ND must be optimized to balance electrostatic repulsion, osmotic pressure, and network flexibility for maximum swelling performance [62, 68].

2.7.1.4 Initiator concentration

Initiator concentration, defined as the molar or weight ratio of the initiator agent to monomer(s), significantly influences the polymerization process by affecting polymer chain length, network connectivity, and mechanical properties. Higher initiator concentrations promote rapid polymerization, leading to the formation of shorter polymer chains. While this does not directly increase the cross-linking density (ν), it produces a greater number of chain ends, which can influence network formation and structural integrity. A high concentration of shorter polymer chains limits entanglement and reduces network cohesion, potentially restricting the swelling capacity (AC) and swelling ratio (SR) by decreasing the polymer's ability to expand [69, 70].

Conversely, lower initiator concentrations slow the polymerization rate, allowing monomer chains to grow longer before termination occurs. This facilitates the development of a more interconnected and flexible network with larger free volumes, enhancing AC and SR. However, excessively low initiator concentrations may result in incomplete polymerization, leading to weaker and less stable networks [69, 70].

At high initiator concentrations, the increased number of polymer chain ends further reduces swelling efficiency, as chain ends contribute less to swelling compared to the central portions of the polymer network [69, 70]. Thus, initiator concentration plays a critical role in determining polymer molecular weight and network architecture, ultimately influencing the SAP's swelling behavior and mechanical stability.

2.7.1.5 Nanoparticles and Additives

Nanoparticles enhance the properties of SAPs by modifying key parameters in the Flory equation, such as cross-linking density (v) and polymer-solvent interaction (X). Clays and MXene improve hydrophilicity, increasing *X*, which enhances swelling behavior, while carbon nanotubes (CNTs) increase v, improving structural integrity. These modifications allow SAPs to meet specific application requirements, such as improved swelling and mechanical strength in biomedical systems.

Incorporating nanoparticles into SAPs forms composites or nanocomposites that improve swelling behavior, mechanical strength, thermal stability, responsiveness, and surface properties [71]. Clays, due to their availability, low cost, and mechanical reinforcement capabilities, are commonly used to improve both absorption capacity and mechanical stability [72, 73]. Clay nanoparticles act as multifunctional cross-linkers, modifying the network structure by decreasing the polymer chain length between crosslinking points, leading to a more tightly crosslinked network. This structural modification enhances mechanical properties without substantially affecting the polymer's affinity for water [72, 73]. Metal nanoparticles, such as silver and gold, add functionalities like antibacterial properties [74], while CNTs primarily enhance mechanical strength and electrical conductivity rather than swelling behavior [75]. Graphene contributes exceptional mechanical, thermal, and electrical properties, enabling the creation of multifunctional hydrogels [76].

MXene, a novel 2D nanomaterial, offers unique advantages, including high electrical conductivity, hydrophilicity, and tunable surface chemistry. These properties make MXene an excellent additive for SAPs, particularly in advanced applications such as environmental remediation and biomedical systems. MXene's hydrophilic nature enhances the polymer-solvent interaction, influencing both swelling performance and mechanical properties. Among the nanomaterials discussed, MXene will

be examined in greater detail in subsequent sections [16, 17]. Detailed discussion is provided in Section 2-8.

2.7.2 Solution Related Factors

Swelling behavior of SAPs is also affected by their surrounding medium. Therefore, the SR and AC can be altered by changing ionic strength, pH, and temperature of the swelling medium [58, 60].

2.7.2.1 Ionic Strength

Ionic strength (IS) is a key parameter in the Flory equation that influences the swelling behavior of SAPs. It quantifies the concentration of ions in a solution and is calculated using the formula:

$$I = \frac{1}{2}\sum_i c_i z_i^2 \qquad (2\text{-}2)$$

where c_i and z_i represent the molar concentration and the charge number of each ion species, respectively.

Higher ionic strength reduces the osmotic pressure gradient that drives water into the SAP network, as described by the Donnan equilibrium theory. This reduction in osmotic pressure decreases the electrostatic force within the polymer network, ultimately lowering AC and SR. In saline environments, the elevated IS causes the equilibrium between charges to be reached more quickly, significantly reducing AC.

SAPs are particularly sensitive to ionic strength, which directly impacts the balance of osmotic forces. Higher ionic strength leads to fewer water molecules being absorbed into the network, limiting the swelling potential of SAPs. For example, in high-saline conditions, the reduced osmotic gradient hinders swelling efficiency [37, 77-79].

2.7.2.2 Solution Temperature

Temperature impacts the polymer-solvent interaction parameter (X) in the Flory equation, which governs the swelling behavior of thermo-responsive SAPs. Negative temperature-sensitive SAPs swell below their LCST, where X favors hydrophilic interactions and promotes water absorption. Examples include chitosan, cellulose, and poly(N-isopropyl acrylamide) [58, 60].

In contrast, positive temperature-sensitive SAPs swell above their UCST, as X shifts to favor polymer-solvent compatibility at higher temperatures. Polymers such as poly(acrylic acid) and poly(acrylamide) exhibit this behavior. This thermo-responsiveness makes these SAPs valuable for applications requiring precise swelling control, such as in smart drug delivery systems and stimuli-responsive hydrogels.

2.7.2.3 Solution pH

Solution pH affects the swelling behavior of SAPs by influencing the ionic charge density (i) in the Flory equation. Functional groups within the polymer network, such as carboxylic acid, sulfonic acid, or amine groups, respond to changes in pH, altering their ionization states and affecting swelling capacity.

At high pH, anionic SAPs containing carboxylic or sulfonic acid groups exhibit increased ionization, leading to higher i. This enhances osmotic pressure, resulting in greater AC. Conversely, at low pH, cationic SAPs with amine functionalities become protonated, increasing i and producing similar swelling effects. These pH-responsive behaviors make SAPs particularly useful in stimuli-sensitive applications, such as controlled drug delivery and environmental sensors [58, 60].

2.8 Mechanical Properties of SAPs

Mechanical stability is another crucial factor for SAP applications, particularly in biomedical, environmental, and industrial sectors where SAPs must withstand external stresses without disintegration. The mechanical properties of SAPs are primarily determined by their Cr, AA content, and ND, all of which influence polymer network structure, elasticity, and toughness [80].

2.8.1 Chemical structure

AA is a primary monomer in SAP synthesis, and its concentration affects both swelling behavior and mechanical stability. As previously discussed, increasing the AA content enhances the polymer's hydrophilicity, allowing SAPs to absorb more water. However, an excessively high AA concentration weakens the mechanical structure due to overexpansion of the polymer network. At low AA concentrations, the polymer structure remains rigid and stable, resulting in a hydrogel with higher tensile strength and reduced elasticity. Conversely, excessive AA content increases the osmotic pressure inside the gel, leading to excessive expansion and network destabilization. This can cause the gel to rupture under stress, compromising its mechanical integrity. Thus, the AA content must be optimized to maintain a balance between swelling behavior and mechanical durability, ensuring the hydrogel remains structurally intact during repeated absorption cycles [81].

2.8.2 Crosslinking ratio

Cr significantly impacts the elasticity, toughness, and resilience of SAP networks. A higher Cr increases the cross-linking density (ν), forming a denser polymer network with reduced segmental mobility. This enhances mechanical strength and modulus, making the hydrogel more resistant to deformation but also more brittle. As polymer chains become more rigid, the hydrogel loses elasticity, which can lead to cracking under external stress. Conversely, a lower Cr results in fewer

cross-links, producing a more flexible and extensible network. While this enhances elasticity, it also weakens structural integrity, making the SAP more prone to mechanical failure under load. To achieve both high absorption and mechanical durability, a balance must be maintained between cross-linking density and network flexibility [82, 83].

2.8.3 Neutralization degree

ND of acrylic acid influences charge density, electrostatic interactions, and mechanical stability in SAPs. A higher ND increases the concentration of ionized carboxylate groups ($-COO^-$), generating stronger electrostatic repulsions within the polymer network. This repulsion expands the gel structure, increasing AC and SR. However, excessively high ND levels can lead to counterion condensation effects, reducing the effective charge repulsion within the network. This phenomenon weakens electrostatic interactions, causing the network to collapse and significantly decreasing mechanical stability. As a result, SAPs with very high ND levels may exhibit reduced swelling efficiency and increased fragility [80].

2.9 MXene Functionalized SAPs

In recent years, significant research has focused on enhancing the performance of SAPs by incorporating nanomaterials. These nanomaterials improve the structural, mechanical, and functional properties of SAPs, expanding their efficiency in various applications. Commonly used nanomaterials include carbon-based nanostructures such as graphene oxide (GO) [84], metals like silver nanoparticles [85], and clay minerals like laponite [86, 87]. These nanomaterials offer unique advantages, such as increased surface area, improved water retention, and enhanced mechanical strength.

MXenes have emerged as a particularly promising class of two-dimensional (2D) materials for

SAP enhancement due to their exceptional conductivity, hydrophilicity, and surface functionalization capabilities. MXenes, first discovered in 2011 by researchers at Drexel University [88], are transition metal carbides, nitrides, and carbonitrides with a general formula of $M_{n+1}X_nT_x$, where M represents transition metals (such as Sc, Ti, Zr, Hf, V, Nb, Ta, Cr, Mo, etc.), X is carbon and/or nitrogen, and 'T_x' denotes surface terminations such as –O, –OH, and –F [89]. These materials are synthesized from layered MAX phases ($M_{n+1}AX_n$), where A represents elements from groups 13 or 14 in the periodic table. During the synthesis of MXene, various functional groups become attached to their surfaces, primarily due to the etching process and subsequent exposure to different environments. For instance, when hydrofluoric acid (HF) is used for etching, fluoride (–F) terminations are introduced. Additionally, hydroxyl (–OH) and oxygen (–O) groups can form upon exposure to water and air, leading to oxidation of the MXene surface. The specific types and distributions of these surface terminations are influenced by the synthesis methods and post-treatment conditions, and they play a crucial role in determining the electronic properties and stability of MXene [89].

MXenes are characterized by excellent metallic conductivity, hydrophilicity, large specific surface area, and mechanical strength, with tunable electronic and optical properties through surface functionalization. These features make MXenes suitable for a wide array of applications, including energy storage (e.g., batteries, supercapacitors), catalysis, chemical and biological sensors, water treatment, and biomedicine (e.g., antibacterial coatings, drug delivery, bioimaging) [16, 90-92].

2.9.1 MXene Synthesis Methods

MXenes are typically synthesized through the selective etching of the aluminum (Al) element from their parent MAX phases. Figure 2-3 illustrates the stepwise process of MXene synthesis,

including etching, intercalation, and delamination. The most common method involves wet chemical etching using hydrofluoric acid (HF) or a combination of hydrochloric acid (HCl) and fluoride salts, such as lithium fluoride (LiF). This process removes the Al layers, resulting in the formation of MXenes with a layered structure.

After etching, MXenes are often intercalated with organic or inorganic species to increase the interlayer spacing, which reduces the van der Waals forces between the layers and prepares the material for further processing. Following intercalation, delamination, or the separation of these expanded layers into single or few-layer nanosheets, is achieved through methods such as sonication or manual shaking in suitable solvents. These steps are critical for improving MXene properties, such as enhancing their dispersibility and compatibility in composite systems [93].

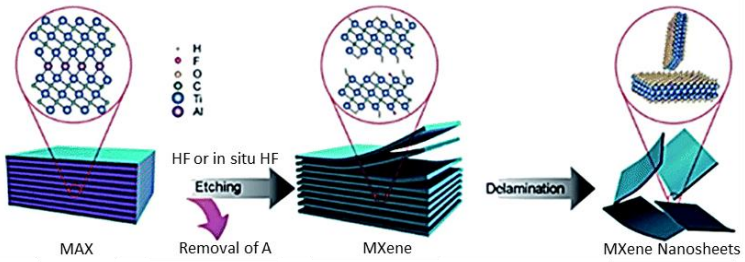

Figure 2-3. Schematic representation of MXene synthesis. The process involves (i) etching of the 'A' element from the MAX phase using HF or in situ HF generation, leading to the formation of MXenes, and (ii) delamination into single or few-layer MXene nanosheets, improving their structural and functional properties. Reprinted with permission from Elsevier [94].

2.9.2 MXene-polymer Nanocomposite

Combining MXenes with polymers has led to the development of MXene/polymer nanocomposites that integrate the unique properties of both components. These composites enhance the performance of SAPs by improving swelling behavior, mechanical properties, and functional responsiveness. MXene/polymer nanocomposites can be synthesized using various methods [95-97]:

Physical Mixing: MXene and polymers are blended to form composites, where the abundant surface functional groups on MXenes (e.g., hydroxyl groups) form hydrogen and electrostatic bonds with hydrophilic polymer groups, enhancing compatibility [98].

Surface modification: To address challenges such as MXene instability and poor compatibility with hydrophobic polymers, surface modification adjusts the hydrophilicity/hydrophobicity of MXene, improving its distribution in the polymer matrix and enabling chemical crosslinking [99-102].

In Situ Polymerization: Monomers, cross-linkers, and initiators are mixed with MXene nanosheets and polymerized to produce well-integrated composites. This method ensures uniform MXene dispersion within the polymer matrix [103-105].

Breathing-In Breathing-Out Method: This technique utilizes the swelling and deswelling properties of hydrogels to absorb MXene layers into the polymer network, improving interaction and compatibility between the two materials. The process begins by dispersing MXene into a water solution. SAP particles are then introduced into the MXene dispersion, allowing them to swell and incorporate MXene layers into their polymer network. The hydrogels absorb water along with dispersed MXene layers during the swelling phase. Subsequently, during the deswelling phase, water is partially removed, locking the MXene layers within the hydrogel matrix. Repeating this swelling and deswelling cycle further enhances the integration and distribution of MXene layers within the polymer, creating a hybrid material with improved compatibility and optimized performance [106].

These composites exhibit enhanced properties such as higher swelling capacity, improved mechanical stability, and better responsiveness, enabling their application in energy storage

devices, electromagnetic shielding, sensors, and water treatment [16, 97].

In water treatment, MXene/hydrogel composites, such as MXene/Sodium Alginate and MXene/Acrylic Acid, demonstrate superior adsorption properties for organic dyes like methylene blue and methyl orange. These materials provide sustainable and eco-friendly solutions for removing pollutants from water. Beyond water purification, MXene/polymer composites show potential in sample enrichment and detection, leveraging their high conductivity and surface area for enhanced performance [21, 22].

2.10 SAP Characterization

SAPs require comprehensive characterization to optimize their performance for various applications. Characterization methods can be categorized into physical, chemical, and swelling characterizations, each providing critical insights into SAP properties.

2.10.1 Physical and Chemical Characterization

Physical and chemical characterizations employ techniques to reveal the structural and compositional details of SAPs. For example, scanning electron microscopy (SEM) examines surface morphology and particle size, offering detailed images of the SAP's structure, and Fourier transform infrared spectroscopy (FTIR) identifies functional groups and chemical bonds within the SAP, providing insights into its chemical framework.

2.10.2 Swelling Characterization

Swelling characterization focuses on understanding the absorption properties of SAPs, specifically the swelling ratio, kinetics, and equilibrium swelling. Multiple methods are utilized:

Gravimetric methods: Measure and compare the mass of SAP samples before and after swelling. For macro-sized SAP samples, the sample is immersed in a solution, then removed, gently cleaned,

and dried with a napkin to eliminate excess surface water before weighing. As shown in Figure 2-4a, the "tea-bag" method is a common gravimetric approach for microparticles, where SAPs are enclosed in a permeable bag and immersed in a solution. This straightforward approach provides rapid results but may overestimate swelling due to interstitial liquid, especially in microparticles. The "tea-bag" method is often used for microparticles, where SAPs are enclosed in a permeable bag and immersed. However, this method may not capture swelling kinetics accurately [107, 108].

Optical methods: Track size changes during swelling and are effective for larger particles. Figure 2-4b illustrates size tracking through microscopy during swelling, offering visual insight into SAP swelling behavior. Direct observation and measurement using microscopy or image analysis provide useful data, but tracking individual microparticles remains challenging, compromising precision.

Microfluidic Methods: Recently, (in this research) microfluidics has emerged as an innovative approach for characterizing SAP microparticles (SAP-MPs). These techniques manipulate fluids at the microscale using microchannels, enabling precise control and real-time analysis of SAP behavior. Figure 2-4c depicts the design and operation of a microfluidic system, highlighting particle traps that enable swelling characterization under controlled conditions. However, traditional microfluidic devices struggle to accommodate the substantial size changes of SAP-MPs, which can swell significantly within minutes. Developing modified microfluidic systems tailored for SAP-MPs is crucial to improving accuracy in small SAP characterization [109-111].

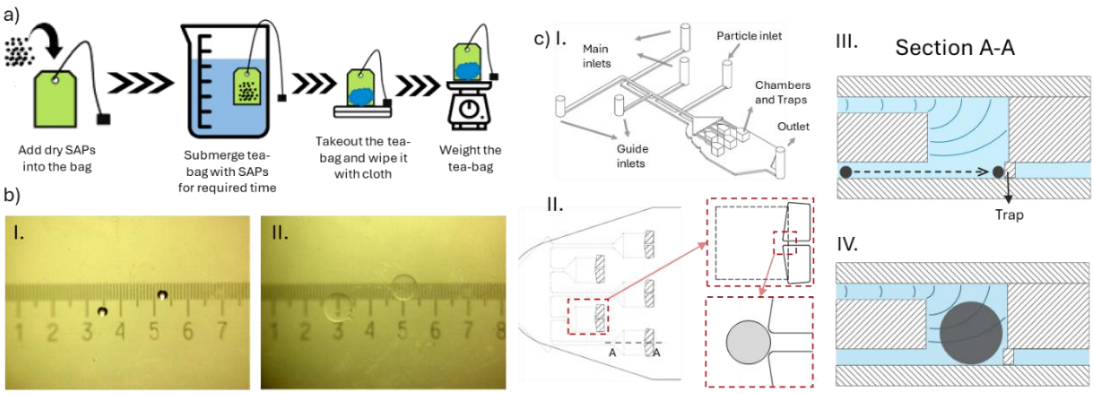

Figure 2-4. Methods for SAP swelling characterization. a) The "tea-bag" method for gravimetric measurement of swelling. b) Microscopy images showing SAP particle size before (I) and after (II) swelling. c) Microfluidic system for SAP swelling analysis, including (I) microfluidic channel design, (II) trap layout, (III) cross-section showing particle trap operation, and (IV) SAP behavior during swelling Reprinted with permission from Elsevier [12, 14, 112].

2.10.3 Challenges in Traditional SAP Characterization Methods

Traditional characterization methods often focus on macro-scale SAPs or bulk samples, potentially overlooking the complexities of small SAP particles [7]. Studies on AA-Aam-based SAPs in the 300–500 µm range underscore the impact of particle size variability on swelling behavior [12], highlighting the need for further research into the effects of size and composition heterogeneity.

SAP characterization traditionally relied on the gravimetric method. However, with the use of SAPs in micro size and various applications, characterizing them using traditional methods has become challenging, resulting in conflicting findings. The following text provides a critical review of conflicting findings in the literature regarding the effect of particle size on the swelling ratio of SAPs and emphasizes the importance of single-particle characterization for accurate assessment.

Omidian et al. [13] prepared acrylic acid-acrylamide SAPs in order to investigate the dependence of absorption characteristics on particle size. They categorized the SAPs into two size groups: 250-300 µm and finer than 250 µm. The larger particles were spherical, while the finer particles, derived from grinding larger pieces, were irregularly shaped. The characterization of swelling

behavior was performed by dispersing 1 g of SAPs into 2 L of distilled water and allowing them to swell overnight. Equilibrium swelling was determined by filtering the swollen samples through a 100-mesh wire gauze, carefully drying the surface water using a piece of soft open-cell polyurethane foam and weighing the samples. For swelling rate measurements, samples were taken from the solution at different intervals and examined using the same procedure. The results indicated that both the swelling rate and the equilibrium swelling ratio increased as the particle size decreased. The increased swelling rate was attributed to the higher surface area to volume ratio of the particles, and the increased swelling ratio was attributed to more water being held in the interstitial volume between the particles [13].

In contrast, Estivens [12] investigated the swelling behavior of acrylamide SAPs in the size range of 50 to 500 μm using an optical method without any trapping system to stabilize the SAP particles during swelling. They used microscopes with different magnifications to measure the average particle size during swelling at different time intervals, capturing images every 10 minutes. Although this method lacked accuracy, it provided useful insights into the swelling characterization of SAP-MPs. Their results demonstrated that the particle size significantly influences the swelling rate. Smaller particles swelled faster, with 50 μm particles reaching volumetric equilibrium in less than 1 minute, while particles larger than 300 μm took more than 20 minutes. Moreover, the swelling ratio was found to be diameter-dependent: larger particles absorbed more fluid relative to their original mass. This suggested that the cross-linked structure of the SAPs might change depending on particle size, with smaller particles having a proportionally larger surface zone (shell) and a smaller nucleus (core), resulting in lower absorption due to less active surface zones compared to the bulk [12]. In other research works, results indicated that the particle size significantly increased the swelling rate of SAPs, but it did

not affect the swelling ratio of the SAPs. The summary of the findings from these papers is shown in Table 2-1.

Table 2-1. Comparative Summary of Studies on SAP characterization

SAP Type	Particle Size Range	Effect on VSR	Effect on SR	Reason for Claims
AA-Aam	250-300 µm (spherical) finer than 250 µm (irregular)	Inverse	Inverse	Higher surface-to-volume ratio and more water being held in the interstitial volume between particles
Aam	50 to 500 µm	Direct	Inverse	Changes in cross-linked structure with particle size: smaller particles have a larger surface zone and smaller nucleus, resulting in lower absorption

2.11 Bacteria Enrichment Methods as an Application Area of SAPs

This section reviews various bacterial enrichment methods, discussing their advantages and limitations. The need for user-friendly and effective enrichment techniques is emphasized, as these methods are essential for enhancing detection sensitivity and accuracy. Bacterial concentration techniques can be categorized into conventional and portable enrichment methods.

2.11.1 Conventional Enrichment Methods

Filtration: Filtration is a simple and widely used method for bacterial enrichment. It involves passing water samples through filter membranes with pore sizes of 0.2 to 1.2 micrometers, which trap bacteria on the membrane's surface. The trapped bacteria can then be recovered for downstream analysis. While this method is cost-effective and applicable to large volumes, it requires specialized equipment, such as vacuum pumps, and can be time-consuming. Additionally, membrane clogging and low bacterial recovery efficiencies can pose challenges [113].

Centrifugation: In this technique, water samples are subjected to high-speed spinning to separate bacteria based on density. The bacteria sediment at the bottom of the tube, enabling their collection. Centrifugation is a rapid method suitable for small sample volumes, but it requires benchtop centrifuges and may not be portable for field applications [113].

Immunomagnetic Separation (IMS): This method uses magnetic beads coated with antibodies specific to target bacteria. After binding, a magnet separates the bacteria-bead complexes from the rest of the sample. IMS offers high specificity and can be automated, but it is limited by the high cost of antibodies and small sample volumes that can be processed [114].

2.11.2 Portable Enrichment Methods

SAPs can provide a promising approach for bacterial enrichment without the need for complex equipment or extensive training. SAPs can absorb large amounts of water, leaving bacteria behind, and concentrating bacterial cells in the remaining solution. This method is simple and cost-effective, enhancing bacterial detection sensitivity, especially in resource-limited settings. Integrating SAPs into portable detection devices can streamline on-site water quality assessment, leading to improved public health outcomes. Studies have demonstrated that SAPs like poly(acrylamide-co-itaconic acid) effectively concentrate *E. coli* from water samples, proving to be rapid, efficient, scalable, and cost-effective [7, 9, 10].

Recent advancements in the synthesis and application of SAPs have demonstrated their potential in concentrating biological contaminants in water samples.

In 2016, Xie et al. [7] synthesized 1 mm-sized poly(acrylamide-co-itaconic acid) beads to concentrate water samples containing *E. coli* for the first time. They employed a milli-fluidic system with a T-junction droplet generation method and used water as the monomer solution and silicon oil as the continuous phase. Figure 2-5a shows the schematic of the enrichment process used in Xie's study, where SAP beads were added to bacterial samples, allowed to swell, and then removed. The concentration efficiency was evaluated using *E. coli* as a model microorganism, with initial *E. coli* concentrations ranging from 10^2 to 10^4 CFU/mL. To maintain bead suspension, a

concentration factor of 1.3-2 was applied for each step, as higher factors (e.g., >4) significantly reduced efficiency due to trapping of microorganisms on the bead surface or within voids. The average recovery efficiency of 80% demonstrated the effectiveness of P(AM-co-IA) beads for bacterial enrichment [7].

In 2018, Jing et al. [115] used a similar concept to synthesize acrylic acid-acrylamide SAP beads with particle sizes of 300 μm, 500 μm, and 1000 μm. They investigated the effects of various parameters, including bead size, on swelling behavior and bacterial concentration performance. Figure 2-5a also illustrates the schematic and real images of Jing's process, where SAP beads of varying sizes were employed for enrichment. Smaller beads (300 μm) were used for bacterial enrichment in 10 mL samples, achieving a concentration degree of 10 over five cycles. This approach reduced processing times to 10 minutes per cycle while maintaining cumulative enrichment efficiencies of 95%, 85%, and 80% for initial *E. coli* concentrations of 3×10^2, 2×10^3, and 6×10^3 CFU/mL, respectively. Compared to Xie's method, Jing's study demonstrated the advantage of optimizing bead size to reduce the total enrichment time to 50 minutes [115].

In 2020, Wu et al. [9] tried to further enhance enrichment factors, reduce cycles, and minimize processing time. They synthesized 500 μm acrylamide-itaconic acid-based SAP beads using a droplet polymerization system. Figure 2-5b provides the schematic of Wu's enrichment process, which incorporated a 3D-printed system and a hand-press centrifuge to separate swollen SAPs from the concentrated solution. This method allowed the enrichment of *E. coli* in 40 mL samples with 10^4-10^6 CFU/mL initial concentrations, reducing residual water to 4 mL and achieving a 10-fold concentration factor with 80% efficiency in a single 10-minute cycle. However, reliance on external equipment, such as the centrifuge, limited its portability and practicality for on-site

applications [9].

In 2021, Yang et al. [10] developed a single-step, equipment-free method for concentrating extracellular vesicles (EVs) using SAP beads. Figure 2-5c illustrates the schematic and real images of Yang's enrichment process, where 200 mg/mL SAP beads were added to EV samples and incubated for 30 minutes. This method reduced the solution volume to 11% of the original, achieving a 9-fold concentration with a recovery yield of 78.9%. The equipment-free approach demonstrated the adaptability of SAP beads for biological sample enrichment, offering simplicity and high purity for downstream applications.

The summary of the findings from these papers is shown in Table 2-2.

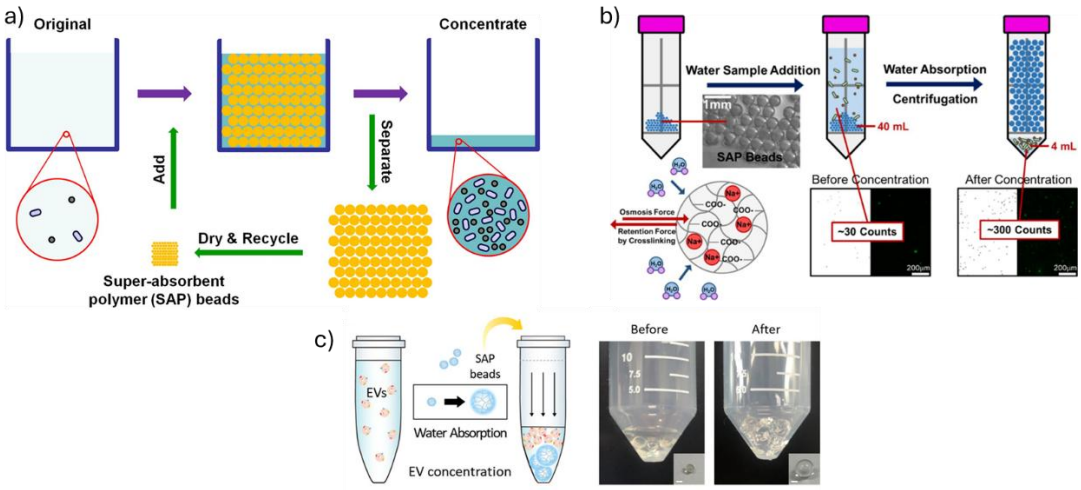

Figure 2-5. a) Schematic and real images of the *E. coli* enrichment process using SAP beads as demonstrated by Xie et al. and Jing et al., highlighting the similarities in polymer bead design and bacterial enrichment mechanisms. b) Wu et al.'s method combining SAP beads with a 3D-printed system and hand-press centrifuge for improved *E. coli* enrichment. c) Yang et al.'s single-step, equipment-free SAP bead-based enrichment process for extracellular vesicles Reprinted with permission from Elsevier [7, 10, 116].

Table 2-2. Comparative summary of studies on SAP-based bacterial enrichment in water analysis

SAP Type	Particle Size	Conc.[1] Factor	Required Time	External Equipment	Target Sample	Initial Volume	Conc. Efficiency	Number of Cycles	Ref
Aam-IA	1 mm	1.3-2	100 min	No	*E. coli*	10 mL	80%	5	[7]
AA-Aam	300 µm	3	50 min	No	*E. coli*	10 mL	80-95%	5	[115]
Aam-IA	500 µm	10	10 min	Hand-press centrifuge	*E. coli*	40 mL	80%	1	[9]
AA-Aam	3 mm	9	30 min	No	EVs[2]	20 mL	78%	1	[10]

2.12 Research Questions and Gaps

A review of the literature on SAP-MP characterization and their applications reveals contradictory findings regarding the relationship between particle size and swelling behavior, as well as gaps in their uses for biological sample enrichment. These inconsistencies in characterization methods underline the complexity of SAP behavior, particularly at the microscale. Accurate single-particle characterization methods are essential for understanding the swelling properties of SAP-MPs. To address these challenges, developing advanced microfluidic platforms for real-time, high-resolution single-particle analysis could reconcile these conflicting observations. (See Table 2-1 for details on swelling behavior findings.)

Additionally, while previous studies have introduced SAPs for biological sample enrichment, the efficiency and processing times of these methods remain suboptimal, limiting their practicality for real-world applications. (See Table 2-2 for comparative details on enrichment efficiencies and methods). The performance of SAPs in adsorption could be significantly enhanced by incorporating MXenes, a novel class of 2D materials with exceptional adsorption capabilities. This

[1] Concentration
[2] Extracellular Vesicles

innovation not only reduces potential waste but also promotes environmental sustainability by enhancing separation processes. MXene/AA composites, such as MXene/Sodium Alginate and MXene/AA, have demonstrated superior adsorption properties for organic dyes and represent sustainable solutions for water purification. However, their potential for bacterial sample enrichment remains largely unexplored, presenting an innovative direction for future research [7, 9, 10].

The analysis of previous studies on SAP-MP characterization and SAP-based biological sample enrichment reveals several critical research gaps and areas for further investigation:

1. **Swelling Behavior Characterization**: Traditional methods for analyzing SAP swelling behavior, such as gravimetric and tea bag methods, lack the precision needed to investigate the swelling dynamics in real time, especially for microparticles. These methods do not account for transient swelling stages or environmental effects, which are crucial for understanding SAP performance in complex matrices.
2. **Particle Size and Enrichment Efficiency**: Previous studies have explored various SAP particle sizes, ranging from millimeter-sized to 300 μm particles. However, the effect of particle size on the concentration factor and enrichment efficiency is not clear. While some studies suggest that smaller particle sizes reduce swelling time, they do not demonstrate a significant impact on the overall concentration factor. Further research is needed to systematically investigate the relationship between SAP particle size and bacterial enrichment efficiency, particularly at the microscale.
3. **Chemical Composition Optimization**: The chemical composition of SAPs, including the type and ratio of monomers and crosslinkers, significantly influences their swelling

behavior and bacterial enrichment efficiency. Although some studies have investigated these parameters, there remains a need for comprehensive optimization to enhance SAP performance for specific applications. Specifically, the impact of these chemical parameters on the enrichment factor and efficiency in various environmental conditions has not been fully explored.

4. **Use of External Equipment**: Several studies have utilized external equipment like hand-press centrifuges to separate SAPs from the sample, which limits the practicality and convenience of these methods for on-site applications. Developing SAP-based enrichment methods that do not require such equipment would greatly enhance their applicability in field conditions.

5. **Composite Material Development**: While the incorporation of nanostructures like MXene into hydrogels and SAPs has shown promise in enhancing their functional properties, the application of MXene/SAP-MPs for bacterial enrichment remains underexplored. There is an opportunity to investigate how these composite materials can improve the sensitivity and efficiency of bacterial detection methods in water analysis.

Addressing these gaps will involve the design and fabrication of advanced microfluidic platforms for SAP-MP characterization, comprehensive chemical composition optimization, development of portable enrichment methods, and rigorous testing across diverse scenarios. This research aims to contribute by developing MXene/SAP-MP nanocomposites and evaluating their performance in bacterial enrichment for water analysis. These efforts will bridge existing gaps and enhance the practical applications of SAP-based technologies in environmental and biological sample enrichment.

2.13 Research Objectives

The primary goal of this research is to advance the application and understanding of SAP-MPs in bacterial enrichment for water analysis. To achieve this overarching goal, the study is structured around the following specific objectives:

1. **Design and Fabricate a Microfluidic Platform for Single-Particle and Real-Time Characterization of SAPs**:
    - Develop a microfluidic platform for the real-time trapping and analysis of SAP-MPs' swelling behavior.
    - Enable single-particle characterization of SAP-MPs, allowing for quantitative analysis of their VSR, SR, and swelling model.
2. **Investigating the Effects of Key Parameters on SAP-MP Swelling Behavior**:
    - Examine the effects of particle size, crosslinker concentration (Cr), monomer concentration (AA), and neutralization degree (ND) on the swelling behavior of SAP-MPs.
    - Utilize the microfluidic platform to analyze the impact of these parameters individually and in combination, focusing on the structure-to-property relationships of SAP-MPs.
3. **Synthesize MXene Nanoparticles and Develop MXene/SAP-MP Nanocomposites**:
    - Synthesize MXene nanoparticles and incorporate them into SAP-MPs to develop MXene/SAP-MP nanocomposites.
    - Employ the breathing-in breathing-out (BI-BO) method to incorporate MXene, enhancing the nanocomposites' properties for environmental applications.
4. **Evaluate the Efficiency of MXene/SAP-MP Nanocomposites for Bacterial Enrichment**:

- Assess the effectiveness of MXene/SAP-MPs in concentrating bacteria to improve the sensitivity of detection methods.
- Provide a preliminary concentration step for water analysis, evaluating the application of MXene/SAP-MPs for bacterial enrichment in water samples.

By addressing these specific objectives, this research aims to provide a comprehensive understanding of the factors influencing SAP-MP performance in bacterial enrichment, develop advanced materials and methodologies for efficient water analysis, and contribute to the improvement of water quality monitoring and public health protection.

Chapter 3

Materials and Methods[1]

This section provides a detailed description of materials and methods used in this research. It includes materials for SAP-MPs synthesis, microfluidic device fabrication, MXene synthesis, and characterization, along with the methods for SAP-MPs synthesis, particle size analysis, and data processing.

[1] Portions of this chapter are adapted from the following works:

1. Tabesh, E., Leung, S. N., Rezai, P. (2023). "A microfluidic-based in-situ investigation of swelling dynamics of superabsorbent polymer microparticles". *Materials Today Communications*, 106369.
2. Tabesh, E., Zabihihesari, A. R., Rezai, P., & Leung, S. N. "In-situ investigation of swelling dynamics of acrylamide-acrylic acid superabsorbent microparticles at a single particle level". *Macromolecular Rapid Communications*, 2025.
3. Tabesh, E., Grumme, D., Herb, M., Rezai, P., Maleki, H., & Leung, S. N. "MXene/superabsorbent polymer composites for bacterial enrichment". Manuscript in preparation.

3.1 Materials

Table 3-1 lists the materials used in this research and their specific functions, categorized by purpose (SAP-MPs synthesis, device fabrication, MXene synthesis, and general use). All materials were used as received.

Table 3-1. Material, function, and vendor for SAP-MPs synthesis, device fabrication, and characterization.

Purpose	Material	Function	Vendor
SAP-MPs Synthesis	Acrylic Acid (AA)	Monomer	Sigma Aldrich
	Acrylamide (Aam)	Monomer	
	N,N′-methylene bisacrylamide (MBAm)	Crosslinker	
	Ammonium Persulfate (APS)	Initiator	
	Cyclohexane	Organic solution	
	Span 80	Surfactant	
	Sodium Hydroxide (NaOH)	Neutralization agent	
Microfluidic Device Fabrication	Polydimethylsiloxane (PDMS) SYLGARD™ 184 Silicone Elastomer	Device	Dow Corning Co.
	Isopropyl Alcohol (IPA)	Washing agent	Sigma Aldrich
MXene Synthesis	titanium aluminum carbide (Ti_3AlC_2)	Precursor	
	hydrochloric acid (HCl)	Etching agent	
	lithium fluoride (LiF)	Etching agent	
General purposes	Ethanol	Carrier fluid	
	DI water	Test fluid	-
Enrichment Characterization	*Escherichia coli* (strain K12, DH5α)	Target bacteria	York University

Figure 3-1 shows the molecular structure of chemicals used in the thesis.

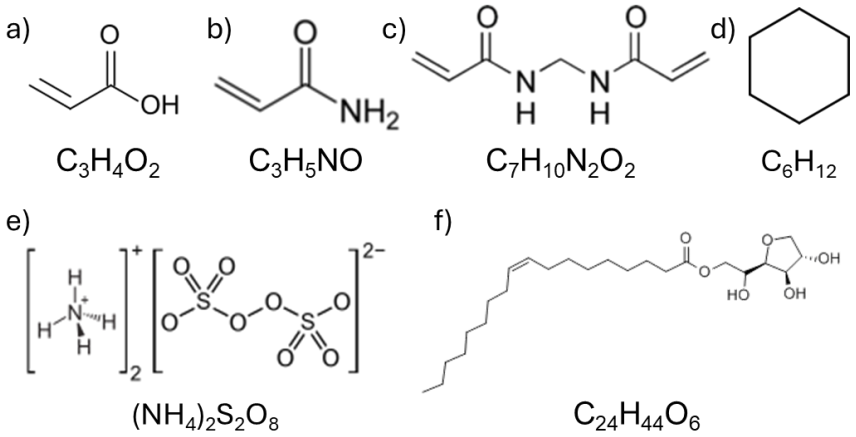

Figure 3-1. Molecular structure of key materials: a) acrylic acid, b) acrylamide, c) N,N′-methylene bisacrylamide (MBAm), d) cyclohexane, e) Ammonium Persulfate (APS), and f) Span 80.

3.2 Synthesis of SAPs

SAP-MPs were synthesized using the inverse suspension polymerization technique, varying the crosslinker ratio (Cr), acrylic acid ratio (AA), neutralization degree (ND), and particle sizes. The synthesis involved the preparation of a continuous phase and a dispersed phase, described in detail below.

3.2.1 **Preparation of Dispersed Phase**

To prepare the dispersed phase, acrylic acid (AA) was neutralized by adding the required amount of 8 M NaOH solution while mixing in an ice bath to prevent temperature rise and AA precipitation. The neutralization reaction follows the chemical equation:

$$CH_2{=}CHCOOH{+}NaOH{\rightarrow}CH_2{=}CHCOONa{+}H_2O \quad (3\text{-}1)$$

The ND was determined using the following equation:

$$ND = {}^{n_a}/_{n_b} \quad (3\text{-}2)$$

where n_a and n_b are the molar amounts of NaOH and AA, respectively. The ND was set from 0 to

100%.

The aqueous phase was prepared by dissolving a total of 1.2 g of monomers (AA and AAm) in predetermined amounts to achieve different AA percentage, indicated as AA in 4 mL of deionized (DI) water. For instance, for a sample with 10% AA, 1.08 g of AAm and 0.12 g of AA were used. The crosslinker was then added to achieve the desired Cr. Subsequently, 6.6 mg of ammonium persulfate (APS) was introduced as the initiator, maintaining a constant concentration across all experiments. This solution was mixed and purged with nitrogen gas for 20 minutes at 25 °C.

3.2.2 **Preparation of Continuous Phase**

The continuous phase was prepared by adding 16 mL of cyclohexane to a three-neck flask equipped with a condenser, a dropping funnel, and a nitrogen purge line. Then, 0.5 g of Span80 was added and mixed using a magnetic stirrer at 300 rpm for 20 minutes.

3.2.3 **Polymerization Process**

The prepared aqueous phase was added dropwise to the three-neck flask using a dropping funnel, while stirring continuously at 300 rpm. The mixture was purged with nitrogen gas and homogenized for 15 minutes. Polymerization was initiated thermally by immersing the reaction vessel in a 70 °C water bath for 3 hours. After the reaction, 100 mL of ethanol was added to the reaction vessel to precipitate the final SAP-MPs.

The SAP-MPs were washed twice with ethanol to remove any unreacted materials. The washed particles were separated through filteration using filter paper and dried overnight at room temperature.

3.2.4 **Particle Size Separation and Analysis**

In the final step, the dried SAP-MPs were separated into four size ranges: 70-105 μm, 120-150

μm, 180-200 μm, and 250-300 μm using sieves No. 200 to No. 50 (McMaster-Carr, USA). The average particle sizes for each group was determined using an optical microscope and analyzed with customized image analysis code in MATLAB. The measured average particle sizes for each group were 89.51 ± 9.13 μm, 137.8 ± 8.21 μm, 194.3 ± 6.38 μm, and 270.8 ± 11.39 μm, respectively. For simplicity, these particle size ranges are denoted as 90, 140, 200, and 270 μm in all subsequent tables and figures.

3.3 Design of Experiment

Response Surface Methodology (RSM) was used as the principal approach to optimize the water absorption performance of SAP-MPs. In this context, the effects of the Cr, AA, ND, and particle size on three critical response variables, VSR_{eq}, SR, and CT, were investigated. Table 3-2 summarizes the varying levels of different factors considered in the experimental study. Utilizing RSM, experiments were conducted using a central composite design (CCD) with one center point, enabling exploration of linear, quadratic, and interaction effects of various independent variables on the response parameters. The independent variables considered in this study include a range of values: Cr from 0.25% to 2.0%, AA from 10% to 90%, ND from 50% to 100%, and particle size from 90 to 270 μm. This systematic investigation aims to elucidate the relationships among particle size and these factors, and to facilitate the optimization of the desired outcomes in RSM.

Table 3-2. Summary of the varying levels of Cr, AA, ND, and particle size used in the experiments, as per the Response Surface Methodology (RSM) design of experiment approach.

No.	Cr (%)	AA (%)	ND (%)	Size (μm)	No.	Cr (%)	AA (%)	ND (%)	Size (μm)
1	0.25	0.5	0.75	90	**15**	1.13	0.1	0.75	200
2	0.25	0.5	0.75	140	**16**	1.13	0.1	0.75	270
3	0.25	0.5	0.75	200	**17**	1.13	0.9	0.75	90
4	0.25	0.5	0.75	270	**18**	1.13	0.9	0.75	140
5	1.13	0.5	0.75	90	**19**	1.13	0.9	0.75	200
6	1.13	0.5	0.75	140	**20**	1.13	0.9	0.75	270
7	1.13	0.5	0.75	200	**21**	1.13	0.5	0.5	90

8	1.13	0.5	0.75	270	**22**	1.13	0.5	0.5	140
9	2	0.5	0.75	90	**23**	1.13	0.5	0.5	200
10	2	0.5	0.75	140	**24**	1.13	0.5	0.5	270
11	2	0.5	0.75	200	**25**	1.13	0.5	1	90
12	2	0.5	0.75	270	**26**	1.13	0.5	1	140
13	1.13	0.1	0.75	90	**27**	1.13	0.5	1	200
14	1.13	0.1	0.75	140	**28**	1.13	0.5	1	270

3.4 Microfluidic Device Design and Fabrication

Figure 3-2 shows a schematic of the device fabrication process. A soft lithography technique was used to fabricate the device. It was made of three PDMS layers that were plasma-bonded together. For all layers, the PDMS base and curing agent were mixed in a standard ratio of 10:1 and degassed in a vacuum chamber for 20 minutes before pouring into molds and curing at 60˚C for 1 hours.

The middle layer was fabricated as a double-sided PDMS layer by replica molding using a pair of 3D-printed molds [117]. It consisted of two main features, i.e., SAP-MPs trapping areas (TRAs) and associated main channels on the trap mold, as well as swelling chambers (SWCs) and associated guide channels on the chamber mold (Figure 3-2a). The molds were printed using an Objet260 Connex3 printer (Stratasys Ltd., USA). After printing, a UV and thermal post-treatment process was performed to remove unreacted monomers and photo-initiator from the surface of the molds, ensuring the structural stability and chemical inertness of the molds [118]. The printed mold parts were washed with ethanol and post-cured in a 405 nm LED UV box for 10 min at a rate of 14 W/cm^2. Then, the mold parts were ultrasonically treated with isopropanol alcohol (IPA) for two hours and exposed to 80 °C in an oven for 24 h.

The SAP-MP TRAs on the trap mold had to be precisely aligned with the SWCs on the chamber mold (Figure 3-2b). A sufficient overlapping between each trap and chamber was needed not only to keep chambers centered on traps but also to allow the PDMS to fill the traps (see inset image in

Figure 3-2b). As shown in Figure 3-2b, eight integrated alignment marks would align with the TRAs and SWCs when the mold parts were assembled. To prepare the middle layer, the PDMS prepolymer was poured into the assembled 3D-printed molds, cured, and peeled off from the mold (Figure 3-2c). PDMS prepolymer was cast on two glass slides using aluminum foils and cured for the top and bottom device layers. The thicknesses of the top and bottom layers were about 5 mm.

For plasma bonding, oxygen plasma (PDC-001-HP, Harrick Plasma, USA) was used at 870 mTorr and 30 W for 30 s. First, the top layer was punched to make five inlets and one outlet. The middle PDMS layer was then plasma bonded to the top layer after curing. Then, the assembled parts were plasma bonded to the bottom layer so that the main middle layer was sandwiched between the top and bottom layers (Figure 3-2d and e).

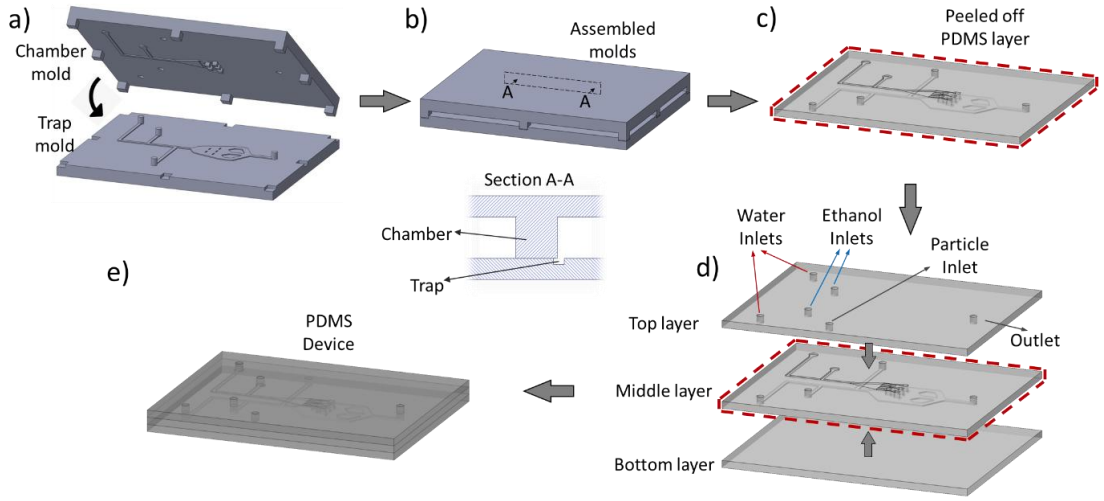

Figure 3-2. The microfluidic device fabrication using 3D-printed master molds followed by a bonding process. (a) two parts of molds before assembling, (b) assembled molds. The inset image shows the A-A cross-section in which the chamber (SWC) and trap (TRA) features are aligned, (c) peeled off middle PDMS layer fabricated in the assembled molds, (d) exploded device layers consisting of the middle layer and two flat top and bottom layers, and (e) the final 3-layer PDMS device for SAP-MP investigations. Reprinted with permission from Elsevier [14].

Figure 3-3a shows an actual image of the microfluidic device developed for trapping and imaging

SAP-MPs under a microscope. Trapping and imaging happened within the region of interest shown by a red dashed box in Figure 3-3a-I. This region is shown in Figure 3-3a-II and illustrated schematically in Figure 3-3b. In this diagram, the solid lines represent the five TRAs arranged in the main channels, while the dashed lines represent the SWCs and guide channels. The trapping mechanism was based on the improved hydrodynamic cells and plastic microparticles trapping method [119]. SAP-MPs were loaded into the device through the main channel and hydrodynamically trapped inside the TRAs arranged in two rows to fit in the microscope's field of view (Figure 3-3b). The second row of TRAs (S1-S3) was offset from the first row (F1-F2) to ensure that the second row could capture SAP-MPs that were not trapped by the first row. Figure 3-3c shows a side cross-section view of one TRA and SWC during the trapping and swelling processes. A downward flow from the guide channel pushed the SAP-MP into the TRA, preventing its escape. SAP-MPs were loaded using ethanol as a carrier solution. After the trapping process (Figure 3-3c-I), SAP-MPs were exposed to water, and their swelling behavior (Figure 3-3c-II) was video recorded under a microscope. To switch the solution between ethanol and water, the device has two inlets for ethanol and two inlets for water. One of each is connected to the main channel, and the other is connected to the guide channel, allowing all the solution inside the channels and SWCs to be washed away when the solution is switched.

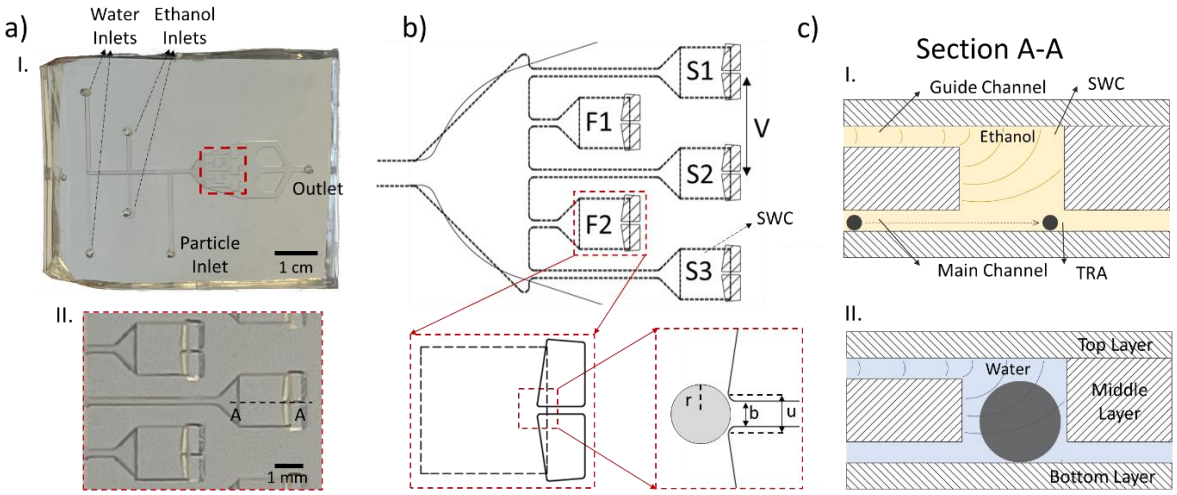

Figure 3-3. The microfluidic device developed for parallel trapping of 5 SAP-MPs. (a) an actual image of the device (I) with the red dashed lined region of interest shown in (II). (b) the TRAs (F1-F2, S1-S3) and close-up images of an individual trap and an SAP-MP. (c) cross-section view of line A-A, in (a-II), drawn across a TRA/SWC for SAP-MP (I) trapping and (II) swelling studies. Yellow and blue colors represent ethanol and water, respectively. Reprinted with permission from Elsevier [14].

The large magnitude of SAP-MPs swelling represents a challenge to design the device. If the SWC is designed based on the initial particle size, swelling will clog the channel. If the SWC is designed based on the size of the swelled particles, trapping the initial unswelled SAP-MPs will be impossible. The device was designed with different heights for TRA and SWC regions to overcome this challenge. The height of the main channel and the TRA were designed based on the initial size of the SAP-MPs. The height of the SWC was designed to provide enough space for the trapped SAP-MPs to swell. Based on the existing data for AA-Aam-based SAPs, it was assumed that the SAP-MPs would have a maximum volumetric swelling ratio of 1000 [120].

The TRAs in our device were designed based on the hydrodynamic trapping principles reported by Xu et al. [119] The design parameters included the SAP-MP radius (r), channel height (h), distance between SAP-MPs in the same row (v), and the upper and lower widths of the trap opening (u and b, respectively) (Figure 3-3b). The TRA geometry had to meet several criteria,

including single-particle trapping, high particle packing density, prevention of channel clogging, and feasibility of fabrication. To ensure that particles were trapped individually, the channel height had to be smaller than the diameter of two SAP-MPs (4r) while being larger than the diameter of one SAP-MP (2r). Thus, the criteria for channel height were $2r<h<4r$. Additionally, to ensure that a single SAP-MP was trapped within a TRA, b and u had to be smaller than the diameters of one SAP-MP and two SAP-MPs, respectively ($b<2r$ and $u<4r$). The SWCs in our device were square-shaped with a width of 2 mm, and the distance between adjacent TRAs had to be greater than the SWC size ($v>2$ mm) to ensure that the fabrication process was feasible. The dimensions of the TRAs were optimized based on an SAP-MP radius of $r=125$ μm, with h fixed at 350 μm. Consequently, the other parameters were found based on criteria listed in Table 3-3. The TRAs' pillars were designed in a trapezius shape for two reasons. First, to allow PDMS to fill the pillars' part of the master mold after assembly during the fabrication process. Second, to guide particles toward the centerlines of adjacent TRAs in the second row. As a result, if one TRA is already filled with a particle, the second particle must bypass the filled trap and align with another TRA in the second row.

For SAP-MPs larger than 120 μm, both chamber and trap master molds were 3D printed using an Objet260 Connex3 printer. For SAP-MPs smaller than 120 μm, which required higher resolution to fabricate SAP-MP trapping regions (TRAs), standard photolithography on a silicon wafer was used to fabricate the trap mold, according to the methodology outlined by Xia et al. [121]. All device designs were crafted using SolidWorks.

The dimensions of critical parameters, such as the SAP-MPs radius (r), the channel height (h), the distance between adjacent SAP-MPs (v), and the upper and lower widths of the trap opening (u

and b, respectively), were optimized based on the methodological criteria established in the published work [14]. The specific values and details of these optimized parameters are summarized in Table 3-3.

Table 3-3. Microfluidic device main geometries based on SAP-MPs with different initial sizes.

Parameter	r	h	b	u	v	target particle size
Value (μm)	45	120	30	50	1500	70-100
	70	180	50	100	1500	120-150
	100	250	80	150	2000	180-212
	135	350	120	200	2000	250-300

3.5 Device Characterization

Before using the designed microfluidic device to characterize the swelling behavior of the SAP-MPs, the device was carefully analyzed to ensure uniformity among traps and to confirm that any differences in their position do not affect the swelling behavior of SAP-MPs. To achieve this, several steps were taken. Firstly, the loading time required for trapping the particles was evaluated. Subsequently, ethanol and water were utilized to characterize the fluid exchange time for each trap. The following sections provide detailed methods for each aspect of this characterization process.

3.5.1 Trapping Time Characterization

Since SAP-MPs do not swell in ethanol, it was used as a carrier fluid to load them into the device. A syringe was used to manually insert suspensions of SAP-MPs into the particle inlet (Figure 3-2d). Different flow rates of 0.03, 0.15, and 0.3 mL/min of the suspension in the ethanol inlets (Figure 3-2d) were used during the loading process.

Trapping time per SAP-MP was evaluated by measuring the trapping time of the particles at three different flow rates. Since it was difficult to fill all the traps at a flow rate of 0.3 mL/min, the time to 80% of the traps filled with SAP-MPs (i.e., four out of five TRAs) was compared to the loading time of the device at all flow rates. The trapping time per SAP-MP at each flow rate was reported

as an average using Eq.(3-3):

$$\text{Trapping time per particle} = {}^{\text{Required time for filling 4 TRAs}}/_{4} \quad (3\text{-}3)$$

3.5.2 Fluid Exchange Characterization

To characterize the device and the differences between traps, two key parameters, transition time (T_t) and time difference (T_d), were defined. T_t represents the time required for the fluid in a TRA to transition from ethanol to water, while T_d denotes the difference between the maximum and minimum T_t values observed across different traps (F1-F2 and S1-S3 in Figure 3-3b) at a specific flow rate ($T_{t\,max} - T_{t\,min}$).

During experimentation, ethanol was introduced into the device, colored with yellow food coloring, followed by the introduction of water colored with blue food coloring. The transition time (T_t) was quantified as the duration required for the color in the chamber to transition completely from yellow to blue, indicating the exchange of fluids from ethanol to water.

To calculate T_t, video analysis was performed. The region of interest (ROI) was selected in the video, and the color intensity was analyzed frame by frame to determine the time required for the color transition. Specifically, the following method was employed:

- The starting hue range was defined as the average hue value of the selected ROI in the first frame, representing the yellow phase (ethanol).
- The target hue range was defined as the average hue value of the selected ROI in the last frame, representing the blue phase (water).
- The T_t was determined as the duration from when the average hue of the ROI exits the starting hue range to when it stabilizes within the target hue range for a duration of at least one second.

The transition time (T_t) was calculated using the formula:

$$T_t = T_{blue} - T_{yellow} \quad (3\text{-}4)$$

where the T_{blue} is the time when the average hue stabilizes within the target hue range for at least one second and T_{yellow} is the time when the average hue exits the starting hue range.

The T_d was calculated as the difference between the maximum and minimum transition times observed among all traps, as follows:

$$T_d = T_{t_{max}} - T_{t_{min}} \quad (3\text{-}5)$$

where $T_{t_{max}}$ and $T_{t_{min}}$ are the maximum and minimum transition times observed across different traps, respectively.

3.6 SAP-MP Characterization

3.6.1 Physicochemical Characterization

The chemical structures and functional group compositions of the synthesized SAP-MPs were analyzed using Fourier Transform Infrared (FTIR) Spectroscopy (VERTEX 70v, Bruker Optics, Ettlingen, Germany). FTIR spectra were obtained in transmittance mode, averaging 64 scans per analysis with a resolution of 4 cm^{-1} in the mid-infrared region (4000–400 cm^{-1}). A comparison of FTIR spectra from raw monomers and synthesized SAP-MPs confirmed successful polymerization and identified the functional groups present.

Thermal properties of SAP-MPs were evaluated using a thermogravimetric analyzer (TGA55 Discovery, TA Instruments, New Castle, DE, USA). Samples, weighing in a range of 10-20 mg, were analyzed under a nitrogen flow rate of 60 mL/min, with the temperature increasing from 30°C to 800°C at a heating rate of 10°C/min. This analysis provided insights into the thermal stability and degradation behavior of the SAP-MPs.

The morphological properties of SAP-MPs were examined using scanning electron microscopy (SEM) (Quanta 3D FEG, Thermo Fisher, Hillsboro, OR, USA). Swelled SAP-MPs were frozen in liquid nitrogen and lyophilized using a freeze-drying system (Harvest Right, Salt Lake City, UT, USA) to preserve their structure. Before imaging, samples were sputter-coated with a 2 nm thick gold layer using a Denton Desk V sputter coater (Moorestown, NJ, USA). SEM images highlighted the morphology and uniformity of the synthesized particles.

3.6.2 Swelling Behavior Characterization

The swelling behavior of SAP-MPs was characterized through a detailed analysis of a video recording the in-situ swelling experiments based on the aforementioned microfluidic platform. During the first minute, where swelling was most rapid, frames were sampled at 2 Hz. Beyond this point, the sampling rate was reduced to 0.1 Hz as the swelling rate stabilized.

A MATLAB-based analysis was employed to measure the diameters (d_t) of SAP-MPs at various time intervals, normalized to their initial diameters (d_0). The volumetric swelling ratio (VSR_t) was calculated using the formula:

$$VSR_t = \frac{V_t - V_o}{V_0} = \left(\frac{d_t}{d_0}\right)^3 - 1 \tag{3-6}$$

where V_0 and V_t represent the initial and time-dependent volumes of the SAP-MPs, respectively.

The VSR_{eq} was determined as the steady-state volume reached by the SAP-MPs, defined at the moment where the change in volume between three consecutive measurements was less than 1%. The SR was calculated using:

$$SR = {VSR_\tau}/{\tau} \tag{3-7}$$

where VSR_τ corresponds to the swelling at the characteristic time τ, the time required to reach 63% of the equilibrium swelling value. This rate parameter is based on a Voigt-like model for SAP swelling [122, 123].

3.6.3 Swelling Kinetics Models

Two kinetic models, pseudo-first-order (PFO) and pseudo-second-order (PSO), were applied to validate the experimental results obtained for the swelling behavior of SAP-MPs [124]. The accuracy of each model was evaluated based on the coefficient of determination (R^2), with the model exhibiting the highest R^2 value considered the best fit.

According to the PFO kinetic model, the SR at any given time is directly proportional to the remaining unabsorbed water content as the SAP-MPs approach equilibrium (VSReq). This model assumes that the swelling kinetics follow first-order behavior, meaning the SR decreases as the SAP-MPs approach equilibrium, without making specific assumptions about the mechanism [124]. The swelling can be expressed by the following differential equation:

$$\frac{dVSR_t}{dt} = k_1(VSR_{eq} - VSR_t) \tag{3-8}$$

The integrated form of this equation is:

$$VSR_t = VSR_{eq}(1 - e^{-k_1 t}) \tag{3-9}$$

where VSR_{eq} represents the equilibrium volume, VSR_t denotes the volume at time t, and k_1 (1/min) is the PFO rate constant.

In contrast, the PSO kinetic model assumes that the SR at any given time is proportional to the

square of the remaining water content that the SAP-MPs have yet to absorb before reaching equilibrium (VSReq). This model describes second-order kinetic behavior, which could reflect more complex interactions between the polymer network and the absorbed water, such as polymer relaxation and water-polymer interactions. As a result, the SR decreases more significantly as the SAP-MPs approaches its equilibrium swelling capacity [124]. The PSO kinetic model can be expressed as:

$$\frac{dVSR_t}{dt} = k_2(VSR_{eq} - VSR_t)^2 \tag{3-10}$$

Integrating with the initial condition $VSR_0 = 0$ leads to:

$$VSR_t = \frac{k_2.t.VSR_{eq}^2}{1+k_2.t.VSR_{eq}} \tag{3-11}$$

where k_2 (1/min) is the PSO rate constant.

3.7 Experimental setup and procedure

Figure 3-4 illustrates the experiment setup for device and SAP-MPs characterization, which consisted of the microfluidic device, an inverted optical microscope (BIM-500FLD, Bioimager Inc., Canada), a cell phone camera (30 fps, iPhone 11 pro), a computer for video analysis and data collection, and two syringe pumps (LEGATO 111 and 110, KD Scientific Inc., USA).

In the experimental procedure, ethanol was introduced into the device through designated inlets at a flowrate of 1 mL/min. SAP-MPs suspended in ethanol were manually loaded into the device through a separate inlet called the particle inlet. When the SAP-MPs were trapped in the TRAs, the ethanol flow was stopped. Consequently, water at different flowrates was introduced into the channels through the two water inlets, thereby completely filling SWCs and initiating the swelling

process. Simultaneously, the real-time swelling behaviors of the trapped SAP-MPs were video recorded for 5 minutes under the microscope. These videos were then analyzed using MATLAB [14]. All experiments were carried out at room temperature.

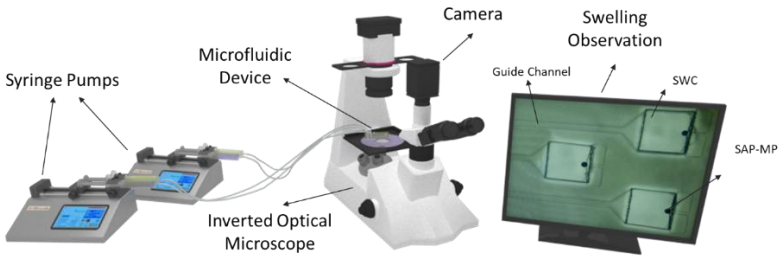

Figure 3-4. Experimental setup for swelling investigation of SAP-MPs. It consists of the microfluidic device on a microscope equipped with a camera (cellphone), two syringe pumps for exposing SAP-MPs to ethanol and water for trapping and swelling processes, respectively, and a computer (not shown) for video collection and analysis. Reprinted with permission from Elsevier [14].

3.8 Synthesis of MXene

The synthesis of $Ti_3C_2T_x$ nanosheets was conducted through a selective etching method from the Ti_3AlC_2 precursor [93]. Initially, 1 g of LiF was gradually added to 20 mL of 9 M HCl and stirred for 30 minutes. Subsequently, 1 g of MAX phase powder (Ti_3AlC_2) was slowly introduced into the etching solution, allowing the Al layer to be etched at 35 °C over a period of 24 hours. During this period, the aluminum (Al) layer in the Ti_3AlC_2 precursor was selectively etched, resulting in the formation of $Ti_3C_2T_x$ nanosheets.

Following the etching process, the acidic supernatant was removed through repeated washing with deionized water and undergoing centrifugation at 9000 rpm until a stable dark green supernatant of $Ti_3C_2T_x$ with a pH of approximately 6 was obtained [93]. For simplicity, $Ti_3C_2T_x$ will be referred to as MXene in the remainder of this study.

3.9 Synthesis of MXene/SAP nanocomposite

The MXene nanosheets were incorporated into the SAPs via the breathing-in-breathing-out

process (BI-BO). In this process, 50 mg of SAPs were immersed in 10 mL of MXene solution (10 mg/mL) for 10 minutes. These concentrations were carefully chosen to optimize the interaction between MXene and SAPs, minimizing MXene agglomeration and ensuring the SAPs remained submerged without complete absorption.

After immersion, the SAPs were washed using a 40-µm cell strainer with deionized (DI) water to remove any surface-bound MXene. They were then soaked in ethanol for an additional 10 minutes to induce deswelling and facilitate water desorption. This cycle of immersion in MXene solution and deswelling in ethanol was repeated several times to achieve the desired MXene concentration within the SAPs.

Following the BI-BO process, the SAPs underwent a final 20-minute immersion in DI water followed by a 20-minute soak in ethanol to complete the washing procedure. The washed SAPs were then placed on filter paper to remove excess surface moisture before being dried in an oven at 60 °C for 24 hours, yielding the final MXene/SAP nanocomposite microparticles.

3.10 MXene/SAP Nanocomposite Characterization

The physical and chemical properties of the synthesized MXene and MXene/SAP nanocomposite microparticles were characterized using SEM, XRD, FTIR, and TGA.

SEM analysis, performed using the Quanta 3D FEG system, examined the morphology of MXene nanosheets, as well as their integration within the SAP matrix. For this purpose, lyophilized samples of swelled MXene/SAP nanocomposites were sputter-coated with a 2 nm thick gold layer before imaging.

XRD was utilized to confirm the successful etching of the MAX phase into MXene nanosheets and to verify the incorporation of MXene within the SAPs. The analysis also revealed structural

changes that occurred during the synthesis of MXene.

FTIR spectroscopy identified the functional groups and chemical bonds within the MXene/SAP nanocomposite. The spectra were compared to those of the individual SAPs and MXene to highlight any potential interaction between the MXene nanosheets and the polymer matrix.

Thermal stability and degradation behavior were evaluated using the TGA55 Discovery system. Consistent with previous analyses, 10-20 mg samples were analyzed under a nitrogen flow rate of 60 mL/min, with the temperature increasing from 30°C to 800°C at a heating rate of 10°C/min. The results were compared to those of the pure SAPs and MXene to assess any modifications in thermal properties due to the incorporation of MXene in the SAPs.

The swelling behavior of MXene/SAP nanocomposite microparticles was characterized using the same methodology described in Section 3.7. The VSR and SR were analyzed to evaluate the influence of MXene incorporation on the swelling kinetics. The integration of MXene was expected to impact polymer-solvent interactions, potentially altering the swelling performance and mechanical properties of the nanocomposite.

3.11 Bacteria Enrichment

The bacteria enrichment test was conducted using water samples containing *E. coli* (strain K12, DH5α). The colony counting method was employed to assess bacterial viability post-enrichment,. *E. coli* was harvested during the mid-log growth phase. To simulate conditions in water, the bacteria were harvested by centrifugation at 4200 rpm for 5 minutes and washed three times with DI water. After the final wash, the bacterial suspensions were transferred into 15 mL commercial centrifuge tubes, and DI water was added to each tube to reach a total volume of 10 mL, adjusting the bacterial concentration to the predetermined level (e.g., 10^7 colony-forming units per mL

(CFU/mL)).

To each solution, 10 mg/mL of different SAPs were added, and the mixture was allowed to stand for 10 minutes to allow the SAPs to swell. Subsequently, the swelled SAPs were removed from the solution using filters, and the remaining solution volume was measured.

To ensure the reliability and accuracy of the bacterial enrichment process, multiple control experiments were conducted to assess bacterial viability and material effects under various conditions. First, *E. coli* suspensions were left untreated for 10 minutes in LB solution to evaluate bacterial viability under optimal growth conditions, serving as a baseline for comparison. Next, post-washing and centrifugation viability controls were performed by leaving washed and centrifuged *E. coli* suspensions untreated in DI water for 10 minutes to assess whether the preparatory steps impacted bacterial viability. Additionally, post-enrichment SAP culture controls involved culturing SAPs on agar plates after enrichment experiments to determine if bacteria adhered to their surfaces.

To evaluate the sterility of the SAPs and the enrichment process, sterility controls were conducted by exposing SAPs to sterile DI water under the same experimental conditions as enrichment tests, followed by plating both the solution and SAPs on agar to confirm the absence of contamination. Separate controls were designed to investigate the effects of the materials on bacterial viability: SAPs were added to bacterial solutions to determine if the SAPs influenced bacterial viability, and a similar test was conducted with MXenes added to bacterial solutions to examine their individual effects. Finally, the combined material effects were assessed by exposing bacterial solutions to SAP-MXene nanocomposite microparticles, measuring any changes in bacterial concentration.

To determine the effects of the enrichment process, 100 μL from each bacterial solution was

manually plated on agar plates. After overnight incubation at 37 °C, the number of bacterial colonies was manually counted, allowing for the calculation of the concentration of viable bacteria in CFU/mL. Serial dilutions were performed as needed for accurate quantification. Additionally, representative images of each condition and the subsequent bacterial growth on blood agar plates were captured using a digital camera for further analysis and documentation.

3.11.1 Enrichment Factor

To quantify the efficiency of the enrichment process, the enrichment factor (EF) was calculated by measuring the concentration of bacteria after the process and normalizing it by the initial concentration of bacteria. The mathematical formula is presented in the equation below:

$$EF = {}^{C_1}/_{C_0} \tag{3-12}$$

where C_0 and C_1 are the concentrations of bacteria in the aqueous samples before and after the enrichment process, respectively.

3.11.2 Concentration Degree

Concentration degree (CD) was defined as the ratio of the sample volumes before and after concentration using equation below:

$$\text{CD} = {}^{V_0}/_{V_1} \tag{3-13}$$

where V_0 and V_1 are the volume of the solution before and after the enrichment process, respectively.

3.11.3 Recovery Efficiency

Additionally, recovery efficiency (RE) represents the ratio of viable bacteria after versus before

the enrichment process and is expressed in Equation (3-13):

$$RE = \left(\frac{N_1}{N_0}\right) \times 100 = \left(\frac{V_1 \times C_1}{V_0 \times C_0}\right) \times 100 \quad (3\text{-}14)$$

where N_0 and N_1 are the number of bacteria in aqueous samples before and after the enrichment process, respectively. By substituting the definitions of the EF and CD:

$$RE = (EF/CD) \times 100 \quad (3\text{-}15)$$

3.12 Data Analysis and Statistics

All measurements were conducted with a minimum of three replicates, and the results are presented as mean ± standard deviation. Statistical analyses were performed using GraphPad Prism software (version 9.5.1). Analysis of Variance (ANOVA) was employed to compare the values among different groups due to its efficacy in assessing variations within and between groups. The significance of the findings was determined using p-values, with a significance threshold set at 0.05. In graphical representations of the data, statistical significance was indicated by asterisks: '*' denoted $p < 0.05$, '**' denoted $p < 0.01$, '***' denoted $p < 0.001$, '****' denoted $p < 0.0001$, and 'ns' indicated non-significant differences.

Given the device's reusability, fabrication of multiple devices was unnecessary; however, operator and experimental setup errors remained inevitable in the studies. Sample size analysis determined that N=8 measurements were needed for particle diameter measurement at each SAP chemical composition (unless otherwise mentioned), based on an upper threshold of 0.05 and a significance level of 80%.

Chapter 4

Microfluidic platform for characterization of SAP-MPs[1]

4.1 Introduction

This chapter focuses on the results from the first objective of this research: the design and fabrication of a microfluidic platform for trapping and analyzing the swelling behavior of SAP-MPs. The aim is to enable single-particle characterization of SAP-MPs in real time during the swelling process. This platform allows for the quantitative characterization of the VSR and SR of AA-Aam-based SAP-MPs under various environmental conditions, addressing existing

[1] Parts of this chapter are extracted from: Tabesh, E., Leung, S. N., & Rezai, P. (2023). "A microfluidic-based in-situ investigation of swelling dynamics of superabsorbent polymer microparticles". *Materials Today Communications*, 2023: p. 106369.

discrepancies in the literature regarding their swelling behavior. To our knowledge, no similar device had been designed or fabricated prior to this research.

To achieve this objective, a microfluidic platform for trapping AA-Aam-based SAP-MPs and investigating their in-situ swelling behavior was designed and fabricated. Following the fabrication of the device, it was characterized using ethanol and water to optimize its operational parameters. Upon validation of the device's capability, AA-Aam-based SAP-MPs were examined and compared with similar macroparticles reported in the literature. The influence of ND on the swelling behavior of AA-Aam SAP-MPs was also assessed.

This novel methodology enables the real-time investigation of the early-stage swelling behavior of SAP-MPs and can be used to characterize various SAP-MPs, as well as to study the effects of numerous processing and material parameters on their swelling performance across different applications.

4.2 Results and Discussion

Before loading the SAP-MPs into the microfluidic device, the fluid exchange time between ethanol and water in the SWCs and TRAs was analyzed. Then, the SAP-MP trapping efficiency of the device was investigated and optimized. Consequently, the swelling behavior of AA-Aam SAP-MPs and the effect of the ND on it was examined to validate the device's performance.

4.2.1 Fluid Exchange Characterization of the Microfluidic Device

To characterize the fluid exchange time between the TRAs, the transition time (T_t) between ethanol and water for each TRA in the microfluidic device was measured. The device was initially loaded with ethanol, and then water was introduced at flow rates ranging from 3 to 10 mL/min. The T_t values for each TRA were determined as shown in Figure 4-1a. As expected, T_t decreased

significantly in each TRA with increasing water flow rates. For example, at a flow rate of 3 mL/min, the maximum T_t was 34 seconds for trap S_1, which decreased to 11 seconds and 8 seconds at 5 and 10 mL/min, respectively, for the same TRA.

Additionally, at a constant flow rate, the T_t values for F_1, F_2, and S_2 traps, which are positioned in the middle of the channel, were not significantly different from each other. Due to the device's symmetry, the T_t values for traps S_1 and S_3 were also similar to each other but significantly different from those for traps F_1, F_2, and S_2. This discrepancy could be attributed to the parabolic velocity profile of the flow within the channel, where the center region experiences a higher velocity and the fluid near the channel walls experiences a lower velocity. Consequently, the middle TRAs filled with water faster than the side TRAs.

According to Figure 4-1b, the averaged T_t for the first and second row TRAs at the lowest flow rate of 3 mL/min was 18 s and 29 s, respectively. The average T_t reduced with increasing flow rate until there was no statistical difference between the first and second row TRAs at 10 mL/min. This decrease in the average time difference, T_d, is summarized in Figure 4-1c. It can be observed that T_d decreased from 17 s at 3 mL/min to 9 s at 5 mL/min, and then to 6 s at 10 mL/min for the three tested flow rates. The channel geometry could be the reason for this substantial variation at lower flow rates. While maintaining a constant height of the main channel throughout the device at 350 μm, the width of the main channel at the first row was narrower than the second row, 11.2 and 13.7 mm, respectively. Consequently, the local velocity between the two rows changed significantly at a fixed flow rate, with the velocity in the first row being higher than that in the second row. This contributed to a more significant transition time variation between the first and second row TRAs, particularly at lower flow rates.

Although the experiments presented in this section concluded that the flow rate of 10 mL/min was desirable for fluid exchange in the TRAs, it was observed in the preliminary experiments with SAP-MPs that this high flow rate would result in a high chance of particles escaping from the TRAs. Therefore, experiments in the rest of the paper were conducted at a flow rate of 5 mL/min. At this flow rate, the ethanol-to-water transition time and the solution exchange time difference were both kept at approximately 10 s, satisfying the criteria for fluid handling.

The total required time for swelling the SAP-MPs was assumed to be more than 150 s based on some preliminary experiments. The goal was to keep the transition time, T_t, and the fluid exchange time difference, T_d, below 10 s to have the lowest difference between the transition times of different TRAs.

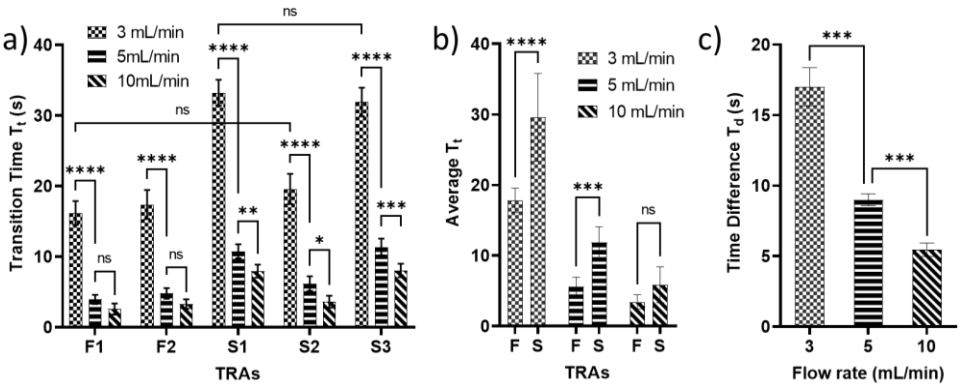

Figure 4-1. Fluid exchange characterization of the microfluidic device. (a) transition time (T_t) for fluid exchange from ethanol to water at different flow rates of 3, 5, and 10 mL/min for all TRAs, (b) average T_t of the first and second rows of TRAs at different flow rates, (c) time difference (T_d) between the minimum and maximum T_t at different flow rates. ∗: $P < 0.05$, ∗∗: $P < 0.01$, ∗∗∗: $P < 0.001$, ∗∗∗∗: $P < 0.0001$, ns: not significant ($N = 8$). Reprinted with permission from Elsevier [14].

4.2.2 SAP-MP Loading Time and Trapping Yield into TRAs

After the fluid exchange characterization, the particle trapping efficiency was examined by loading SAP-MPs into the TRAs. As shown in Figure 4-2, the average loading times per SAP-MP were 6.7, 8.7, and 21.5 s for the ethanol flow rates of 0.03, 0.15, and 0.3 mL/min, respectively. At the flow rate of 0.3 mL/min, particles escaped from the TRAs due to the fast movement of SAP-MPs.

It resulted in a long loading time to fill 80% of the traps (4 out of 5 TRAs). The loading time decreased significantly by decreasing the loading flow rate from 0.3 to 0.15 mL/min.

Further reduction in the flow rate to 0.03 mL/min did not result in any significant change in the SAP-MP loading time; however, it enhanced the chance of clogging the main channel before SAP-MPs could reach the expanding area due to the slow movement of the particles. Therefore, the loading flow rate was set at 0.15 mL/min in the rest of the experiments. As a result, it would take approximately 44 s for an operator to load five SAP-MPs into the TRAs. Based on this flow rate, and in a set of 10 experiments, it was found that the SAP-MPs trapping efficiency was 92%, i.e., 4.6 particles per experiment.

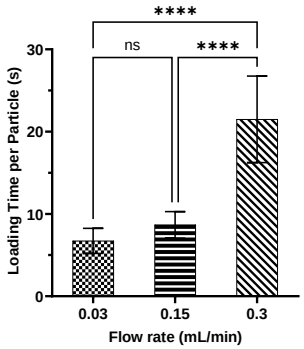

Figure 4-2. Average loading time per particle in the TRAs at three different loading flow rates of 0.03, 0.15, and 0.3 mL/min at the ethanol inlet. ∗∗∗∗: P < 0.0001, ns: not significant (N = 10). Reprinted with permission from Elsevier [14].

4.2.3 SAP-MPs Swelling Characterization

The swelling behavior of AA-Aam (4:1) SAP-MPs was characterized to validate the device performance. It was characterized by monitoring the time-lapse diameters of the SAP-MPs in the device and normalizing them to their initial diameters. As a control sample for device evaluation, non-neutralized SAP-MPs in a size range of 250 to 300 µm with the same synthesis condition were used to eliminate the effect of particle size and chemical composition on the swelling behavior. Within the 200s time window shown in Figure 4-3a, the size of a representative SAP-MP increased

from 270 µm to 478 µm with a VSR_{eq} and a SR of 5.54 m^3/m^3 and 0.04 $m^3/m^3.s$, respectively.

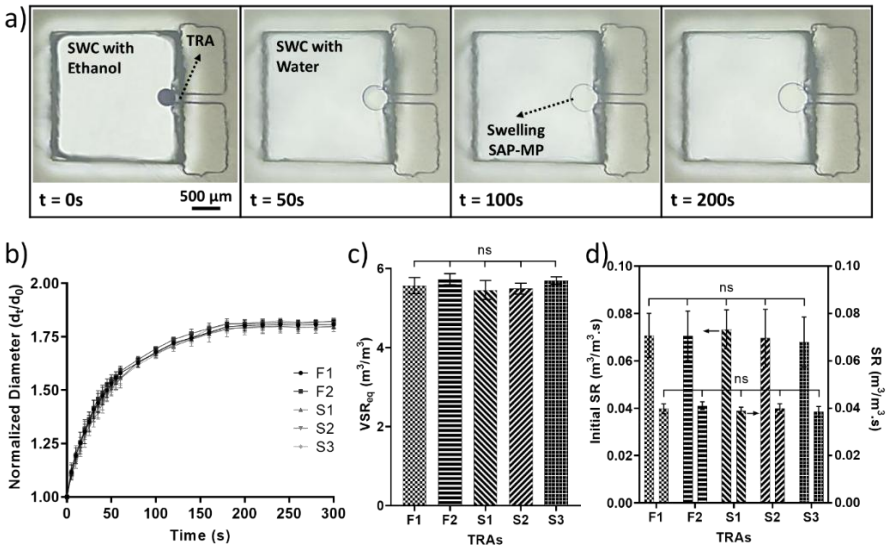

Figure 4-3. Swelling characterization of AA-Aam SAP-MPs using the microfluidic device. (a) swelling process of a representative SAP-MP at different times of being exposed to water. (b) dynamic swelling behavior of SAP-MPs trapped in different TRAs presented in terms of their normalized diameter (d_t/d_0) versus time. (c) VSR_{eq} and (d) initial SR and SR of SAP-MPs in different TRAs. ns: not significant (N=8). Reprinted with permission from Elsevier [14].

Figure 4-3b illustrates the dynamic swelling process of N=40 SAP-MPs in different TRAs (8 particles for each TRA), at the particle loading flow rate of 0.15 mL/min and water flow rate of 5 mL/min. The results revealed that the normalized diameter, d_t/d_0, of SAP-MPs trapped in different TRAs are not significantly different from each other, mainly due to the flow rate optimizations shown in Figure 4-2. For instance, at a flow rate of 5 mL/min, T_t for S3 was 13 s. Although this was the longest transition time between TRAs, it is only about 7% of the estimated equilibrium swelling time of 150 s. Thus, it had a minimal effect on the swelling behavior of these samples.

Figure 4-3c and d plot the VSR_{eq} and SR of the SAP-MPs in different TRAs. These values were statistically similar among different traps. It can be concluded that the SAP-MPs' swelling behavior is independent of their positions in the TRAs and SWCs, and the results of all TRAs can be combined and averaged for quantitative assessment of SAP-MPs swelling. As a result, the

VSR_{eq} and SR of N=40 SAP-MPs tested in this experiment was determined to be 5.59 ± 0.13 (m^3/m^3) and 0.039 ± 0.002 ($m^3/m^3.s$), respectively.

Experimental results were consistent with previous findings from the investigation of the swelling behavior of non-neutralized AA-Aam SAPs. Using a different method, Esteves [12] determined the VSR_{eq} of the SAP-MPs in the range of 50-500 μm that was 6.31 ± 2.73 (m^3/m^3). By comparing the standard deviation of VSR_{eq}, the microfluidic device-based technique yields more precise results. Moreover, the importance of this study lies in the real-time investigation of SAP-MPs with different particle sizes to understand its effect on their dynamic swelling behavior. Another remarkable result to emerge from the data is the experimental determination of SR of the SAP-MPs. To the best of our knowledge, this has never been reported. Using this method of real-time characterization, the SR of SAP-MPs can be investigated at any time during the swelling process. For instance, the initial SR of the SAP-MPs at the beginning of the swelling was 0.068 ± 0.010 ($m^3/m^3.s$), which is about 75% higher than the average SR reported in the literature using Eq. 4 [124].

4.2.4 Effect of ND on SAP-MPs Swelling Behavior

It has been reported that the ND of AA plays an essential role in optimizing the swelling behavior of SAPs [125, 126]. Therefore, the effects of ND in the range of 0% to 100% on the VSR_{eq} and SR of SAP-MPs were investigated while showing the device's effectiveness for parametric studies. Figure 4-4a illustrates the dynamic swelling behavior of SAP-MPs with various ND. For all levels of ND, the VSR increased sharply initially before reaching a plateau. Experimental results reveal that VSR_{eq} strongly depends on the ND of the AA. According to Figure 4-4b, the VSR_{eq} of SAP-MPs increased from 5 m^3/m^3 to 80 m^3/m^3 as the ND of AA increased from 0% to 90%. Then, it

dramatically decreased to 25 m^3/m^3 at ND of 100%. Under the experimental conditions, the SAP-MPs with the highest VSR_{eq} were those with an ND of 90%. This behavior is explicable using Flory's network theory [51]. In this theory, the swelling ability of an ionic network depends on the rubbery elasticity, ionic osmotic pressure, and polymer-solvent affinity. According to the reaction below, when acrylic acid is neutralized with sodium hydroxide, the negatively charged carboxyl groups attached to the polymer chains enhance the polymer's affinity to water. The promoted ionic concentration inside the network generates an electrostatic repulsion that tends to expand the network. In addition, by increasing the ND, hydrogen bonds between carboxyl groups break, and the crosslinking density decreases.

$$-CH_2CH(COOH) + Na^+OH^- \rightarrow -CH_2CH(COO^-) + Na^+ + H_2O$$

However, considering Manning's counterion condensation theory [127], an increase in ND beyond a certain threshold introduces a critical ionic concentration in the network, leading to counterion condensation effects. As ND increased beyond a certain point, the additional sodium counterions accumulate near the negatively charged carboxylate groups, partially neutralizing the electrostatic repulsion responsible for network expansion. This counterion condensation reduces the effective charge density of the polymer, leading to a collapse of the network structure and a sharp decline in swelling capacity. This explains why the VSR_{eq} of SAP-MPs decreases significantly at ND = 100%, as the polymer chains undergo charge screening and reduced electrostatic repulsion, limiting water absorption. No significant differences were found in the literature regarding the effect of the ND on SAP-MPs swelling behavior [128, 129].

Figure 4-4c shows the SR of the SAP-MPs with different ND. Increasing the ND increases the repulsive force between charged functional groups inside the structure. It leads to an increase in the flexibility of the structure. At ND of 0, low charged functional group and repulsive force resulted in a dense structure. Therefore, the SR was minimum and was about 0.03 m^3/m^3.s. Incraseing ND to 25% improved the SR significantly to 0.19 m^3/m^3.s. Further increase in the ND resulted in a gradual increase in SR to 1.11 m^3/m^3.s for 90% neutralized SAP-MPs. Higher ND decreased the SR dramatically to 0.3 m^3/m^3.s. As mentioned previously, at this level of neutralization, Manning's counterion condensation mechanism becomes significant. The accumulation of sodium counterions reduces effective charge repulsion, leading to polymer chain contraction and decreased water permeability. As a result, the SR of fully neutralized (100% ND) SAP-MPs dropped dramatically to 0.3 m^3/m^3.s.

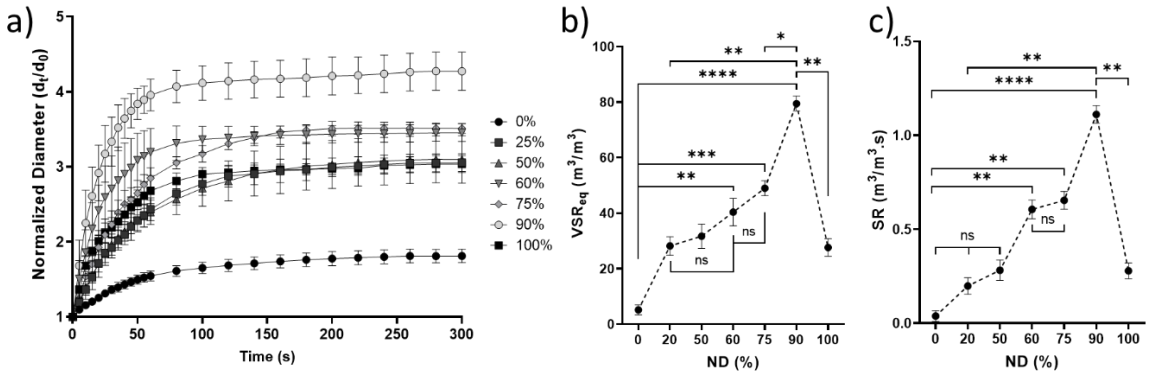

Figure 4-4. Effect of neutralization degree (ND) on the swelling behavior of AA-Aam-based SAP-MPs tested in the microfluidic device. (a) dynamic swelling behavior of SAP-MPs with different ND (0-100% in the legend). (b) VSR_{eq} and (c) SR of SAP-MPs with different ND. ∗: P < 0.05, ∗∗: P < 0.01, ∗∗∗: P < 0.001, ∗∗∗∗: P < 0.0001, ns: not significant (N = 8). Reprinted with permission from Elsevier [14].

4.3 Conclusion

In this chapter, a microfluidic platform was successfully designed and fabricated to enable real-time characterization of SAP-MPs, specifically targeting their swelling behavior. This novel device allowed for the precise analysis of VSR and SR of the SAP-MPs under controlled environmental conditions. It provides real-time data on the swelling dynamics of AA-Aam-based SAP-MPs. The platform's ability to trap and observe individual SAP-MPs has proven to be effective, with experimental results demonstrating the reproducibility and accuracy of the measurements.

The fluid exchange characterization optimized the device's operational parameters, such as flow rate, to reach the minimum T_t and T_d between TRAs, while the loading time and efficiency of trapping are minimum and maximum, respectively. The results showed that selecting a 5 mL/min flow rate for water ensured a T_d of approximately 10 seconds between different TRAs. For ethanol, a flow rate of 0.15 mL/min was used to effectively trap the SAP-MPs. The measured SR and VSR_{eq} values were 0.039 ± 0.002 $m^3/m^3.s$ and 5.59 ± 0.13 m^3/m^3, respectively.

The investigation into the effect of ND on swelling behavior indicated that the highest VSR_{eq} of 80 m^3/m^3 and SR of 1.11 $m^3/m^3.s$ were achieved at an ND of 90%. Beyond this point, both VSR_{eq} and SR decreased, illustrating the over-screening effect of electrostatic repulsion at higher ND levels.

Chapter 5

Parametric Investigation of SAP-MPs[1]

5.1 Introduction

This chapter focuses on the second objective of this research, which is investigating the effect of different parameters such as particle size, crosslinker concentration (Cr), monomer concentration (AA), and neutralization degree (ND) on VSR_{eq}, SR, and CT of SAP-MPs using developed microfluidic platform in objective one. The aim is to characterize the effect of each parameter and their synergistic effects on the swelling behavior of the SAP-MPs at different size levels. This

[1] Parts of this chapter are extracted from: 2. Tabesh, E., Zabihihesari, A. R., Rezai, P., & Leung, S. N. "In-situ investigation of swelling dynamics of acrylamide-acrylic acid superabsorbent microparticles at a single particle level". *Macromolecular Rapid Communications*, 2025.

helps us to selectively focus on a single parameter without coupling the effects of other parameters. For example, investigating the effect of Cr at different particle size levels.

To achieve this objective, the microfluidic-based single SAP-MP characterization was used to investigate the effects of different parameters. SAP-MPs with diameters ranging from 70 μm to 300 μm was at focus. The response surface method (RSM) was utilized to design experiments. Additionally, the correlations between particle size and the swelling behavior of SAP-MPs was investigated. To elucidate the involved kinetic mechanisms, two different kinetic models, i.e., Pseudo-first-order (PFO) and Pseudo-second-order (PSO) models, were applied and compared to determine which one provides a more accurate prediction of the swelling behavior of SAP-MPs. The microfluidic-based single SAP particle characterization approach enables understanding the structure-to-property relationship of individual particles. By analyzing the properties of individual SAP-MPs, it is possible to gain a deeper insight into the factors that influence their swelling behaviors to optimize their performance in various applications.

5.2 Results and Discussion

In this section, first, we present the results of physical and chemical characterization of the SAP-MPs using FTIR, TGA, and SEM. Then, their swelling behaviors, consisting of the impact of various factors on VSR_{eq} and SR, were examined, using RSM. Finally, the section concludes with an evaluation of different kinetic models.

5.2.1 SAP-MPs Characterization

5.2.1.1 Chemical Structure Analysis

FTIR was employed to examine the chemical structure of the synthesized SAP-MPs, specifically

to confirm the polymerization process. This was achieved by comparing the FTIR spectra of the raw monomers, AA, and Aam, with the resultant SAP-MPs. The spectral shifts, emergence, and disappearance of characteristic peaks were analyzed to identify structural changes indicative of successful polymerization. Figure 5-1 presents the FTIR spectra of SAP-MPs, AA, and Aam.

The spectra showed significant differences, confirming co-polymerization. For instance, in both AA and Aam, there was a peak at 980 cm^{-1} that is characteristic of C=C bending vibrations. This peak, however, was absent in the SAP-MPs spectrum, suggesting the consumption of C=C bonds during co-polymerization. In the spectra of both monomers, peaks representing C-H and O-H bond vibrations are visible at 3000 cm^{-1} and 3355 cm^{-1}, respectively, whereas the N-H bond in Aam appears at 3180 cm^{-1}. These peaks also appear in the SAP-MPs spectrum, albeit slightly shifted to 3421 cm^{-1}, 3200 cm^{-1}, and 2930 cm^{-1}, respectively. Moreover, the peaks at 1626 cm^{-1} in AA and 1612 cm^{-1} in Aam, related to the stretching of C=C bonds, are absent in the SAP-MPs. In contrast, the C=O stretching bands, initially observed at 1707 cm^{-1} in AA and 1673 cm^{-1} in Aam, shift to 1710 cm^{-1} in the SAP-MPs. The overlapping structural characteristics of the monomers at specific wavelengths manifest as subtle peaks at 1710 cm^{-1} and 1660 cm^{-1} (C=O) in the SAP-MPs spectrum [130, 131]. Significant shifts, emergence, and disappearance of characteristic peaks confirmed the successful co-polymerization of AA and Aam. SAP-MP samples of varying sizes exhibited identical spectra, confirming the consistency of their chemical composition (data not shown due to similarity).

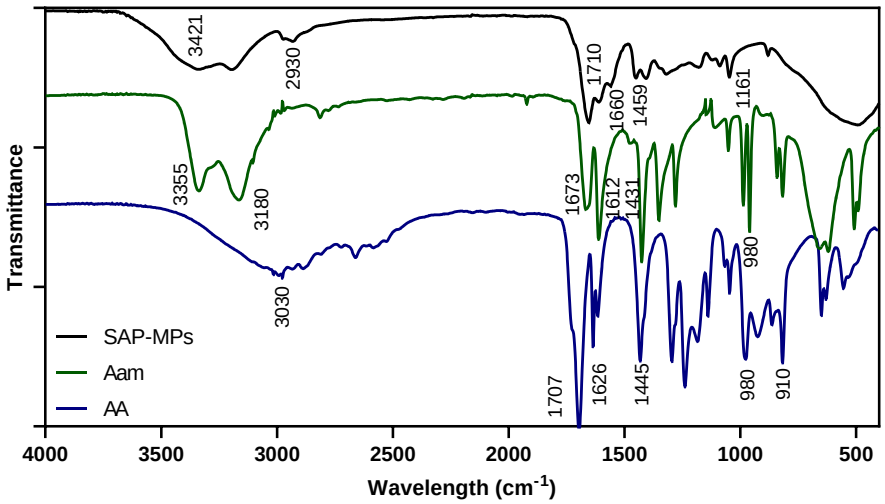

Figure 5-1. FTIR spectra of AA, Aam, and the synthesized SAP-MPs (sample No. 18 in table 1).

5.2.1.2 Thermal Analysis

TGA was conducted to investigate the thermal stability and degradation temperature of the synthesized SAP-MPs. The TGA thermogram for the sample made with recipe No. 18 in Table 1 is used herein as a case example. TGA thermograms were expected to show the onsets of water loss and thermal degradation of polymeric structure. Figure 5-2 illustrates the TGA thermograms of SAP-MPs, showing different stages of water desorption, dehydration reactions, and, ultimately, degradation reactions.

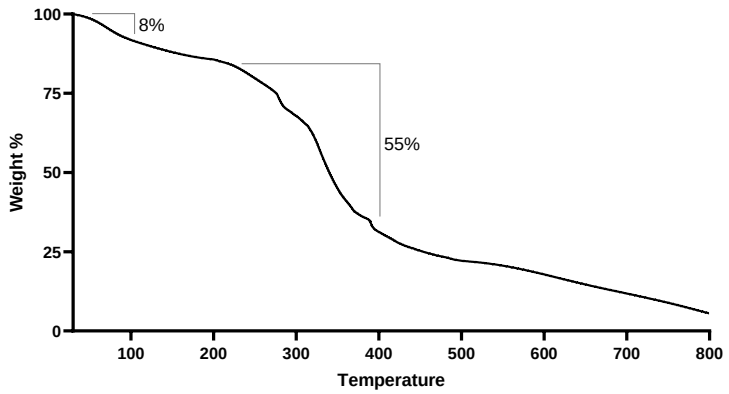

Figure 5-2. TGA graph of SAP-MPs in an inert atmosphere (sample No. 18 in Table 1).

Initially, there was a weight loss of approximately 8% of the total mass below 100 °C, attributed

to water evaporation from the samples. The physically absorbed water in the SAP-MPs was released upon heating, a process that is predominantly physical and known as water desorption. The degradation stage, occurring between 250-450°C, resulted in a substantial weight loss of 55%. This stage was likely raised from the successive cleavage of the polymeric hydrogel backbone, involving various dehydration reactions such as dehydration of amide groups in Aam and decomposition of carboxylic acid groups from AA. Depolymerization primarily occurred due to the disruption of crosslinks between polymeric chains, facilitated by the rupture of C-O and C-C bonds within the molecular rings. This process generates byproducts such as CO, CO_2, and H_2O. The decomposition of carboxyl groups from AA and amide groups from Aam occurs within the temperature range of 340–500 °C [132]. Beyond 450°C, the mass reduction rate remains relatively constant, signifying the robust thermal stability of the hydrogel samples [133].

5.2.1.3 Morphological Analysis

SEM was employed to investigate the morphology of dry and swollen SAP-MPs. Figure 5-3 depicts distinct morphological differences between 90 µm and 270 µm SAP-MPs in their dry and swollen states.

Figure 5-3a-d show the surface morphology of SAP-MPs synthesized in one batch, with sizes of 90 µm (a, b) and 270 µm (c, d) in the dry state. Both particle sizes exhibit a spherical and dense structure; however, the smaller 90 µm SAP-MPs display a remarkably smooth surface morphology. In contrast, the larger 270 µm SAP-MPs show rougher surfaces, which is likely due to higher mechanical stress during the drying process. Such stress induces surface deformation that is more pronounced in larger particles due to their increased rigidity [134, 135].

Figure 5-3e-h depict the morphology of 90 and 270 µm SAP-MPs after reaching equilibrium. Both

particle sizes show highly porous structures, but the pores differ in size and distribution. The 90 µm SAP-MPs exhibit larger and less densely packed surface pores compared to the smaller, tightly packed pores observed in the 270 µm SAP-MPs. The larger pores in the smaller particles after freeze-drying can be attributed to their higher water absorption capacity of smaller particles.

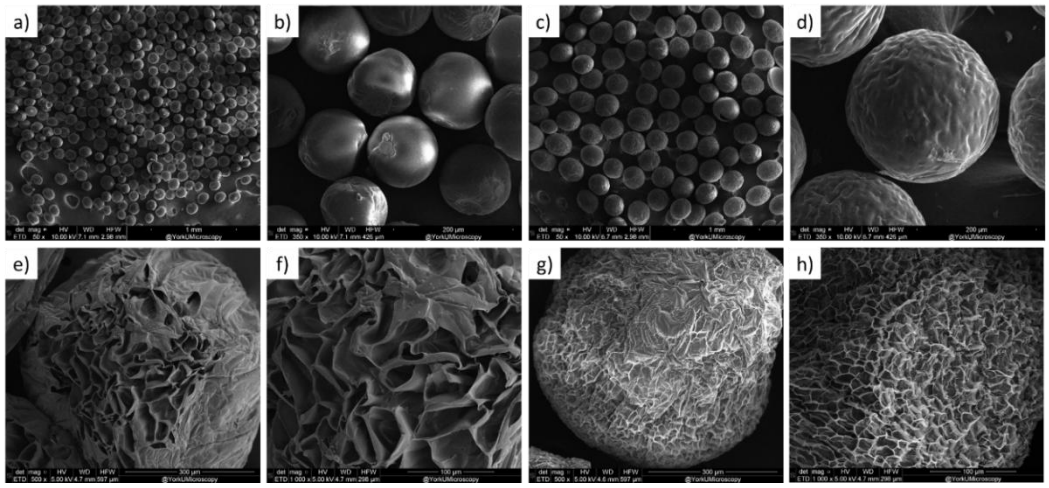

Figure 5-3. SEM images with different magnifications of (a-d) dry and (e-h) swollen SAP-MPs. The surface morphology of smaller 90 µm SAP-MPs (a, b, e, f) was compared to that of larger 270 µm SAP-MPs (c, d, g, h).

5.2.2 Swelling Behaviors of SAP-MPs

5.2.2.1 Response Surface Methodology (RSM)

The effects of Cr, AA, ND, and particle size, as well as their interactions, on VSR_{eq} and SR were investigated using RSM. Experimental ranges were set between 0.2–2.0% for Cr, 10–90% for AA, 50–100% for ND, and 90–270 µm for particle size. In all experiments, when evaluating the effect of a specific parameter, the other parameters were fixed at AA = 50%, Cr = 1.13%, and ND = 75%. Statistical analyses, including ANOVA, confirmed the significance of these factors and their interactions. Pareto charts and normal probability plots validated the model assumptions and residual normality.

5.2.2.1.1 Effect of Cr

Increasing the Cr from 0.2% to 1.13% and then to 2% significantly decreased VSR_{eq} from ~360

(m^3/m^3) to ~150 (m^3/m^3) and then to ~50 (m^3/m^3) (Figure 5-4a). Similarly, SR diminished from ~4.2 ($m^3/m^3 \cdot s$) to ~2.5 ($m^3/m^3 \cdot s$) and then ~1.8 ($m^3/m^3 \cdot s$) (Figure 5-4b). The reduction in both VSR_{eq} and SR can be attributed to the increased degree of crosslinking. As Cr increases, the polymer network becomes more tightly bound, resulting in a higher crosslinking density. The tighter network structure restricts the mobility and expansion of polymer chains, leading to greater rigidity and reduced flexibility of the polymer network. This rigidity limits the ability of the chains to accommodate water molecules, thereby diminishing the overall swelling capacity. The combined effects of reduced polymer chain mobility and increased network rigidity contribute to the observed decline in both VSR_{eq} and SR as Cr increases [51, 136].

5.2.2.1.2 Effect of AA

Increasing the AA from 10% to 50% led to a significant increase in the VSR_{eq}, rising from 50 m^3/m^3 to 120 m^3/m^3 (Figure 5-4a). This improvement can be attributed to the higher concentration of hydrophilic carboxylic groups (-COOH) in the polymer network. Carboxyl groups enhance water absorption by forming strong hydrogen bonds through both their hydroxyl (-OH) and carbonyl (-C=O) components. Additionally, their ability to ionize into carboxylate ions ($-COO^-$) at higher pH levels generates significant osmotic pressure, further increasing the swelling capacity of the hydrogel. In contrast, while amide functional groups ($-CONH_2$) in Aam also form hydrogen bonds with water, they lack ionizable properties, making the carboxyl groups in AA more effective at enhancing water absorption and swelling behavior.

However, when AA was further increased from 50% to 90%, the VSR_{eq} exhibited only a slight increase to 140 m^3/m^3. This diminished improvement suggests a saturation effect, where additional carboxylic groups contribute minimally to swelling due to the dominant role of elastic forces in the expanded polymer network. As swelling progresses, the elastic restoring forces within the

network increasingly resist further expansion, thereby limiting additional gains in VSR_{eq} despite the higher AA.

Regarding the SR, increasing AA from 10% to 50% resulted in a moderate increase, from less than 1 $m^3/m^3 \cdot s$ to approximately 2.5 $m^3/m^3 \cdot s$ (Figure 5-4b). This increase is primarily driven by the enhanced hydrophilicity of the polymer network, which facilitates faster water diffusion into the SAP-MPs. Conversely, further increasing AA to 90% caused a slight decrease in SR to about 2 $m^3/m^3 \cdot s$. This non-linear behavior may be attributed to increased network rigidity at higher AA. The higher crosslinking density and tighter network structure, resulting from the more abundant -COOH groups, restrict chain mobility and slow water penetration into the network, thereby reducing the swelling kinetics [137].

5.2.2.1.3 Effect of ND

Although ND is recognized as a key factor in improving the swelling capacity of SAP-MPs, Increasing ND from 50% to 75% and then to 100% resulted in a moderate increase in the VSR_{eq}, from approximately 90 m^3/m^3 to 120 m^3/m^3 and 130 m^3/m^3, respectively (Figure 5-4a). This improvement can be attributed to the ionization of carboxyl groups within the polymer network, which generates electrostatic repulsion between carboxylate anions (COO^-) and increases osmotic pressure, leading to enhanced water absorption [138].

However, when ND increased from 75% to 100%, the enhancement in VSR_{eq} was less pronounced. This behavior can be explained by the combined effects of polymer network flexibility, elastic restoring forces, and counterion shielding. At higher ND, the polymer chains are already highly ionized and significantly stretched, reaching a physical expansion limit where further electrostatic repulsion provides diminishing returns. The elastic force within the network becomes a dominant opposing factor, restricting further chain expansion and limiting additional increases in swelling

capacity. Additionally, the counterion shielding effect—where excess Na^+ ions form COO^-Na^+ complexes—reduces the effective electrostatic repulsion and further contributes to the observed plateau in VSR_{eq}.

Regarding the SR, increasing ND initially enhances water penetration and swelling kinetics by loosening the polymer network structure, facilitating the diffusion of water molecules into the hydrogel matrix (Figure 5-4b). However, at higher ND levels, the SR stabilizes as the network approaches its maximum physical expansion limit, where additional ionization no longer significantly alters the diffusion pathways or chain mobility within the polymer matrix. This trend has been observed in studies investigating the role of ND in similar hydrogel systems, where both elastic forces and counterion effects are identified as key limiting factors [117].

5.2.2.1.4 Effect of Particle Size

As discussed earlier (Figure 5-3a–d), decreasing the particle size from 270 µm to 90 µm significantly affects surface morphology and swelling behavior. The smaller SAP-MPs (90 µm) exhibit smoother surfaces, while the larger SAP-MPs (270 µm) display rougher surfaces due to higher mechanical stress and greater polymer chain entanglement during the drying process [134, 135]. These structural differences play a critical role in the swelling performance of SAPs.

Decreasing the particle size from 270 µm to 90 µm led to a notable increase in the VSR_{eq}, from approximately 50 m^3/m^3 to 150 m^3/m^3 (Figure 5-4a). As illustrated in the SEM micrographs (Figure 5-3e–h), this enhanced water absorbency in smaller SAP-MPs is primarily attributed to their larger surface area-to-volume ratio, which facilitates greater interaction with the surrounding solvent and improves water uptake capacity [139, 140].

The physical entanglement of polymer chains also influences swelling behavior. Larger particles,

with their greater internal volume, exhibit higher degrees of chain entanglement due to increased spatial overlap among polymer chains. This entanglement restricts chain mobility and flexibility, limiting water molecule diffusion and reducing the swelling capacity of larger SAP-MPs [135, 140]. In contrast, the smaller SAP-MPs exhibit reduced chain entanglement due to their limited volume for polymer chain interactions during synthesis. This reduced entanglement creates a more flexible polymer network structure, enabling greater swelling and the formation of larger pores after freeze-drying, as evident in the SEM images (Figure 5-3e–h) [139]. These findings align with previous studies demonstrating that reduced entanglement and crosslink density promote swelling flexibility and porosity [134, 135, 139].

Additionally, decreasing the particle size from 270 μm to 90 μm resulted in a significant increase in the SR, from approximately 1.5 $m^3/m^3 \cdot s$ to 7 $m^3/m^3 \cdot s$ (Figure 5-4b). The increased SR can be explained by the larger surface area-to-volume ratio of smaller particles, which facilitates faster interaction with the surrounding solvent. Moreover, the reduced particle size shortens the internal diffusion path for water molecules, expediting their penetration and swelling process.

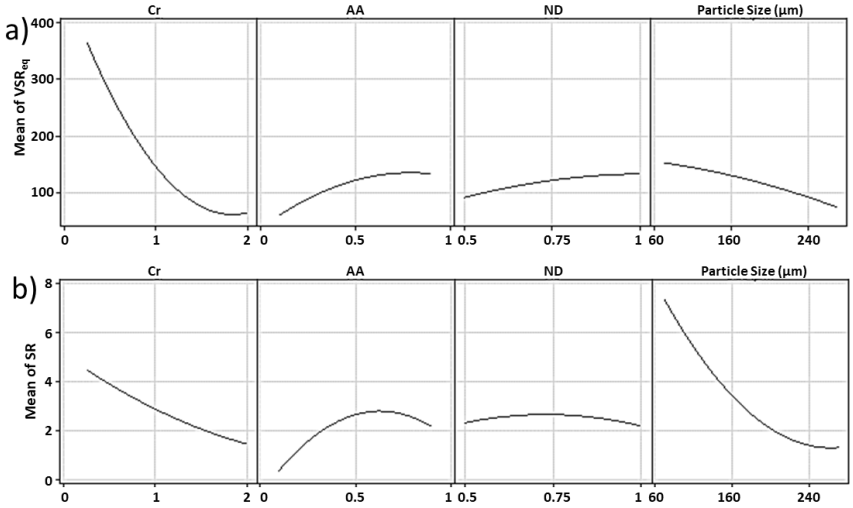

Figure 5-4. The effects of parameters; including Cr, AA, ND, and particle size on a) VSR_{eq} and b) SR. Other factors were held constant at middle levels (Cr: 1.13%, AA: 50%, ND: 75%, size: 200 μm).

Figure 5-5a and b show the two-way interaction between AA and Cr as well as that between ND and Cr, respectively. In both cases, Cr was the dominating factor compared to AA and ND. An increase in Cr resulted in a consistent decrease in VSR_{eq}. Notably, at Cr > 1.3%, VSR_{eq} reached its minimum, indicating that Cr is the predominant factor influencing swelling behavior. The decrease in VSR_{eq} with increasing Cr can be attributed to the denser crosslinking within the SAP-MPs that restricts the expansion of polymer chains. Under these conditions, changes in AA and ND had minimal effect on VSR_{eq}, reinforcing that crosslinking density is the dominant parameter over the concentration of functional groups or the degree of neutralization.

Figure 5-5c shows the interaction between particle size and Cr. At low Cr, decreasing particle size caused VSR_{eq} to increase significantly, from approximately 200 (m^3/m^3) to over 450 (m^3/m^3). At Cr > 1.3%, the dominating factor is crosslinking density, and VSR_{eq} reaches its minimum regardless of particle size. This observation can be attributed to the dominant role of crosslinking density at high Cr, where the dense crosslinking restricts the polymer chains' ability to swell, minimizing the effect of particle size. Conversely, at low Cr, the physical entanglement of polymer chains becomes more significant in determining the swelling behavior. So, larger particles increase the effectiveness of chain entanglements, particle size has negative impact on VSR_{eq} [13, 141].

Figure 5-5d shows the interaction between ND and AA. At lower levels of AA and ND, the limited number of carboxylic groups and the low ND result in reduced osmotic pressure, leading to low VSR_{eq} (less than 50 m^3/m^3). However, at high AA and ND, the larger number of carboxylic groups significantly enhances the water absorption capacity of the SAP-MPs. In this case, increasing the ND neutralizes more carboxylic groups, increasing charge density and osmotic pressure. As a result, both high AA and increased ND synergistically improve the VSR_{eq} (about 150 m^3/m^3).

Notably, in all cases, individual factors such as high AA or high ND alone are not able to significantly change the VSR_{eq}, while their combined effect is more pronounced.

Figure 5-5e and f show the correlation between particle size and AA as well as that between particle size and ND, respectively. In both plots, the maximum VSR_{eq} (about 250 m^3/m^3) was achieved at a small particle size with higher AA and ND. Similarly, either small particle size or high AA/ND alone does not significantly affect VSR_{eq}, but their combined effect leads to substantial improvement. Specifically, small size and high AA, or small size and high ND consistently lead to high VSR_{eq}.

It is important to note that in these results, Cr was fixed at 1.13%, which could influence the effect of other factors. The fixed crosslinking density may limit the observed impact of AA, ND, and particle size on VSR_{eq}, as Cr plays a dominant role in determining the swelling behavior.

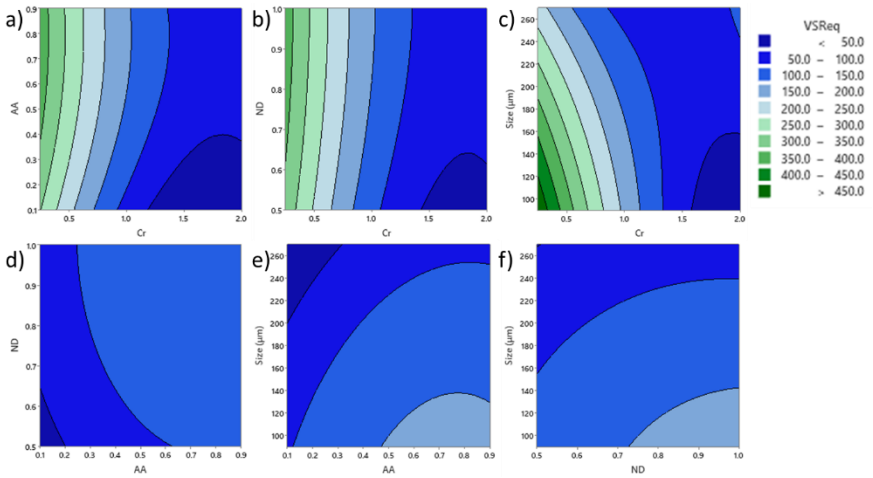

Figure 5-5. The interaction effects of parameters on VSR_{eq}. The interactions are demonstrated for a) AA and Cr, b) ND and Cr, c) particle size and Cr, d) ND and AA, e) particle size and AA, and f) particle size and ND. Other factors held constant at middle levels (Cr: 1.13%, AA: 50%, ND: 75%, size: 200 µm).

Figure 5-6a and b illustrate the interaction between AA and ND with Cr, respectively. In both cases, Cr acts as the dominant factor affecting the SR of the SAPs. However, the effect of AA appears to

be more significant than ND, as observed in Figure 5-6d, which shows the relationship between ND and AA. In general, an increase in Cr leads to a consistent decrease in SR across all levels of AA and ND. This trend indicates that crosslinker density plays a predominant role in limiting SR, as higher Cr results in a denser, more rigid polymer network, which slows down the swelling process. Comparing the effects of AA and ND suggests that the presence of additional carboxyl groups from AA, combined with an optimal ND, enhances the hydrophilic nature of the SAPs, thereby improving SR.

Figure 5-6c shows the interaction between particle size and Cr. The results indicate that particle size has a significantly dominant effect on SR. At a particle size of 270 μm, increasing Cr did not significantly affect SR. This may be due to the lower surface area-to-volume ratio of larger particles, where the swelling process is primarily controlled by the diffusion of water into the bulk of the particle, rather than the crosslinking density. As a result, Cr has a minimal influence on SR in larger particles. However, decreasing the particle size to 90 μm led to a significant decrease in SR across all levels of Cr. This can be attributed to the increased surface area-to-volume ratio in smaller particles. For smaller particles, the surface area plays a more prominent role, and the degree of crosslinking can substantially influence the rate of water absorption.

Figure 5-6e and f show the interaction between particle size with AA and ND, respectively. In both cases, a clear decrease in SR was observed with increasing particle size. This pattern is consistent across various levels of AA and ND, indicating that particle size is the most influential factor in determining SR. Notably, at particle sizes >200 μm, the effect of size completely dominates SR, and changes in either ND or AA have no significant impact on SR. Under these conditions, SR was observed to reach its minimum value regardless of the levels of ND or AA.

Overall, the results demonstrate that Cr is the dominant factor affecting VSR_{eq} due to its impact on crosslinking density and polymer network rigidity, whereas particle size is the dominant factor influencing SR, primarily through its effect on surface area-to-volume ratio and diffusion pathways.

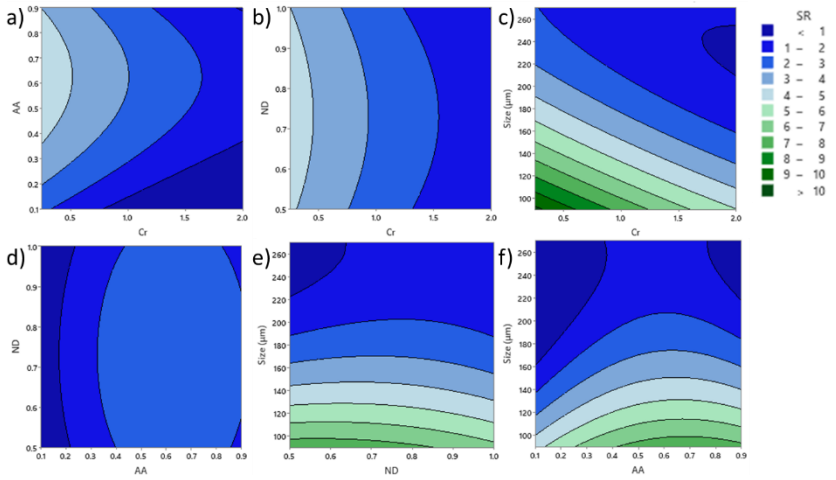

Figure 5-6. The interaction effects of influencing parameters on SR. The interactions are demonstrated for a) AA and Cr, b) ND and Cr, c) particle size and Cr, d) ND and AA, e) particle size and AA, and f) particle size and ND. Other factors held constant at middle levels (Cr: 1.13%, AA: 50%, ND: 75%, size: 200 µm).

5.2.2.2 Kinetic Studies

Studying swelling kinetics is crucial for understanding the mechanism behind the swelling process, optimizing conditions for maximum swelling capacity, and explaining the SR of SAP-MPs. In this study, we utilized a single-particle characterization method, which minimizes external factors such as water interference between particles and delays in measurement. This method enables a precise assessment of the intrinsic swelling behavior of SAP-MPs, providing detailed insights into their swelling dynamics.

We applied two kinetic models—the PFO and PSO models—to fit the experimental data. The goal was to determine which model best describes the swelling behavior of SAP-MPs and to identify the dominant mechanisms contributing to their swelling. The R^2 was used to evaluate the

goodness-of-fit, comparing predicted and experimental VSR_{eq} values. By analyzing the effects of Cr, AA, ND, and particle size separately, we isolated the contribution of each factor to the swelling kinetics of SAP-MPs.

5.2.2.2.1 Effect of Cr

The kinetic data from the models and experimental results are summarized in Table 5-1. Figure 5-7a and b illustrate the experimental data and the PFO and PSO model predictions for the real-time swelling behavior of SAP-MPs under three Cr: 0.2%, 1.13%, and 2%. An increase in Cr resulted in a more rapid attainment of the equilibrium state, as evidenced by shorter times to reach the plateau for higher Cr. However, this increase in Cr also reduced the final plateau value of the VSR_{eq}, highlighting the trade-off between swelling speed and capacity.

Although both models showed high R^2 values, the PFO model consistently demonstrated slightly better performance compared to the PSO model. The ΔVSR_{eq} values, indicating the differences between experimental and model-predicted VSReq, were consistently low for the PFO model, remaining within 1% across all Cr levels. In contrast, the PSO model exhibited higher ΔVSR_{eq} values, ranging from 7% to 10%. This underscores the superior accuracy of the PFO model in predicting VSR_{eq} at varying Cr.

The excellent fit of the PFO model suggests that the swelling behavior of SAP-MPs is predominantly governed by physical diffusion processes, where water molecules migrate into the polymer matrix without forming strong chemical bonds [142]. The rate constant values (k_1) for the PFO model increased from 0.012 to 0.032 min^{-1} with increasing Cr, indicating that SAP-MPs with higher Cr reached equilibrium faster. This can be attributed to the reduced flexibility and mobility of the polymer network at higher Cr, which limits available sites for water absorption and results in a faster but reduced swelling process.

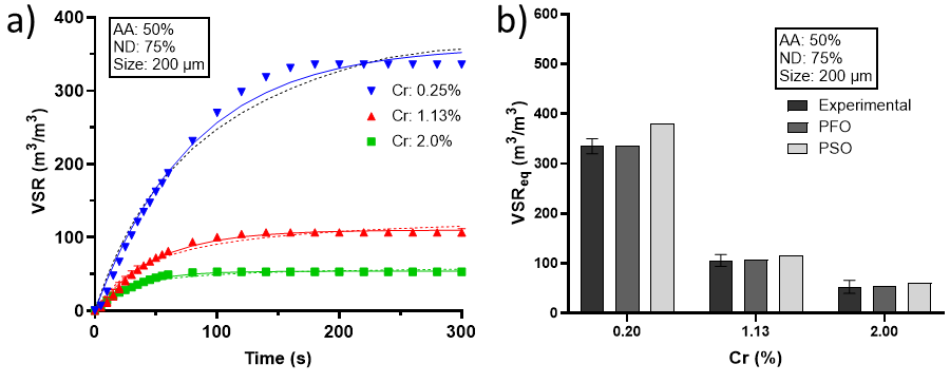

Figure 5-7. Experimental data and PFO and PSO model predictions of (a) the real-time swelling behaviors of SAP-MPs and (b) VSR_{eq} values under varying Cr. Solid lines represent the PFO model, while dashed lines represent the PSO model.

Table 5-1. Summary of experimental and model-predicted values for VSR_{eq}, R^2, rate constants (k_1 and k_2), and ΔVSR_{eq} for PFO and PSO modes with experimental values across different Cr.

Cr (%)	Experimental	PFO				PSO			
	VSR_{eq}	VSR_{eq}	R^2	k_1	ΔVSR_{eq} (%)	VSR_{eq}	R^2	k_2 (10^{-4})	ΔVSR_{eq} (%)
0.2	335.43	335.36	0.98	0.012	1%	370.99	0.98	0.200	10%
1.13	106.91	106.78	0.99	0.021	1%	115.11	0.97	1.600	7%
2	53.14	53.86	0.99	0.032	1%	57.92	0.97	6.900	7%

5.2.2.2.2 Effect of AA

Figure 5-8a and b show the experimental data and the PFO and PSO model predictions for SAP-MPs at different AA levels: 10%, 50%, and 90%. Increasing AA led to higher VSR_{eq} values, with an increase from 61.19 m^3/m^3 at 10% AA to 134.22 m^3/m^3 at 90% AA. The PFO model consistently exhibited higher R^2 values (0.99 for all AA levels) compared to the PSO model, which showed slightly lower R^2 values of 0.98, 0.97, and 0.96 for 10%, 50%, and 90% AA, respectively (Table 5-2).

The ΔVSR_{eq} values further highlighted the superior predictive performance of the PFO model. For the PFO model, ΔVSR_{eq} ranged from 1% to 5%, while the PSO model exhibited significantly higher ΔVSR_{eq} values, ranging from 7% to 11%. The PFO model's rate constants (k_1) increased

slightly with higher AA levels, from 0.014 to 0.023 min^{-1}, reflecting faster water absorption due to the enhanced hydrophilicity of the network.

The better fit of the PFO model indicates that the swelling process is largely governed by physical diffusion rather than chemical interactions, as additional hydrophilic groups (-COOH) at higher AA levels enhance water uptake without altering the fundamental diffusion-driven mechanism [137].

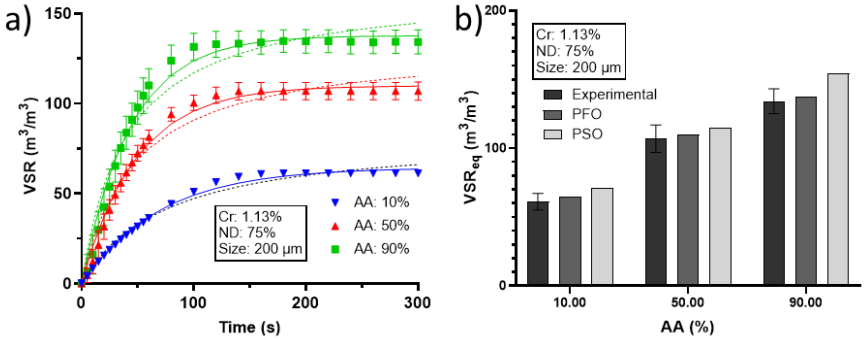

Figure 5-8. Experimental data and PFO and PSO model predictions of (a) the real-time swelling behaviors of SAP-MPs and (b) VSR_{eq} values under varying AA. Solid lines represent the PFO model, while dashed lines represent the PSO model.

Table 5-2. Summary of experimental and model-predicted values for VSR_{eq}, R^2, rate constants (k_1 and k_2), and ΔVSR_{eq} for PFO and PSO modes with experimental values across different AA.

AA (%)	Experimental	PFO				PSO			
	VSR_{eq}	VSR_{eq}	R^2	k_1	ΔVSR_{eq} (%)	VSR_{eq}	R^2	$k_2(10^{-4})$	ΔVSR_{eq} (%)
10	61.19	64.40	0.99	0.014	5%	70.72	0.98	1.600	11%
50	106.91	106.78	0.99	0.021	1%	115.11	0.97	1.600	7%
90	134.22	137.72	0.99	0.023	2%	151.00	0.96	1.500	11%

5.2.2.2.3 Effect of ND

Figure 5-9a and b illustrate the experimental data and the PFO and PSO model predictions for SAP-MPs at different ND: 50%, 75%, and 100%. Increasing ND significantly increased VSR_{eq}, from 79.13 m^3/m^3 at 50% ND to 113.23 m^3/m^3 at 100% ND. However, the time required to reach the equilibrium state remained largely unaffected by ND.

The R^2 values for the PFO model were consistently high across all ND levels (0.99), while the PSO model showed slightly lower R^2 values, ranging from 0.97 to 0.98 (Table 5-3). Similarly, ΔVSR_{eq} values for the PFO model ranged from 2% to 3%, significantly lower than the 7% to 12% observed for the PSO model. These results emphasize the superior predictive accuracy of the PFO model.

The rate constant values (k_1) for the PFO model decreased slightly with increasing ND, from 0.022 to 0.020 min^{-1}, suggesting that the network's physical expansion limits become a dominant factor at higher ND [138, 143].

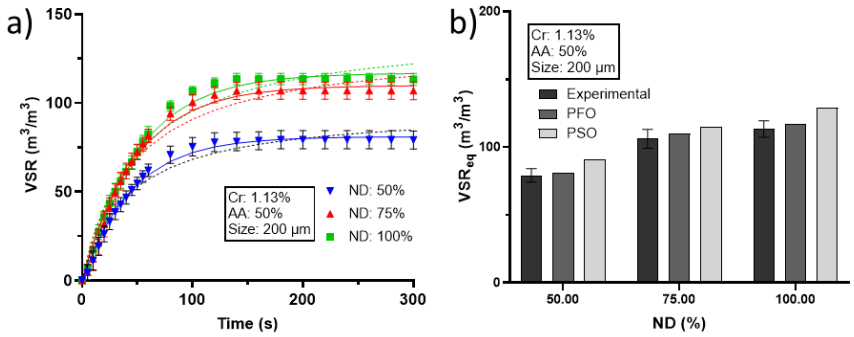

Figure 5-9. Experimental data and PFO and PSO model predictions of (a) the real-time swelling behaviors of SAP-MPs and (b) VSR_{eq} values under varying ND. Solid lines represent the PFO model, while dashed lines represent the PSO model.

Table 5-3. Summary of experimental and model-predicted values for VSR_{eq}, R^2, rate constants (k_1 and k_2), and ΔVSR_{eq} for PFO and PSO modes with experimental values across different ND.

ND	Experimental	PFO				PSO			
	VSR_{eq}	VSR_{eq}	R^2	k_1	ΔVSR_{eq} (%)	VSR_{eq}	R^2	$k_2(10^{-4})$	ΔVSR_{eq} (%)
50	79.13	80.98	0.99	0.022	2%	90.75	0.98	2.500	12%
75	106.91	106.78	0.99	0.021	1%	115.11	0.97	1.600	7%
100	113.23	116.81	0.98	0.020	2%	128.81	0.98	1.500	11%

5.2.2.2.4 Effect of particle size

The impact of particle size on swelling kinetics is shown in Figure 5-10a and b. A decrease in particle size resulted in higher VSR_{eq} values and a faster achievement of the equilibrium plateau

state. For particle sizes of 90, 140, 200, and 270 μm, the R^2 values for the PFO model ranged from 0.98 to 1.00, whereas the PSO model showed lower R^2 values, ranging from 0.92 to 0.99 (Table 5-4).

The ΔVSR_{eq} values for the PFO model were consistently low, ranging from 1% to 4%, compared to 7% to 10% for the PSO model. Additionally, the PFO rate constant values (k_1) decreased from 0.077 to 0.010 min^{-1} as particle size increased, reflecting the slower SR of larger particles. This trend highlights the critical role of particle size, with smaller particles exhibiting faster water uptake due to their larger surface area-to-volume ratio.

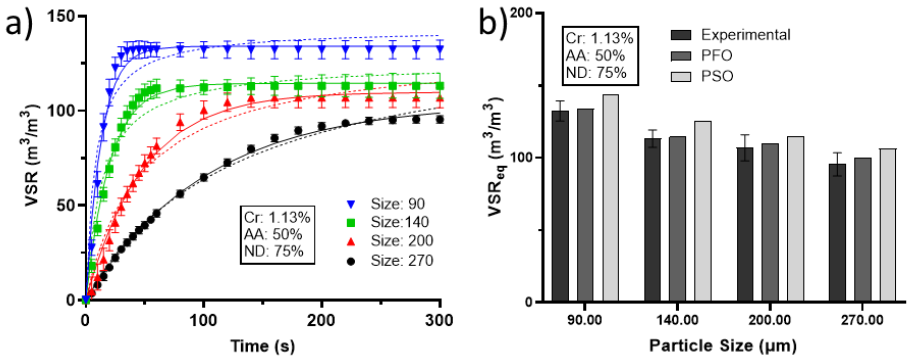

Figure 5-10. Experimental data and PFO and PSO model predictions of (a) the real-time swelling behaviors of SAP-MPs and (b) VSR_{eq} values under varying particle size. Solid lines represent the PFO model, while dashed lines represent the PSO model.

Table 5-4. Summary of experimental and model-predicted values for VSR_{eq}, R^2, rate constants (k_1 and k_2), and ΔVSR_{eq} for PFO and PSO modes with experimental values across different particle size.

Size (μm)	Experimental	PFO				PSO			
	VSR_{eq}	VSR_{eq}	R^2	k_1	ΔVSR_{eq} (%)	VSR_{eq}	R^2	$k_2(10^{-4})$	ΔVSR_{eq} (%)
90	132.27	134.02	0.98	0.077	1%	143.42	0.92	8.800	7%
140	113.19	114.45	0.99	0.050	1%	125.33	0.95	5.800	9%
200	106.91	106.78	0.99	0.021	1%	115.11	0.97	1.600	8%
270	95.41	99.23	1	0.010	4%	106.48	0.99	0.500	10%

Overall, both PFO and PSO models provided a good fit during the initial stages of swelling, where

water uptake is driven by both functional group interactions and physical diffusion. However, as the swelling process progresses, the PSO model's fit becomes less accurate. This behavior can be attributed to the saturation of functional group interactions, which occur predominantly in the early stages. Once these interactions stabilize, diffusion becomes the dominant mechanism driving the swelling process. The superior fit of the PFO model at later stages highlights the role of physical diffusion as the primary factor influencing the swelling dynamics of SAP-MPs.

5.3 Conclusion

This chapter provided an in-depth analysis of the swelling behavior of SAP-MPs by investigating the effects of particle size, Cr, AA, and ND. The experiments revealed that SAP-MPs with a smaller particle size of 90 µm exhibited a significantly faster SR of 10 m^3/m^3.s compared to larger particles of 270 µm, which had an SR of 1 m^3/m^3.s. In addition, smaller particles achieved a higher VSR_{eq} of 140 m^3/m^3, whereas larger particles reached only 100 m^3/m^3.

The Cr was found to inversely affect the VSR_{eq} and SR, with higher concentrations leading to a decrease in VSR_{eq} and SR. For instance, increasing the Cr from 0.2% to 2.0% resulted in a 85% reduction in VSR_{eq} from 350 m^3/m^3 to about 50 m^3/m^3. Similarly, AA and ND showed significant effects on the swelling behavior, with optimized conditions achieving a VSR_{eq} of up to 100 m^3/m^3 and an SR of 2 m^3/m^3.s.

These findings emphasize the importance of optimizing these parameters to enhance the performance of SAP-MPs for applications requiring precise control over swelling behavior. The study's use of a microfluidic platform enabled high-resolution, real-time analysis of these dynamic processes, providing valuable knowledge into the interplay between material composition and environmental conditions.

Chapter 6

Synthesize MXene nanoparticles and evaluate its application for bacterial enrichment in water samples[1]

6.1 Introduction

This chapter focuses on the results from objectives 3 and 4. It explores the application of SAP-MPs and their nanocomposites with MXene as a novel preliminary bacteria enrichment step in water analysis. The objective is to enhance the concentration of bacteria in water samples, thereby improving the sensitivity of the bacteria detection methods.

[1] Parts of this chapter are extracted from: Tabesh, E., Grumme, D., Herb, M., Rezai, P., Maleki, H., & Leung, S. N. "MXene/superabsorbent polymer composites for bacterial enrichment". Manuscript in preparation

To meet these objectives, MXene nanoparticles were first synthesized using a selective etching method. Following characterization, the BI-BO method was used to dope MXene nanoparticles into SAP-MPs, which were synthesized in previous objectives. After optimizing the BI-BO method's parameters. The physical, chemical, and swelling properties of the nanocomposite SAP-MPs were characterized and compared with those of the SAP-MPs. Subsequently, a bacterial enrichment test was conducted to assess their performance and determine the effective parameters.

6.2 Results and Discussion

In this section, we first present the results of the physical and chemical characterization of the synthesized MXene using XRD, FTIR, TGA, and SEM. Then, the synthesis of MXene/SAP-MPs will be investigated using the same characterization methods, followed by an examination of their swelling behaviors. Finally, the bacterial enrichment test will be performed and analyzed using *E. coli* as the sample bacteria.

6.2.1 MXene synthesis

MXene was synthesized from a MAX phase through in-situ etching with HF. Figure 6-1a illustrates the XRD spectra of the synthesized MXene. The strong peak at around 4-5° corresponds to the (002) plane, a characteristic peak of MXene, indicating the successful formation of its layered structure. Additional peaks observed at 17° and 28° correspond to the (004) and (006) planes, respectively, reflecting higher-order reflections consistent with the periodic arrangement of Ti_3C_2 layers influenced by surface terminations. The absence of significant peaks at 9.5°, 38°, and 60° indicates the successful removal of the MAX phase. The absence of these peaks confirms the effective etching of the aluminum layer, ensuring the purity of the synthesized MXene [144, 145].

SEM was employed to investigate the morphological characteristics of MAX and MXene. As

shown in Figure 6-1b, the SEM image of the MAX phase exhibits a densely packed and layered structure which are characteristic of MAX phases. This smooth and unetched surface morphology confirms the material's integrity prior to etching [93]. In contrast, the structure of MXene shows a more delaminated and accordion-like appearance. These features suggest an increased surface area, with a rougher texture compared to the MAX phase. This multilayer morphology not only confirms the successful synthesis of MXene but also implies potential changes in functional properties.

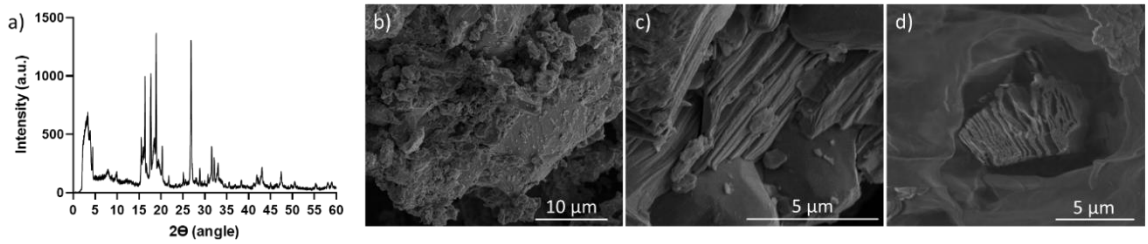

Figure 6-1. a) XRD pattern of MAX and MXene. SEM image of MAX (b) and MXene sheets before delamination (c, d)

Synthesized MXene was loaded into SAPs using the BI-BO method. The increasing concentration of MXene in the SAPs with different cycles is qualitatively illustrated in Figure 6-2a (real images of SAPs), which displays the bare SAPs and the SAPs after the first, third, fifth, and seventh BI-BO cycles. It is evident that the SAPs, after undergoing three cycles, became darker compared to the SAPs with only one cycle.

To quantitatively optimize the doping process, various number of BI-BO cycles were evaluated by measuring the MXene concentration in the solution using UV-Vis spectroscopy and a calibration curve before and after each doping cycle. The amount of doped MXene into SAPs was calculated. Figure 6-2b illustrates the percentage of MXene in the SAPs after different BI-BO cycles. The results showed that after the first BI-BO cycle, the MXene concentration increased to 1.7%.

Increasing the BI-BO cycles to three raised the MXene content of the SAPs from 1.7% to 2.3%. However, the rate of MXene content increase decreased with additional BI-BO cycles. Increasing the BI-BO cycles to five and seven raised the MXene content to 2.7% and 3.1%, respectively.

When dry SAPs were immersed in an aqueous solution of MXene, the SAPs swelled due to the absorption of water molecules and suspended MXene. After reaching equilibrium, the SAPs were transferred into ethanol, causing rapid deswelling of the SAP network and the removal of water molecules. However, the MXene remained trapped inside the gel network, likely due to physical entanglement within the macromolecular networks and hydrogen-bonding interactions between the polymer chains and the surface of the MXene sheets. Repeating this process led to an increase in the MXene content of the SAPs.

Figure 6-2c shows the total water uptake per gram of SAPs after different BI-BO cycles. The results indicate that each gram of SAPs absorbed approximately 135 mL of the solution. The number of cycles did not significantly affect the water uptake of the SAPs. This consistent water uptake may be attributed to the fact that doping MXene did not alter the chemical structure and flexibility of the polymer. As a result, it can swell to the same state in subsequent cycles.

Figure 6-2d illustrates the quantity of released MXene into deionized water after one hour. The results indicated a low amount of MXene release into deionized water. It could be originating from two sources: MXene attached to particle surfaces and MXene within the SAPs that are not strongly bonded to the polymer structure. This limited release could be attributed to the effective incorporation of MXene into the SAP network [146]. The MXene release stayed constant by increasing BI-BO cycles. It may be attributed to the deswelling process occurring during each BO cycle, which partially cleanses the surface of the particles. Across different BI-BO cycles, the

released amount of MXene did not exceed 370 µg per gram of SAPs, which is below levels associated with observed biocompatibility in literature.

Extensive studies consistently highlight a significant level of biocompatibility when assessing the impact of MXene on various cell cultures and organisms [146-148]. In vitro assessments of MXene (quantum dots) revealed no toxic effects, even at elevated concentrations [149]. Ecotoxicological assessments using a zebrafish embryo model indicated minimal adverse effects at concentrations up to 100 µg/mL [150].

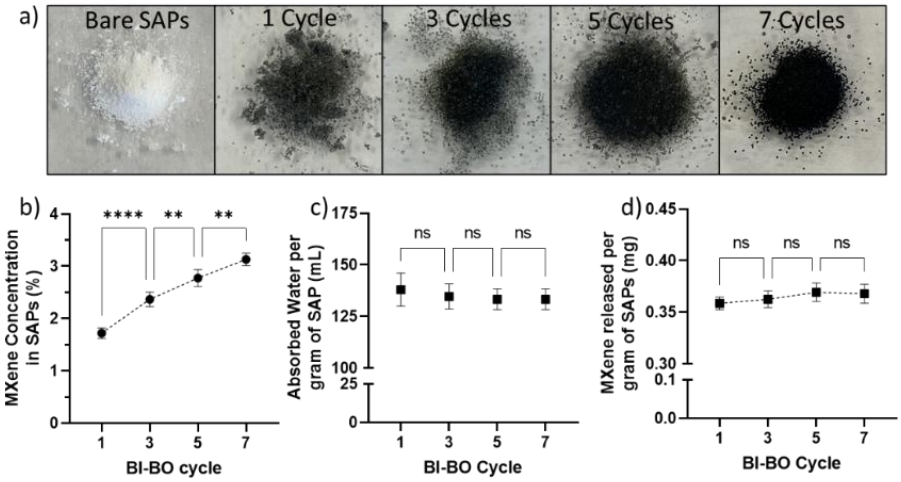

Figure 6-2. a) SAPs after different BI-BO cycles, d) MXene released from the SAPs in DI water per gram of SAPs

Figure 6-3 presents the SEM images of SAPs subjected to varying cycles of BI-BO doping with MXene. Initially, the surface of the SAPs before MXene doping appeared smooth, with no discernible features. This smoothness indicates the absence of any surface modifications or particulate deposits. However, after three BI-BO doping cycles with MXene, the surface morphology of the SAPs underwent a noticeable transformation, becoming rough and irregular. This roughness is attributed to the successful deposition of MXene sheets onto the SAP surface. The images revealed uniform dispersion of MXene sheets within the SAP matrix, with observable changes in the surface roughness as BIBO cycles increased. Furthermore, increasing the number

of BI-BO doping cycles resulted in an increase in the density of MXene sheets on the SAP surface. These results are consistent with the findings of previous studies, which have demonstrated that multiple doping cycles enhance the loading of MXene onto various substrates [106].

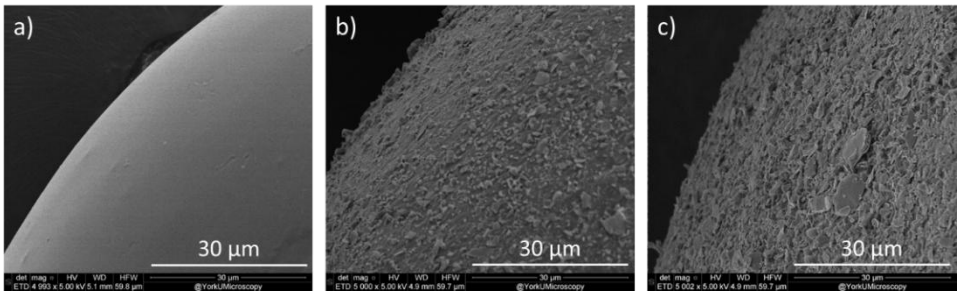

Figure 6-3. SEM images of SAPs before (a), after 3 cycles (b), and after 7 cycles (c) of BI-BO doping MXene

Figure 6-4b shows the FTIR spectrum of AA, Aam, SAPs, and MXene/SAPs. The analysis revealed significant differences in the FTIR spectra of AA and Aam monomers compared to the synthesized SAP and the MXene/SAPs nanocomposite, signifying successful co-polymerization and nanocomposite formation. Notably, the peak at 980 cm^{-1}, attributed to C=C bending vibrations in both AA and Aam, was absent in the SAP-MPs, indicating polymerization. Furthermore, a peak at 1161 cm^{-1} in the SAP-MPs, denoting a C-C stretch, confirmed the co-polymer's formation. Shifts in the peaks for C-H and O-H vibrations to 2930 cm^{-1} and 3421 cm^{-1}, respectively, in the SAP, suggest changes in the electronic environments of these functional groups.

The MXene/SAPs exhibited additional spectral changes, including variations in peak intensities and shifts in peak positions. The peak at around 1710 cm^{-1} was shifted and its intensity decreased, likely due to interactions between the carboxyl groups of acrylic acid and the surface functional groups on MXene. Similarly, the shift and decrease in the peak at 1660 cm^{-1} could be attributed to interactions between the amide groups and the MXene surface. In the spectra of the MXene/SAPs, a new absorption peak at 814 cm^{-1}, corresponding to the Ti–O stretching vibration and terminal functional groups, emerged, confirming the successful incorporation of AA/Aam into the MXene.

Additionally, the shift in peak position from 2930 cm^{-1} in the SAP to 2915 cm^{-1} in the MXene/SAPs implies the formation of hydrogen bonds between AA/Aam and the terminal functional groups of MXene. The characteristic peak at 3421 cm^{-1} shifted towards lower wavenumbers, becoming broader and weaker at 3259 cm^{-1}, further indicating interactions between the MXene and the AA/Aam functional groups. These changes suggest the presence of hydrogen bonding interactions between the MXene and the AA/Aam components.

TGA was used to assess the thermal stability and compositional changes in MXene/SAP nanocomposites, as well as to determine the MXene content. As depicted in Figure 6-4c, the TGA curves of different samples show different stages. Initial weight loss below 100°C, mainly due to water evaporation indicating the hydrophilic nature of the composites. The most significant degradation stage, observed between 200-500°C with a weight loss of 65%, is attributed to the successive cleavage of the polymeric hydrogel backbone, primarily involving the breakdown of C-O and C-C bonds. The decomposition of carboxyl groups from AA and amide groups from AM happened within the temperature range of 340°C–500°C [132]. Beyond 550°C, the weight loss stabilized, highlighting the robust thermal stability of the hydrogel samples [133]. The incorporation of MXene into the SAP matrix enhanced this thermal stability, likely due to the thermal conductivity and barrier effect of MXene. MXene content, expressed as a weight percentage, was derived from the TGA results, with the residual mass at temperatures above 450°C correlating to the MXene content in the SAPs. The specific MXene contents in the samples, namely SAP, MXSAP/3, and MX/SAP7, are quantified as 0%, 2.4%, and 3% by weight, respectively.

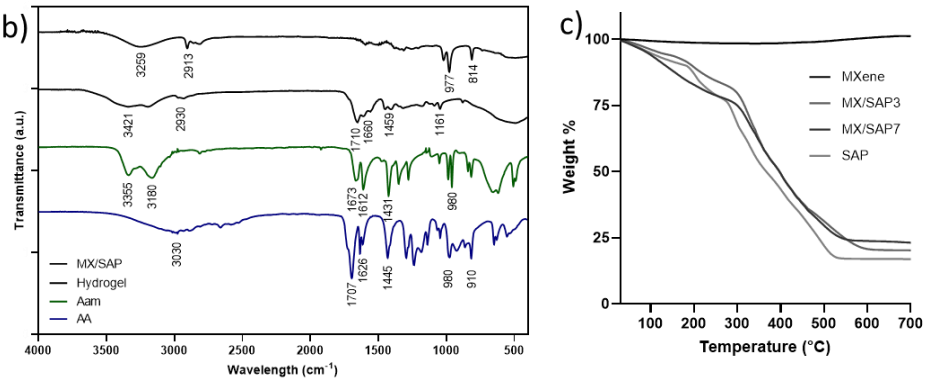

Figure 6-4. b) FTIR spectrum of AA, Aam, AA/Aam, and MXene/SAPs, c) TGA curves of samples with different concentration of MXene

6.2.2 Swelling Behavior Analysis

Figure 6-5a illustrates the dynamic swelling behavior of various samples. In all cases, the VSR initially increased rapidly, followed by a slower rate of increase, eventually reaching a plateau, which represents the VSReq. Figure 6-5b and 6c show the VSR_{eq} and SR of the particles with different MXene concentrations (0, 1, 3, 7 cycles), respectively.

The VSR_{eq} and SR of the SAPs did not significantly change when the MXene content was increased up to 5%, remaining around 115 m^3/m^3 and 1.2 $m^3/m^3 \cdot s$ for VSR_{eq} and SR, respectively. This stability can be attributed to the hydrophilic nature of MXene, which does not decrease the water absorption capacity of the composite. However, with a further increase in MXene concentration to 7%, the VSR_{eq} and SR decreased to 90 m^3/m^3 and 0.8 $m^3/m^3 \cdot s$, respectively.

This reduction could be due to several factors. First, an excess of MXene might cause agglomeration, reducing the effective surface area available for water interaction. Second, high MXene concentrations could lead to overcrowding within the polymer matrix, limiting the available space for water absorption. Finally, a high MXene content might alter the network structure of the SAP, potentially acting as a crosslinker, decreasing its flexibility and thereby reducing water absorption.

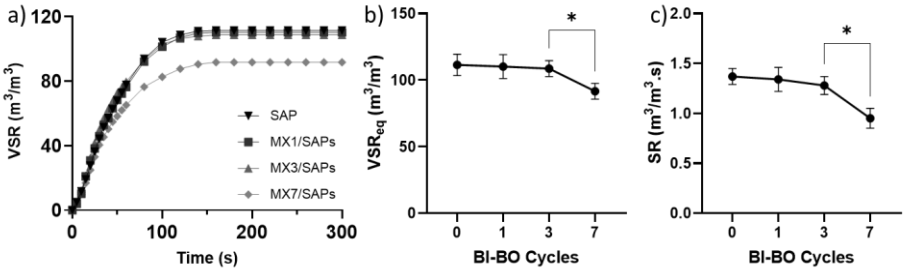

Figure 6-5. a) dynamic swelling, b) VSR_{eq}, and c) SR, d) SR of MXene/SAPs with different BI-BO cycles

6.2.3 Bacteria Enrichment Test

First, the effects of Cr, AA, and particle size on the bacterial enrichment of SAPs were investigated. After the optimization of these parameters, the effect of MXene concentration was examined. Finally, the effects of initial bacterial concentration, initial sample volume, and the number of enrichment steps were assessed. The initial bacterial concentration, solution volume, and SAP concentration were kept constant at 10^3 CFU/mL, 10 mL, and 10 mg/mL, respectively, and the enrichment process was conducted in a single step, unless otherwise mentioned.

6.2.3.1 Effect of Cr

As shown in Figure 6-6a, the CD decreased significantly with increasing Cr levels. When Cr was increased from 0.2% to 2.0%, the CD decreased from approximately 3.3 to 1.6. This reduction in CD is attributed to the higher crosslinking density, which restricts the swelling of the polymer network and limits its ability to absorb water [25].

Figure 6-6b shows the effect of Cr on the EF of the SAPs showing a decrease by increasing the Cr. At a Cr of 0.2%, the EF was 2.2, indicating a strong increase in bacterial concentration. As Cr increased to 1.13% and 2.0%, the EF dropped to 1.8 and 1.5, respectively. This decrease in EF can be explained by the reduced water absorption at higher Cr levels, which limits the ability of SAPs for bacteria enrichment. In general, the lower the water absorption, the lower the EF.

Figure 6-6c presents the RE of SAPs for different levels of Cr. At 0.2% Cr, the RE was 60%. As

Cr increased to 1.13% and 2.0%, the RE improved significantly to 90%. The lower RE at 0.2% Cr, that means more bacteria loose, could be due to the smaller volume of the remaining solution. The decrease in RE was probably caused by more *E. coli* attaching to the surface of the SAPs. When the volume of the remaining water dropped to a certain level that is not sufficient to suspend the swollen SAPs, the mixing condition of the system became very poor. Thus, local regions could be almost dry, forcing *E. coli* to stick on the surface of the beads. Additionally, the higher SR and larger pore sizes at lower Cr level may have facilitated easier bacterial adhesion. In contrast, while higher Cr levels reduced water absorption, the smaller pore sizes likely minimized bacterial loss, leading to higher RE values.

These results highlight the interplay between CD, EF, and RE in SAPs. The optimize Cr would be the trade-off between CD and RE. According to the preliminary results, keeping the CD about 2 should maintain a high recovery efficiency (~90%).

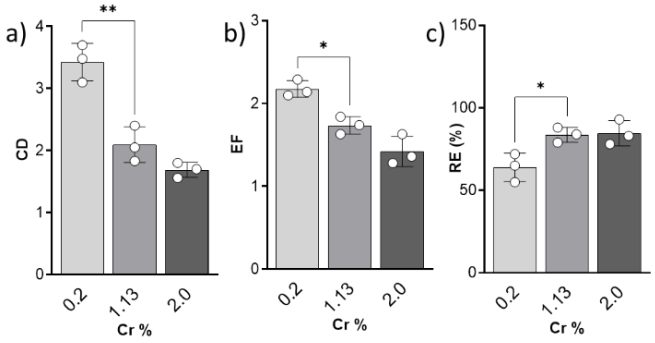

Figure 6-6. Effect of Cr on SAP performance: a) CD, b) EF, and c) RE.

6.2.3.2 Effect of AA

Figure 6-7a shows the effect of AA concentration on the CD of SAPs. Increasing the AA content from 10% to 50% resulted in a slight increase in CD, from approximately 1.6 to 2.2. This increase in CD can be attributed to the higher presence of carboxylic functional groups at elevated AA levels, which enhance water absorption [25].

Figure 6-7b shows the EF of SAPs with varying AA content. At 10% AA, the EF was 1.4. With an increase in AA to 30% and 50%, the EF rose to approximately 1.7 and 1.9, respectively. This trend likely results from the improved water absorption capacity of SAPs at higher AA concentrations [25].

Figure 6-7c presents the RE of SAPs across different AA levels. The RE increased modestly from 82% to 85% as the AA concentration rose. The lower RE observed at 10% AA may be attributed to a reduced presence of charged functional groups in the SAPs, which could facilitate bacterial adhesion to the SAP surfaces. In contrast, the higher RE observed at 30% and 50% AA is likely due to the increased density of charged functional groups, which repelled bacteria and minimized bacterial loss.

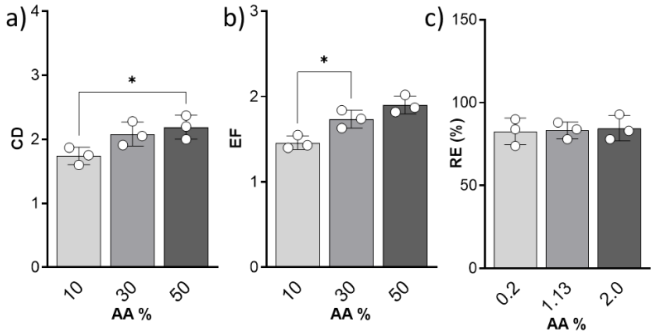

Figure 6-7. Effect of AA on SAP performance: a) CD, b) EF, and c) RE.

6.2.3.3 Effect of Particle Size

Figure 6-8a demonstrates the effect of particle size on the CD. The results indicate that CD decreases from 2.7 to 1.6 as particle size increases from 90 µm to 270 µm. This inverse relationship between particle size and water absorption aligns well with previous experiments conducted using the microfluidic system [25].

Figure 6-8b presents the EF of SAPs across different particle sizes. As particle size increased from

90 µm to 270 µm, the EF declined slightly from 1.8 to 1.5. This reduction in EF can likely be attributed to the lower water absorption capacity of SAPs with larger particle sizes [25].

As shown in Figure 6-8c, the RE of SAPs increased from 65% to 83% as the particle size rose from 90 µm to 140 µm, with a further increase to 91% at 270 µm. While CD was highest for smaller particle sizes, these smaller particles have a relatively larger surface area, which increases the likelihood of bacterial adhesion and thus lowers the RE. In contrast, the higher RE observed with larger particle sizes could be due to their reduced surface area, which minimizes bacterial adhesion.

Based on these findings, the optimal SAP conditions for achieving high EF and RE were identified as 1.13% Cr, 50% AA, and a particle size of 140 µm. This optimized chemical composition and particle size were used in all subsequent experiments.

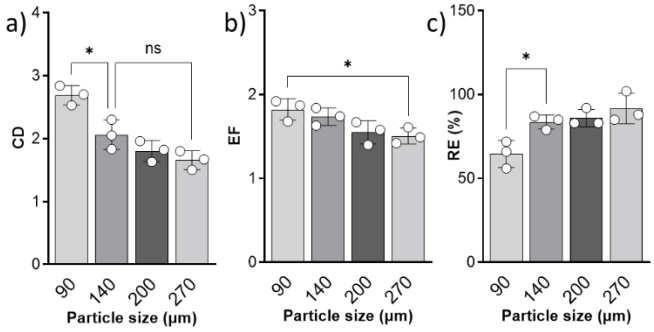

Figure 6-8. Effect of particle size on SAP performance: a) CD, b) EF, and c) RE.

6.2.3.4 Effect of MXene

Figure 6-9a illustrates the effect of MXene on CD, showing that increasing the MXene content did not significantly impact CD. This finding aligns with swelling characterization results for both SAPs and MXene/SAPs, confirming that MXene addition did not reduce the water absorption capacity of the SAPs.

Figure 6-9b presents the EF of SAPs with different levels of MXene. Adding MXene at 1%

increased the EF from 1.6 to approximately 1.9, which can be attributed to the higher surface charge due to additional functional groups (-F, -OH, and =O) from MXene, enhancing bacterial repulsion. However, further increases in MXene to 2% and 3% did not significantly change the EF.

Figure 6-9c depicts the RE of SAPs at varying MXene levels. The initial addition of MXene at 1% led to a notable increase in RE from 70% to 93%, likely due to the higher concentration of negatively charged functional groups, which enhanced bacterial repulsion from the SAPs. Further increases in MXene to 2% and 3% did not significantly impact RE, maintaining it around 93%.

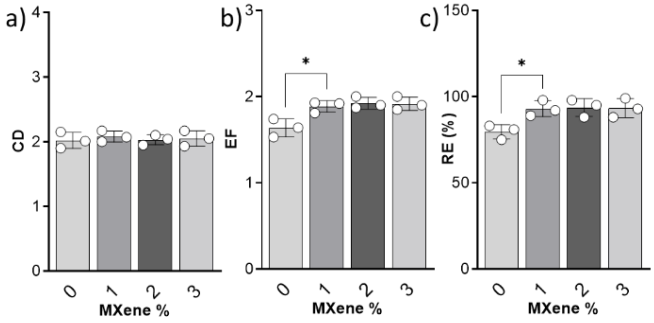

Figure 6-9. Effect of MXene concentration on SAP performance: a) CD, b) EF, and c) RE.

6.2.3.5 Effect of initial SAP Concentration

Figure 6-10a demonstrates the effect of the initial concentration of SAPs on the CD. An increase in SAPs concentration resulted in a significant rise in CD. Specifically, as the concentration increased from 5 to 15 mg/mL, CD rose from approximately 1.3 to around 4.

Figure 6-10b and c show the effects of SAP concentration on EF and RE, respectively. As SAP concentration increased from 5 to 10 mg/mL, the EF also rose, from about 1.1 to approximately 1.8. However, a further increase to 15 mg/mL did not lead to a substantial change in EF. The initial increase in EF is likely due to the greater availability of SAPs and their enhanced water absorption capacity at higher concentrations.

In contrast, the RE remained relatively stable at approximately 85% as the SAP concentration increased from 5 to 10 mg/mL, but then dropped significantly to 43% at 15 mg/mL. This decline in RE and the lack of further increase in EF at higher SAP concentrations may be due to excessive water absorption and greater bacterial adhesion on the SAP surfaces, as the remaining solution volume may no longer be sufficient to keep the SAPs fully suspended. It could increase the chance of bacterial attachment and adhesion on the SAP surfaces.

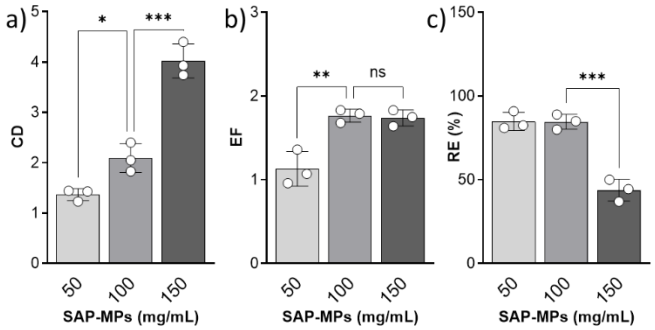

Figure 6-10. Effect of SAP concentration on SAP performance: a) CD, b) EF, and c) RE.

6.2.3.6 Effect of initial Bacteria Concentration

Figure 6-11a illustrates the effect of initial bacteria concentration on the CD. The results indicate that CD is not significantly affected by the initial bacteria concentration, confirming that CD is primarily determined by factors such as SAP concentration, particle size, and chemical composition.

As shown in Figure 6-11b and c, increasing the initial bacteria concentration from ~10^3 to ~10^5 CFU/mL resulted in a slight decrease in EF, from around 2 to 1.7. A further increase to ~10^7 CFU/mL led to a reduction in EF to 1.4. Similarly, the RE of the SAPs declined from around 95% to 65% as the initial bacteria concentration rose from ~10^3 to ~10^7 CFU/mL. This decrease in both RE and EF at higher bacterial concentrations could be attributed to an increased likelihood of bacterial attachment and adhesion on the SAP surfaces, potentially reducing effective recovery.

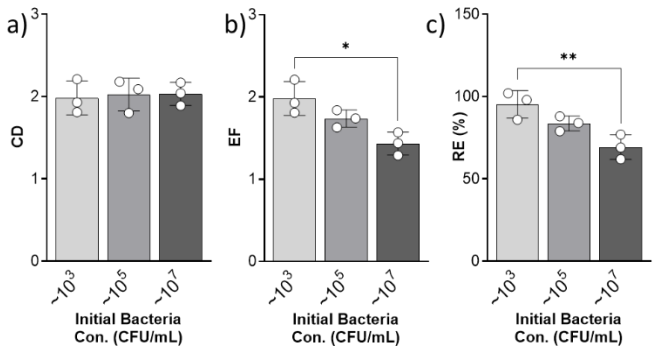

Figure 6-11. Effect of initial bacteria concentration on SAP performance: a) CD, b) EF, and c) RE.

6.2.3.7 Effect of Initial Sample Volume and Enrichment Steps

Figure 6-12a shows that the CD was maintained at approximately 2 for both initial sample volumes of 10 mL and 40 mL, enabling a direct comparison of results. Figure 6-12b and c illustrate the EF and RE at these initial volumes, respectively. The data indicates a slight increase in both EF and RE as the sample volume increased, which can be attributed to the larger residual solution volume at the end of the enrichment process. This residual volume helps to keep the swollen SAPs suspended within the solution and having more space between the particles that reduce the chance of bacteria being trapped, supporting improved enrichment performance.

Figure 6-12d, e, and f present the cumulative CD, EF, and RE across multiple steps of the enrichment process for an initial sample volume of 40 mL and a bacterial concentration of 10^3 CFU/mL. In each step, the CD consistently maintained around 2 (Figure 6-12d). The results show a substantial increase in EF, reaching approximately 10 after the fourth step. However, RE gradually declined to around 62% over the enrichment steps. The decrease in RE across steps may be due to the diminishing remaining water volume, which affects SAP suspension and the gap between them. Additionally, cumulative filtration and washing steps increase the chance of bacterial loss, as they are performed four times over the process.

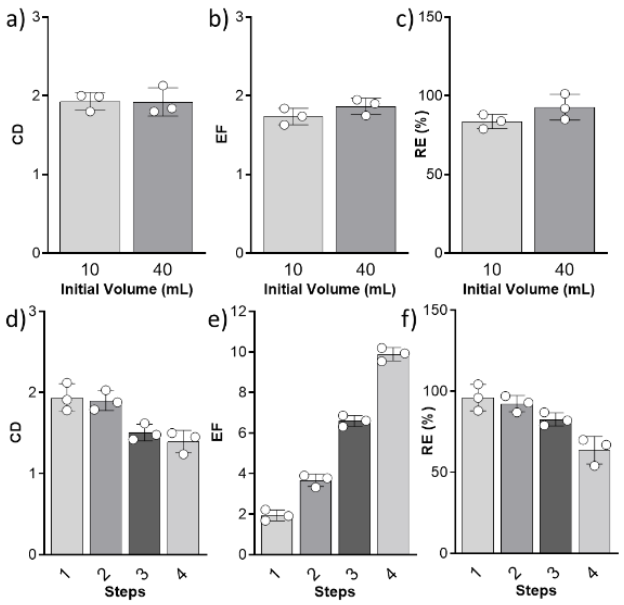

Figure 6-12. Effect of initial sample volume and enrichment steps on SAP performance: a) CD for both 10 mL and 40 mL initial volumes, b) EF, and (c) RE at 10 mL and 40 mL initial sample volumes; d) CD, e) cumulative EF, and f) cumulative RE for a four-step enrichment process with an initial 40 mL sample.

6.3 Conclusion

In this chapter, MXene nanoparticles and MX/SAP-MPs were synthesized using the BI-BO method, and their bacterial enrichment efficiency was investigated. The results indicated that incorporating up to 3% MXene into the SAP-MPs did not significantly affect their swelling behavior. However, exceeding 3% led to a reduction in the VSR_{eq} and SR from 115 m^3/m^3 and 1.2 $m^3/m^3 \cdot s$ to 90 m^3/m^3 and 0.8 $m^3/m^3 \cdot s$, respectively.

Increasing the Cr from 0.2% to 2.0% reduced the EF from 2.2 to 1.5, while the RE increased from 60% to 90%. Similarly, increasing the AA from 10% to 50% improved the EF from 1.5 to 1.8 and increased the RE from 82% to 87%.

In terms of particle size, an increase from 90 µm to 270 µm resulted in a decrease in EF from 1.8 to 1.5, while the RE increased from 66% to 90%. Introducing MXene into the SAP-MPs enhanced the EF from 1.6 to 1.85 and increased the RE from 80% to 90%.

Varying the initial SAP-MP concentration revealed that increasing it from 5 to 10 mg/mL improved the EF from 1.2 to 1.8, but further increasing it to 15 mg/mL caused the EF to decrease to 1.5, with the RE remaining constant at approximately 85% at 10 mg/mL before dropping to around 55% at 15 mg/mL.

The effect of initial bacterial concentration showed that increasing it from 10^3 to 10^7 CFU/mL reduced the EF from 2.0 to 1.5, while the RE decreased from 90% to 65%. Increasing the initial sample volume from 10 mL to 40 mL slightly improved both EF and RE.

Finally, increasing the number of enrichment steps to four led to a significant improvement in the EF, reaching approximately 8, with a RE of around 85%.

The incorporation of MXene into SAP-MPs demonstrated both advantages and challenges. While MXene enhanced the EF and RE within certain concentration ranges, exceeding 3% negatively affected the swelling properties. MXene's high surface area and functional groups contributed to improved bacterial interactions, potentially making the composite more effective for bacterial enrichment applications. Additionally, MXene's conductive properties could allow integration into biosensing platforms. However, concerns regarding MXene's stability, potential cytotoxicity, and long-term environmental impact must be addressed for practical applications. Further studies are needed to optimize MXene doping strategies, evaluate biocompatibility, and explore scalable, cost-effective synthesis approaches for real-world implementation.

Chapter 7

Thesis Summary and Future Directions

7.1 Conclusion

This study successfully addressed the research objectives, contributing significant advancements in the field of SAPs and their application in water analysis. The findings are summarized as follows:

7.1.1 Objective 1: Development of a Microfluidic Platform for SAP-MP Characterization

A novel microfluidic platform was designed and fabricated to enable high-resolution, real-time characterization of SAP microparticles (SAP-MPs). The platform featured an innovative design with integrated channel sets that enhanced particle trapping and fluid exchange efficiency. A

unique fabrication method employing multi-layer molds reduced fabrication complexity, eliminating the need for alignment steps while ensuring reliable and reproducible results.

The platform is capable of effectively trapping single SAP-MPs, allowing precise measurement of swelling kinetics, including VSR and SR. Real-time measurements under dynamic conditions demonstrated a VSR_{eq} of 5.59 ± 0.13 (m^3/m^3) and an SR of 0.039 ± 0.002 ($m^3/m^3 \cdot s$) for AA-Aam (4:1) SAP-MPs, showing excellent repeatability and accuracy. These results validated the platform's capability to provide detailed insights into swelling dynamics, even for small and irregularly shaped SAP-MPs.

7.1.2 Objective 2: Parametric Study of SAP-MP Swelling Behavior

The microfluidic platform enabled a detailed parametric study of the swelling behavior of SAP-MPs, focusing on particle size, crosslinker concentration (Cr), acrylic acid concentration (AA), and neutralization degree (ND). The study confirmed the significance of particle size and composition in influencing swelling dynamics, particularly the role of crosslinking density in balancing water absorption with structural integrity.

By varying Cr from 0.2% to 2.0%, the VSR_{eq} was observed to decrease from 350 m^3/m^3 to 50 m^3/m^3, representing an 85% reduction in swelling. Additionally, particle size significantly impacted the swelling rate, with smaller SAP-MPs (90 μm) exhibiting a higher SR of 10 $m^3/m^3 \cdot s$, compared to larger particles (270 μm) with an SR of 1 $m^3/m^3 \cdot s$. Increasing AA concentration from 10% to 50% improved both the VSR and SR, with a 200% enhancement in VSR and a 180% increase in SR.

These findings advanced the understanding of SAP-MP behavior and provided valuable design guidelines for tailoring SAPs for specific applications.

7.1.3 Objectives 3 and 4: Incorporation of MXene and Bacterial Enrichment

MXene sheets were successfully incorporated into SAP-MPs using the breathing-in-breathing-out (BI-BO) method, creating a nanocomposite for bacterial enrichment applications. The integration of MXene was optimized to ensure uniform dispersion without compromising SAP performance.

Swelling characterization revealed that incorporating MXene up to 3% did not significantly alter the swelling behavior of SAPs, with the VSR remaining at 115 m^3/m^3 and SR at 1.2 $m^3/m^3 \cdot s$. However, at concentrations greater than 3%, the VSR dropped to 90 m^3/m^3 and SR decreased to 0.8 $m^3/m^3 \cdot s$ due to agglomeration of MXene particles.

The bacterial enrichment study systematically investigated the effects of Cr, AA, particle size, MXene content, SAP concentration, initial bacterial concentration, initial sample volume, and multiple enrichment steps. This comprehensive analysis demonstrated that MXene/SAP-MPs achieved a 10-fold improvement in enrichment efficiency (EF) and 90% recovery efficiency (RE), without the need for external equipment, making the process effective, cost-efficient, and scalable, particularly in resource-limited settings.

7.2 Future Directions

Building upon the findings and limitations of this study, several areas for future research and development are proposed for each objective:

7.2.1 Objective 1: Development of a Microfluidic Platform

- **Automation of Particle Loading**: Develop automated systems, such as micro-pipetting or microfluidic valves, to reduce manual intervention and improve experimental repeatability.
- **Increasing the Number of Traps**: Expand the number of particle traps to enhance throughput and statistical reliability in swelling behavior analysis.
- **Design Modifications for Faster Fluid Exchange**: Optimize microfluidic channel

geometry to minimize time differences (T_d) and transition times (T_t), ensuring uniform swelling behavior across traps.

- **Characterization of Deswelling Behavior**: Integrate features to study the deswelling process, supporting applications like drug delivery systems with reversible swelling cycles.
- **Simulation Studies**: Perform simulations for current and future designs to validate experimental data and optimize device configurations.

7.2.2 Objective 2: Parametric Study of SAP-MP Swelling Behavior

- **Exploration of Diverse Monomers**: Investigate the effects of alternative monomers, such as itaconic acid, to develop SAPs with tailored properties for specific applications.
- **Analysis of Sub-50 µm SAP-MPs**: Study smaller particle sizes to uncover size-dependent swelling characteristics for applications like environmental sensing and drug delivery.
- **Impact of External Fields**: Examine the influence of electric and magnetic fields during swelling/deswelling for potential use in smart materials.
- **Temperature-Responsive Studies**: Investigate thermo-responsive SAPs for applications in biomedical and environmental remediation systems.
- **Real-Time Drug Release Investigations**: Integrate drugs into SAP-MPs and monitor release dynamics to explore controlled drug delivery systems.

7.2.3 Objectives 3 and 4: Incorporation of MXene and Bacterial Enrichment

- **Optimization of MXene Doping**: Refine doping cycles and explore alternative incorporation methods, such as in-situ polymerization, to enhance MXene dispersion and stability.
- **Alternative Nanomaterials**: Investigate the incorporation of graphene oxide, carbon nanotubes, or silica nanoparticles to add functionalities like antimicrobial properties or biocompatibility.
- **Integration into Detection Platforms**: Combine MXene/SAP composites with biosensors or microfluidic devices for real-time bacterial detection.
- **Application Expansion**: Test bacterial enrichment methods on diverse strains and environmental samples, such as industrial wastewater or natural water sources.

- **Scale-Up and Field Tests**: Develop scalable synthesis methods and validate performance in real-world scenarios to assess feasibility for large-scale applications.
- **Reusability Studies**: Examine the potential for reusing MXene/SAP composites across multiple cycles to improve cost-efficiency.
- **Sustainability Assessments**: Evaluate the environmental impact of the synthesis and application of MXene/SAPs, exploring green synthesis methods and biodegradable alternatives.
- **Bacterial Diversity Testing**: Assess the efficiency of SAPs in enriching different bacterial types, including Gram-positive bacteria, and evaluate performance using real environmental samples.

Chapter 8

Contributions

This thesis presents significant advancements in the synthesis, characterization, and application of superabsorbent polymer microparticles (SAP-MPs) and their nanocomposites for water analysis. The work contributes to both fundamental understanding and practical applications of SAP-MPs, with specific emphasis on real-time swelling behavior characterization and bacterial enrichment using MXene/SAPs. Below, the key contributions are outlined:

8.1 Fundamental Contributions

1. **Development of a Novel Microfluidic Platform**:
    - Designed and fabricated an innovative microfluidic device, enabling precise trapping

of SAP-MPs and real-time observation of swelling behavior.

- Introduced a fabrication method using double molds that eliminates alignment steps, improving the efficiency and reproducibility of device manufacturing.
- Demonstrated the device's capability to provide high-resolution, real-time swelling data, including VSR_{eq} and SR, under controlled environmental conditions.

2. **Advanced Understanding of Swelling Dynamics**:

    - Provided accurate single-particle characterization of SAP-MPs, removing confounding factors such as trapped interstitial water that affect bulk analysis.
    - Investigated the effects of key parameters, including particle size, crosslinker concentration (Cr), acrylic acid (AA) content, and neutralization degree (ND), on swelling behavior.
    - Resolved conflicting results in the literature by demonstrating that smaller SAP-MPs achieve higher VSR_{eq} and SR, attributed to their larger surface-to-volume ratio.

3. **Introduction of MXene/SAP Nanocomposites**:

    - Synthesized MXene nanoparticles and successfully incorporated them into SAP-MPs using the breathing-in-breathing-out (BI-BO) method.
    - Established that MXene content up to 3% does not negatively affect the swelling behavior of SAP-MPs, maintaining VSR and SR at optimal levels.
    - Investigated the interactions between MXene and SAP functional groups, revealing insights into their compatibility and stability within the polymer network.

8.2 Applied Contributions

1. **Enhanced Bacterial Enrichment Methods**:
    - Evaluated the bacterial enrichment efficiency of SAP-MPs and MXene/SAP-MPs under various conditions, such as Cr, AA content, particle size, MXene concentration, SAP concentration, and initial bacterial concentration.
    - Demonstrated the feasibility of SAP-based bacterial enrichment without requiring sophisticated external equipment, highlighting their potential for portable water analysis applications.
    - Achieved enrichment factors (EF) of up to 8 and recovery efficiencies (RE) of around 85% through optimized enrichment steps and SAP-MP design.
2. **Parametric Optimization for Real-World Applications**:
    - Identified optimal SAP-MP properties for bacterial enrichment, including 1.13% Cr, 50% AA, and particle sizes around 140 μm, providing a blueprint for tailoring SAPs to specific applications.
3. **Foundational Work for Portable Detection Systems**:
    - Laid the groundwork for integrating MXene/SAP nanocomposites into biosensors or microfluidic systems for real-time bacterial detection, enabling their use in point-of-care diagnostics and environmental monitoring.

8.3 Publications, Conferences, and Awards

8.3.1 Publications

The research presented in this thesis has resulted in several high-impact publications that

contribute to advancing knowledge in the fields of SAP characterization, MXene composites, and water treatment:

1. Tabesh E., Leung E., Rezai E., "A Microfluidic-Based In-situ Investigation of Swelling Dynamics of Superabsorbent Polymer Microparticles," *Materials Today Communications*, 2023.
2. Tabesh E., Zabihihesari A., Rezai P., Leung S., "In-Situ Investigation of Swelling Dynamics of Acrylamide-Acrylic Acid Superabsorbent Microparticles (SAP-MPs) at a Single Particle Level," *Macromolecular Rapid Communications, 2025*.
3. Abie N., Ünlü C., Pinho A.R., Gomes M.C., Remmler T., Herb M., Grumme D., Tabesh E., et al., "Designing of a Multifunctional 3D-Printed Biomimetic Theragenerative Aerogel Scaffold via Mussel-Inspired Chemistry," *ACS Applied Materials & Interfaces*, 2024.
4. Doostmohammadi A., Youssef K., Akhtarian S., Tabesh E., Kraft G., Brar S.K., Rezai P., "Molecularly Imprinted Polymer (MIP) Based Core-Shell Microspheres for Bacteria Isolation," *Polymer*, 2022.
5. Tabesh E., Rezai P., Herb M., Maleki H., Leung S., "MXene/superabsorbent polymer composites for bacterial enrichment" *(Under process)*.

8.3.2 Presentations

Key findings from this research have been disseminated through oral and poster presentations at international and national conferences:

1. Tabesh E., Leung S., Rezai P., "Fabrication of Monodispersed Acrylamide/Acrylic Acid Superabsorbent Polymer Microparticles Using Droplet Microfluidics and In-Situ Thermal Polymerization," *CSME, Sherbrooke, QC, Canada, 2023*.

2. Tabesh E., Brown J., Zabihihesari A., Leung S., Rezai P., “A Droplet Microfluidic Device for Rapid In-Situ Polymerization of Superabsorbent Polymer Microparticles (SAP-MPs),” *μTAS, Katowice, Poland, 2023*.
3. Tabesh E., Leung S., Rezai P., “Microfluidic-Based Time Lapse Characterization of Water Uptake in Superabsorbent Polymer Particles,” *2nd Conference on Micro Flow and Interfacial Phenomena (μFIP), Irvine, California, 2022*.
4. Brown J., Zabihihesari A., Tabesh E., Rezai P., “Microfluidic Droplet-Based Polymerization of Imprinted Polymers for Biological Applications,” *μTAS, RN#0168, 2024*.

8.3.3 Awards and Recognitions

1. Mitacs Globalink Award: Recognized for research excellence, enabling collaboration with the Department of Inorganic Chemistry, Cologne University, Germany on bacteria enrichment and MXene-related studies.
2. Academic Excellence Fund: Awarded consecutively for three years (2021–2024) for outstanding academic and research contributions.
3. Best Presentation Award: Received for an oral presentation in the Mechanical Engineering Department's presentation series.

8.3.4 Collaborations

A significant international collaboration was established with Dr. Maleki and Herb at Cologne University, Germany, focusing on bacterial enrichment and MXene applications. This collaboration has broadened the scope of the thesis and enabled the exploration of interdisciplinary approaches in environmental sensing and material science.

8.3.5 Mentorship and Supervision

Successfully mentored and supervised one bachelor's student and one master's student during this research. Both mentees made substantial contributions to SAP synthesis while gaining hands-on experience in microfluidic device fabrication and characterization techniques.

References

1. Buchholz, F.L. and A.T. Graham, *Modern superabsorbent polymer technology*. Vol. 152. 1998: Wiley-vch New York.
2. Zohuriaan-Mehr, M. and K. Kabiri, *Superabsorbent polymer materials: a review.* 2008.
3. Schröfl, C., et al., *Recent progress in superabsorbent polymers for concrete.* Cement and Concrete Research, 2022. **151**: p. 106648.
4. Behera, S. and P.A. Mahanwar, *Superabsorbent polymers in agriculture and other applications: a review.* Polymer-Plastics Technology and Materials, 2020. **59**(4): p. 341-356.
5. Oladosu, Y., et al., *Superabsorbent polymer hydrogels for sustainable agriculture: A review.* Horticulturae, 2022. **8**(7): p. 605.
6. Zhang, Y., et al., *An automated bacterial concentration and recovery system for pre-enrichment required in rapid Escherichia coli detection.* Scientific reports, 2018. **8**(1): p. 1-8.
7. Xie, X., et al., *"Nanofiltration" enabled by super-absorbent polymer beads for concentrating microorganisms in water samples.* Scientific reports, 2016. **6**: p. 20516.
8. Gawande, N. and A.A. Mungray, *Superabsorbent polymer (SAP) hydrogels for protein enrichment.* Separation and Purification Technology, 2015. **150**: p. 86-94.
9. Wu, X., et al., *Synthesis and application of superabsorbent polymer microspheres for rapid concentration and quantification of microbial pathogens in ambient water.* Separation and purification technology, 2020. **239**: p. 116540.
10. Yang, H.C., et al., *Single-step equipment-free extracellular vesicle concentration using super absorbent polymer beads.* Journal of Extracellular Vesicles, 2021. **10**(4): p. e12074.
11. Ostrand, M.S., et al., *Superabsorbent polymer characteristics, properties, and applications.* Agrosystems, Geosciences & Environment, 2020. **3**(1): p. e20074.
12. Esteves, L.P., *Superabsorbent polymers: On their interaction with water and pore fluid.* Cement and concrete composites, 2011. **33**(7): p. 717-724.
13. Omidian, H., et al., *Modified acrylic-based superabsorbent polymers (dependence on particle size and salinity).* Polymer, 1999. **40**(7): p. 1753-1761.
14. Tabesh, E., S.N. Leung, and P. Rezai, *A microfluidic-based In-situ investigation of swelling dynamics of superabsorbent polymer microparticles.* Materials Today Communications, 2023. **35**: p. 106369.
15. Oon, Y.-L., et al., *Waterborne pathogens detection technologies: advances, challenges, and future perspectives.* Frontiers in Microbiology, 2023. **14**: p. 1286923.
16. Zhang, Y.-Z., et al., *MXene hydrogels: fundamentals and applications.* Chemical Society Reviews, 2020. **49**(20): p. 7229-7251.
17. Damiri, F., et al., *MXene (Ti3C2Tx)-embedded nanocomposite hydrogels for biomedical applications: a review.* Materials, 2022. **15**(5): p. 1666.
18. Zaed, M.A., et al., *Cost analysis of MXene for low-cost production, and pinpointing of its economic footprint.* Open Ceramics, 2024. **17**: p. 100526.
19. Cao, F., et al., *Recent advances in oxidation stable chemistry of 2D MXenes.* Advanced Materials, 2022. **34**(13): p. 2107554.

20. Ghanbari, R. and E.N. Zare, *Engineered MXene-polymer composites for water remediation: promises, challenges and future perspective.* Coordination Chemistry Reviews, 2024. **518**: p. 216089.
21. Zhang, Z.-H., J.-Y. Xu, and X.-L. Yang, *MXene/sodium alginate gel beads for adsorption of methylene blue.* Materials Chemistry and Physics, 2021. **260**: p. 124123.
22. Dong, Y., et al., *Mxene/alginate composites for lead and copper ion removal from aqueous solutions.* RSC advances, 2019. **9**(50): p. 29015-29022.
23. Hao, C., et al., *Preparation of acrylic acid modified alkalized MXene adsorbent and study on its dye adsorption performance.* Colloids and Surfaces A: Physicochemical and Engineering Aspects, 2022. **632**: p. 127730.
24. Shahzad, A., et al., *Ti3C2Tx MXene core-shell spheres for ultrahigh removal of mercuric ions.* Chemical Engineering Journal, 2019. **368**: p. 400-408.
25. Tabesh, E., et al., *In-Situ Investigation of Swelling Dynamics of Acrylamide-Acrylic Acid Superabsorbent Microparticles (SAP-MPs) at a Single Particle Level (Unpublished manuscript), Mechanical Engineering Department, York University.* Macromolecular Rapid Communications, 2025. **Under Review**.
26. Tabesh, E., et al., *Fabrication of MXene Integrated Superabsorbent Polymers Composites Hydrogels for Bacterial Enrichment.* Under Process, 2025.
27. Ahmed, E.M., *Hydrogel: Preparation, characterization, and applications: A review.* Journal of advanced research, 2015. **6**(2): p. 105-121.
28. Ullah, F., et al., *Classification, processing and application of hydrogels: A review.* Materials Science and Engineering: C, 2015. **57**: p. 414-433.
29. Zohuriaan-Mehr, M., et al., *Advances in non-hygienic applications of superabsorbent hydrogel materials.* Journal of materials science, 2010. **45**(21): p. 5711-5735.
30. Mignon, A., et al., *Superabsorbent polymers: A review on the characteristics and applications of synthetic, polysaccharide-based, semi-synthetic and 'smart'derivatives.* European Polymer Journal, 2019.
31. Wichterle, O. and D. Lim, *Hydrophilic gels for biological use.* Nature, 1960. **185**(4706): p. 117-118.
32. Venkatachalam, D. and S. Kaliappa, *Superabsorbent polymers: A state-of-art review on their classification, synthesis, physicochemical properties, and applications.* Reviews in Chemical Engineering, 2023. **39**(1): p. 127-171.
33. Reyes, Z., et al., *Continuous production of acrylonitrile-starch graft copolymers by ceric ion catalysis.* Industrial & Engineering Chemistry Process Design and Development, 1973. **12**(1): p. 62-67.
34. Masuda, F., *Trends in the development of superabsorbent polymers for diapers*. 1994, ACS Publications.
35. Staples, T.L. and P.K. Chatterjee, *Synthetic superabsorbents*, in *Textile science and technology*. 2002, Elsevier. p. 283-322.
36. Wang, A. and W. Wang, *Superabsorbent materials.* Kirk-Othmer encyclopedia of chemical technology, 2000: p. 1-34.
37. Laftah, W.A., S. Hashim, and A.N. Ibrahim, *Polymer hydrogels: A review.* Polymer-Plastics Technology and Engineering, 2011. **50**(14): p. 1475-1486.
38. Hoffman, J., *Theoretical aspects of polymer crystallization with chain folds: bulk polymers.* Polymer Engineering & Science, 1964. **4**(4): p. 315-362.

39. Ma, X. and G. Wen, *Development history and synthesis of super-absorbent polymers: a review.* Journal of Polymer Research, 2020. **27**(6): p. 136.
40. Carmo, I.A.D., et al., *Experimental planning applied to the synthesis of superabsorbent polymer by acrylic acid graft in pectin extracted from passion fruit peel.* Materials Research Express, 2019. **6**(9): p. 095328.
41. Pakdel, P.M. and S.J. Peighambardoust, *A review on acrylic based hydrogels and their applications in wastewater treatment.* Journal of environmental management, 2018. **217**: p. 123-143.
42. Chaudhary, V. and S. Sharma, *Suspension polymerization technique: parameters affecting polymer properties and application in oxidation reactions.* Journal of Polymer Research, 2019. **26**(5): p. 102.
43. Arshady, R., *Suspension, emulsion, and dispersion polymerization: A methodological survey.* Colloid and polymer science, 1992. **270**: p. 717-732.
44. Gilbert, R.G., *Emulsion polymerization: a mechanistic approach*. 1995: Academic press.
45. Chern, C.-S., *Principles and applications of emulsion polymerization*. 2008: John Wiley & Sons.
46. Cheng, D., et al., *Water-and fertilizer-integrated hydrogel derived from the polymerization of acrylic acid and urea as a slow-release N fertilizer and water retention in agriculture.* Journal of agricultural and food chemistry, 2018. **66**(23): p. 5762-5769.
47. Qureshi, D., et al., *Environment sensitive hydrogels for drug delivery applications.* European Polymer Journal, 2019. **120**: p. 109220.
48. Spicer, C.D., *Hydrogel scaffolds for tissue engineering: the importance of polymer choice.* Polymer Chemistry, 2020. **11**(2): p. 184-219.
49. Ramli, R.A., *Slow release fertilizer hydrogels: a review.* Polymer Chemistry, 2019. **10**(45): p. 6073-6090.
50. Shalla, A.H., M.A. Bhat, and Z. Yaseen, *Hydrogels for removal of recalcitrant organic dyes: A conceptual overview.* Journal of environmental chemical engineering, 2018. **6**(5): p. 5938-5949.
51. Flory, P.J., *Principles of polymer chemistry*. 1953: Cornell university press.
52. Tang, Q., et al., *Superabsorbent conducting hydrogel from poly (acrylamide-aniline) with thermo-sensitivity and release properties.* Carbohydrate polymers, 2008. **73**(3): p. 473-481.
53. Kim, S.J., et al., *Electrical sensitive behavior of poly (vinyl alcohol)/poly (diallyldimethylammonium chloride) IPN hydrogel.* Sensors and Actuators B: Chemical, 2003. **88**(3): p. 286-291.
54. Xiong, Z., et al., *Preparation and properties of thermo-sensitive hydrogels of konjac glucomannan grafted N-isopropylacrylamide for controlled drug delivery.* 2007.
55. Green, T.K., J. Kovac, and J.W. Larsen, *A rapid and convenient method for measuring the swelling of coals by solvents.* Fuel, 1984. **63**(7): p. 935-938.
56. Hamidi, M., A. Azadi, and P. Rafiei, *Hydrogel nanoparticles in drug delivery.* Advanced drug delivery reviews, 2008. **60**(15): p. 1638-1649.
57. Chun, C., et al., *Thermosensitive poly (organophosphazene)–paclitaxel conjugate gels for antitumor applications.* Biomaterials, 2009. **30**(12): p. 2349-2360.
58. He, H., *Multifunctional medical devices based on pH-sensitive hydrogels for controlled drug delivery*. 2006: The Ohio State University.
59. Wu, J., et al., *Study on starch-graft-acrylamide/mineral powder superabsorbent composite.*

Polymer, 2003. **44**(21): p. 6513-6520.
60. Peppas, N.A., et al., *Hydrogels in pharmaceutical formulations.* European journal of pharmaceutics and biopharmaceutics, 2000. **50**(1): p. 27-46.
61. Athawale, V.D. and V. Lele, *Factors influencing absorbent properties of saponified starch-g-(acrylic acid-co-acrylamide).* Journal of applied polymer science, 2000. **77**(11): p. 2480-2485.
62. Chen, Y. and H.-m. Tan, *Crosslinked carboxymethylchitosan-g-poly (acrylic acid) copolymer as a novel superabsorbent polymer.* Carbohydrate Research, 2006. **341**(7): p. 887-896.
63. Xie, J., et al., *Swelling properties of superabsorbent poly (acrylic acid-co-acrylamide) with different crosslinkers.* Journal of applied polymer science, 2009. **112**(2): p. 602-608.
64. Adibnia, V. and R.J. Hill, *Universal aspects of hydrogel gelation kinetics, percolation and viscoelasticity from PA-hydrogel rheology.* Journal of Rheology, 2016. **60**(4): p. 541-548.
65. Chen, X.P., et al., *Synthesis and properties of acrylic-based superabsorbent.* Journal of applied polymer science, 2004. **92**(1): p. 619-624.
66. Pourjavadi, A., A. Harzandi, and H. Hosseinzadeh, *Modified carrageenan 3. Synthesis of a novel polysaccharide-based superabsorbent hydrogel via graft copolymerization of acrylic acid onto kappa-carrageenan in air.* European Polymer Journal, 2004. **40**(7): p. 1363-1370.
67. Liang, R. and M. Liu, *Preparation of poly (acrylic acid-co-acrylamide)/kaolin and release kinetics of urea from it.* Journal of Applied Polymer Science, 2007. **106**(5): p. 3007-3015.
68. Kiatkamjornwong, S. and P. Phunchareon, *Influence of reaction parameters on water absorption of neutralized poly (acrylic acid-co-acrylamide) synthesized by inverse suspension polymerization.* Journal of applied polymer science, 1999. **72**(10): p. 1349-1366.
69. Li, A., A. Wang, and J. Chen, *Studies on poly (acrylic acid)/attapulgite superabsorbent composite. I. Synthesis and characterization.* Journal of Applied Polymer Science, 2004. **92**(3): p. 1596-1603.
70. Lin, J., Q. Tang, and J. Wu, *The synthesis and electrical conductivity of a polyacrylamide/Cu conducting hydrogel.* Reactive and Functional Polymers, 2007. **67**(6): p. 489-494.
71. Rafieian, S., et al., *A review on nanocomposite hydrogels and their biomedical applications.* Science and Engineering of Composite Materials, 2019. **26**(1): p. 154-174.
72. Haraguchi, K. *Nanocomposite gels: new advanced functional soft materials*. in *Macromolecular Symposia*. 2007. Wiley Online Library.
73. Ianchis, R., et al., *Hydrogel-clay nanocomposites as carriers for controlled release.* Current Medicinal Chemistry, 2020. **27**(6): p. 919-954.
74. Dzulkharnien, N.S.F. and R. Rohani, *A review on current designation of metallic nanocomposite hydrogel in biomedical applications.* Nanomaterials, 2022. **12**(10): p. 1629.
75. Adewunmi, A.A., S. Ismail, and A.S. Sultan, *Carbon nanotubes (CNTs) nanocomposite hydrogels developed for various applications: a critical review.* Journal of Inorganic and Organometallic Polymers and Materials, 2016. **26**: p. 717-737.
76. Pan, C., L. Liu, and G. Gai, *Recent progress of graphene-containing polymer hydrogels: preparations, properties, and applications.* Macromolecular Materials and Engineering, 2017. **302**(10): p. 1700184.

77. SADEGHI, M. and Z.G. KOUCHAK, *Swelling kinetics study of hydrolyzed carboxymethylcellulose-poly (sodium acrylate-co-acrylamide) superabsorbent hydrogel with salt-sensitivity properties.* 2007.
78. Yoshimura, T., K. Matsuo, and R. Fujioka, *Novel biodegradable superabsorbent hydrogels derived from cotton cellulose and succinic anhydride: Synthesis and characterization.* Journal of Applied Polymer Science, 2006. **99**(6): p. 3251-3256.
79. Chang, C., et al., *Superabsorbent hydrogels based on cellulose for smart swelling and controllable delivery.* European polymer journal, 2010. **46**(1): p. 92-100.
80. Cheng, W.-M., et al., *Preparation and swelling properties of poly (acrylic acid-co-acrylamide) composite hydrogels.* e-Polymers, 2017. **17**(1): p. 95-106.
81. Zhong, M., et al., *Dually cross-linked single network poly (acrylic acid) hydrogels with superior mechanical properties and water absorbency.* Soft matter, 2016. **12**(24): p. 5420-5428.
82. Lee, K.M., et al., *Rapid accessible fabrication and engineering of bilayered hydrogels: Revisiting the cross-linking effect on superabsorbent poly (acrylic acid).* ACS omega, 2018. **3**(3): p. 3096-3103.
83. Li, W., et al., *Compressive mechanical properties and microstructure of PVA–HA hydrogels for cartilage repair.* RSC advances, 2016. **6**(24): p. 20166-20172.
84. Huang, Y., et al., *Preparation and swelling properties of graphene oxide/poly (acrylic acid-co-acrylamide) super-absorbent hydrogel nanocomposites.* Colloids and Surfaces A: Physicochemical and Engineering Aspects, 2012. **401**: p. 97-106.
85. Singh, J. and A. Dhaliwal, *Synthesis, characterization and swelling behavior of silver nanoparticles containing superabsorbent based on grafted copolymer of polyacrylic acid/Guar gum.* Vacuum, 2018. **157**: p. 51-60.
86. Gao, B., et al., *Super-adsorbent poly (acrylic acid)/laponite hydrogel with ultrahigh mechanical property for adsorption of methylene blue.* Journal of Environmental Chemical Engineering, 2021. **9**(6): p. 106346.
87. Kabiri, K., et al., *Superabsorbent hydrogel composites and nanocomposites: a review.* Polymer composites, 2011. **32**(2): p. 277-289.
88. Naguib, M., et al., *Two-dimensional nanocrystals produced by exfoliation of Ti3AlC2*, in *MXenes*. 2011, Jenny Stanford Publishing. p. 15-29.
89. Zhan, X., et al., *MXene and MXene-based composites: synthesis, properties and environment-related applications.* Nanoscale Horizons, 2020. **5**(2): p. 235-258.
90. Zhang, Y.-Z., et al., *MXenes stretch hydrogel sensor performance to new limits.* Science advances, 2018. **4**(6): p. eaat0098.
91. Zhang, P., et al., *Fabrication of novel MXene (Ti 3 C 2)/polyacrylamide nanocomposite hydrogels with enhanced mechanical and drug release properties.* Soft Matter, 2020. **16**(1): p. 162-169.
92. Zhang, J., et al., *Highly stretchable and self-healable MXene/polyvinyl alcohol hydrogel electrode for wearable capacitive electronic skin.* Advanced Electronic Materials, 2019. **5**(7): p. 1900285.
93. Alhabeb, M., et al., *Guidelines for synthesis and processing of two-dimensional titanium carbide (Ti3C2T x MXene).* Chemistry of Materials, 2017. **29**(18): p. 7633-7644.
94. Cao, M.-S., et al., *2D MXenes: electromagnetic property for microwave absorption and electromagnetic interference shielding.* Chemical Engineering Journal, 2019. **359**: p. 1265-

1302.
95. Parajuli, D., et al., *Advancements in MXene-polymer nanocomposites in energy storage and biomedical applications.* Polymers, 2022. **14**(16): p. 3433.
96. Chen, X., et al., *MXene/polymer nanocomposites: preparation, properties, and applications.* Polymer Reviews, 2021. **61**(1): p. 80-115.
97. He, S., et al., *Preparation strategies and applications of MXene-polymer composites: a review.* Macromolecular Rapid Communications, 2021. **42**(19): p. 2100324.
98. Shi, S., et al., *Self-assembly of MXene-surfactants at liquid–liquid interfaces: from structured liquids to 3D aerogels.* Angewandte Chemie International Edition, 2019. **58**(50): p. 18171-18176.
99. Huang, H., et al., *Recent development and prospects of surface modification and biomedical applications of MXenes.* Nanoscale, 2020. **12**(3): p. 1325-1338.
100. Riazi, H., et al., *Surface modification of a MXene by an aminosilane coupling agent.* Advanced Materials Interfaces, 2020. **7**(6): p. 1902008.
101. Zhao, J., et al., *A hydrophobic surface enabled salt-blocking 2D Ti 3 C 2 MXene membrane for efficient and stable solar desalination.* Journal of Materials Chemistry A, 2018. **6**(33): p. 16196-16204.
102. Hao, L., et al., *Novel thin-film nanocomposite membranes filled with multi-functional Ti3C2Tx nanosheets for task-specific solvent transport.* Composites Part A: Applied Science and Manufacturing, 2017. **100**: p. 139-149.
103. Ge, G., et al., *Ti3C2T x MXene-activated fast gelation of stretchable and self-healing hydrogels: a molecular approach.* ACS nano, 2021. **15**(2): p. 2698-2706.
104. Wang, Y., et al., *Synthesis of Ti3C2/Fe3O4/PANI hierarchical architecture composite as an efficient wide-band electromagnetic absorber.* Applied Surface Science, 2019. **480**: p. 830-838.
105. Boota, M., et al., *Pseudocapacitive electrodes produced by oxidant-free polymerization of pyrrole between the layers of 2D titanium carbide (MXene).* Adv. Mater, 2016. **28**(7): p. 1517-1522.
106. Thomas, V., et al., *Breathing-in/breathing-out approach to preparing nanosilver-loaded hydrogels: highly efficient antibacterial nanocomposites.* Journal of Applied Polymer Science, 2009. **111**(2): p. 934-944.
107. Yang, J., et al., *Early-state water migration characteristics of superabsorbent polymers in cement pastes.* Cement and Concrete Research, 2019. **118**: p. 25-37.
108. Yang, J. and F. Wang, *Influence of assumed absorption capacity of superabsorbent polymers on the microstructure and performance of cement mortars.* Construction and Building Materials, 2019. **204**: p. 468-478.
109. Nikdoost, A. and P. Rezai, *Dean flow velocity of viscoelastic fluids in curved microchannels.* AIP Advances, 2020. **10**(8): p. 085015.
110. Karimi, A., S. Yazdi, and A. Ardekani, *Hydrodynamic mechanisms of cell and particle trapping in microfluidics.* Biomicrofluidics, 2013. **7**(2): p. 021501.
111. Narayanamurthy, V., et al., *Microfluidic hydrodynamic trapping for single cell analysis: mechanisms, methods and applications.* Analytical Methods, 2017. **9**(25): p. 3751-3772.
112. Jalal, A. and R. Kiran, *Quantifying the water donation potential of commercial and corn starch hydrogels in a cementitious matrix.* Journal of Materials Research and Technology, 2023. **24**: p. 4336-4352.

113. Gibson, K.E. and K.J. Schwab, *Tangential-flow ultrafiltration with integrated inhibition detection for recovery of surrogates and human pathogens from large-volume source water and finished drinking water.* Applied and environmental microbiology, 2011. **77**(1): p. 385-391.
114. Wang, Z., et al., *Immunomagnetic separation: An effective pretreatment technology for isolation and enrichment in food microorganisms detection.* Comprehensive Reviews in Food Science and Food Safety, 2020. **19**(6): p. 3802-3824.
115. Jing, S., *Optimization of the diameter and water absorption capacity of superabsorbent polymer beads for three-dimensional filtration.* 2018.
116. Wu, X., et al., *Synthesis and Application of Superabsorbent Polymer Microspheres for Rapid Concentration and Quantification of Microbial Pathogens in Ambient Water.* Separation and Purification Technology, 2020: p. 116540.
117. Glick, C.C., et al., *Rapid assembly of multilayer microfluidic structures via 3D-printed transfer molding and bonding.* Microsystems & nanoengineering, 2016. **2**(1): p. 1-9.
118. Venzac, B., et al., *PDMS Curing Inhibition on 3D-Printed Molds: Why? Also, How to Avoid It?* Analytical chemistry, 2021. **93**(19): p. 7180-7187.
119. Xu, X., et al., *Optimization of microfluidic microsphere-trap arrays.* Biomicrofluidics, 2013. **7**(1): p. 014112.
120. Liu, Z. and G. Rempel, *Preparation of superabsorbent polymers by crosslinking acrylic acid and acrylamide copolymers.* Journal of Applied Polymer Science, 1997. **64**(7): p. 1345-1353.
121. Xia, Y. and G.M. Whitesides, *Soft lithography.* Annual review of materials science, 1998. **28**(1): p. 153-184.
122. Kabiri, K. and M.J. Zohuriaan-Mehr, *Porous superabsorbent hydrogel composites: synthesis, morphology and swelling rate.* Macromolecular Materials and Engineering, 2004. **289**(7): p. 653-661.
123. Zhang, K., W. Feng, and C. Jin, *Protocol efficiently measuring the swelling rate of hydrogels.* MethodsX, 2020. **7**: p. 100779.
124. Lalji, S.M., et al., *Comparative performance analysis of different swelling kinetic models for the evaluation of shale swelling.* Journal of Petroleum Exploration and Production Technology, 2022. **12**(5): p. 1237-1249.
125. Safaei, F., et al., *Preparation of an acrylic acid-based superabsorbent composite: investigation of synthesis parameters.* Chemical Papers, 2020. **74**(3): p. 939-949.
126. Zhu, L., et al., *Synthesis and the swelling behavior of sodium alginate graft poly (acrylic acid-co-acrylamide)/graphite oxide super absorbent composite.* Polymer Science, Series B, 2019. **61**(5): p. 680-690.
127. Manning, G.S., *Limiting laws and counterion condensation in polyelectrolyte solutions I. Colligative properties.* The journal of chemical Physics, 1969. **51**(3): p. 924-933.
128. Ebrahimi, R. and G.R. Bardajee, *Sonochemical synthesis and swelling behavior of Fe 3 O 4 nanocomposite based on poly (acrylamide-co-acrylic acid) hydrogel for drug delivery application.* Journal of Polymer Research, 2021. **28**(2): p. 1-12.
129. Tang, Y., et al., *Preparation and absorption studies of poly (acrylic acid-co-2-acrylamide-2-methyl-1-propane sulfonic acid)/graphene oxide superabsorbent composite.* Polymer Bulletin, 2019. **76**(3): p. 1383-1399.
130. de Souza e Castro, N.L., M. Nele, and J.C. Pinto. *Production of Crosslinked Starch*

Microparticles through Inverse Suspension Polymerization using Statistical Experimental Design. in *Macromolecular Symposia*. 2020. Bento Gonçalves, Rio Grande do Sul, Brazil: Wiley Online Library.
131. Feng, L., et al., *pH-sensitive polymeric particles as smart carriers for rebar inhibitors delivery in alkaline condition.* Journal of Applied Polymer Science, 2018. **135**(8): p. 45886.
132. Gharekhani, H., et al., *Superabsorbent hydrogel made of NaAlg-g-poly (AA-co-AAm) and rice husk ash: Synthesis, characterization, and swelling kinetic studies.* Carbohydrate polymers, 2017. **168**: p. 1-13.
133. Fosso-Kankeu, E., et al., *Thermodynamic properties and adsorption behaviour of hydrogel nanocomposites for cadmium removal from mine effluents.* Journal of Industrial and Engineering Chemistry, 2017. **48**: p. 151-161.
134. Khurana, A., et al., *Effect of polymer chains entanglements, crosslinks and finite extensibility on the nonlinear dynamic oscillations of dielectric viscoelastomer actuators.* Nonlinear Dynamics, 2021. **104**(2): p. 1227-1251.
135. Saalwächter, K., W. Chassé, and J.-U. Sommer, *Structure and swelling of polymer networks: insights from NMR.* Soft Matter, 2013. **9**(29): p. 6587-6593.
136. Yang, H., et al., *Mechanism and influencing factors on the initial particle size and swelling capability of viscoelastic microspheres.* Journal of Dispersion Science and Technology, 2015. **36**(11): p. 1673-1684.
137. Gupta, I., et al., *A study on effect of acrylic acid content on swelling behavior of poly (AAm-co-BMA-co-AAc) hydrogels.* Journal of Macromolecular Science, Part A: Pure and Applied Chemistry, 2007. **44**(4): p. 403-412.
138. Wang, J., et al., *Acrylated composite hydrogel preparation and adsorption kinetics of methylene blue.* Molecules, 2017. **22**(11): p. 1824.
139. Hulubei, C., et al., *New polyimide-based porous crosslinked beads by suspension polymerization: physical and chemical factors affecting their morphology.* Journal of Polymer Research, 2014. **21**: p. 1-16.
140. McGraw, J.D. and K. Dalnoki-Veress, *Swelling molecular entanglement networks in polymer glasses.* Physical Review E—Statistical, Nonlinear, and Soft Matter Physics, 2010. **82**(2): p. 021802.
141. Richbourg, N.R. and N.A. Peppas, *The swollen polymer network hypothesis: Quantitative models of hydrogel swelling, stiffness, and solute transport.* Progress in Polymer Science, 2020. **105**: p. 101243.
142. Hubbe, M.A., S. Azizian, and S. Douven, *Implications of apparent pseudo-second-order adsorption kinetics onto cellulosic materials: A review.* BioResources, 2019. **14**(3).
143. Zhang, W., et al., *Factors affecting the properties of superabsorbent polymer hydrogels and methods to improve their performance: a review.* Journal of Materials Science, 2021. **56**(29): p. 16223-16242.
144. von Treifeldt, J.E., et al., *The effect of Ti3AlC2 MAX phase synthetic history on the structure and electrochemical properties of resultant Ti3C2 MXenes.* Materials & Design, 2021. **199**: p. 109403.
145. Shuck, C.E., et al., *Scalable synthesis of Ti3C2Tx mxene*, in *MXenes*. 2023, Jenny Stanford Publishing. p. 539-560.
146. Rozmysłowska-Wojciechowska, A., et al., *A simple, low-cost and green method for controlling the cytotoxicity of MXenes.* Materials Science and Engineering: C, 2020. **111**:

p. 110790.
147. Szuplewska, A., et al., *2D Ti2C (MXene) as a novel highly efficient and selective agent for photothermal therapy.* Materials Science and Engineering: C, 2019. **98**: p. 874-886.
148. Vasyukova, I.A., et al., *Synthesis, toxicity assessment, environmental and biomedical applications of MXenes: A review.* Nanomaterials, 2022. **12**(11): p. 1797.
149. Yu, X., et al., *Fluorine-free preparation of titanium carbide MXene quantum dots with high near-infrared photothermal performances for cancer therapy.* Nanoscale, 2017. **9**(45): p. 17859-17864.
150. Nasrallah, G.K., et al., *Ecotoxicological assessment of Ti 3 C 2 T x (MXene) using a zebrafish embryo model.* Environmental Science: Nano, 2018. **5**(4): p. 1002-1011.